

Lehrstuhl für Experimentelle Orthopädie und Arthroseforschung

Universität des Saarlandes

Direktor: Prof. Dr. med. H. Madry

**Präzise mikrostrukturelle Analyse der frühen  
osteocondralen Reparatur im Kontext markstimulierender  
Verfahren in translationalen Tiermodellen**

*Dissertation zur Erlangung des Grades eines Doktors der Medizin*

der Medizinischen Fakultät

der UNIVERSITÄT DES SAARLANDES

2017

vorgelegt von Liang Gao

geboren am 07. Mai 1987 in Anhui, V. R. China

Lehrstuhl für Experimentelle Orthopädie und Arthroseforschung

Universität des Saarlandes

Direktor: Prof. Dr. med. H. Madry

**Precise microstructural evaluation of  
early osteochondral repair in the context of marrow  
stimulation in translational animal models**

*Dissertation for the degree of Doctor of Medicine*

Faculty of Medicine

SAARLAND UNIVERSITY

2017

submitted by Liang Gao

Born on May 07, 1987 in Anhui, P. R. China

## **DECLARATION**

I hereby declare that this thesis is my own original work and effort. All experiments, except for those specified, were exclusively performed by me. Except for the publications written by myself listed in the publication list, the data presented here have not been submitted elsewhere for any award. Where other sources of information and help have been used, they have been indicated and acknowledged.

Homburg, 21. 12. 2017

---

Liang Gao

## CONTENT

List of Abbreviations.....	VI
List of Figures.....	VII
List of Tables.....	VIII
1 ABSTRACT.....	1
2 ZUSAMMENFASSUNG.....	2
3 INTRODUCTION.....	3
3.1 The osteochondral unit as a structural and functional concept.....	3
3.2 Articular cartilage.....	3
3.2.1 Articular cartilage structure.....	3
3.2.2 Articular cartilage injury.....	5
3.3 Subchondral bone.....	6
3.3.1 Structure of subchondral bone.....	6
3.3.2 Role of subchondral bone for cartilage repair.....	7
3.4 Marrow stimulation techniques.....	7
3.4.1 Treatment theory.....	7
3.4.2 Technical principles.....	7
3.4.3 Outcomes.....	8
3.4.4 Microfracture.....	10
3.4.5 Enhanced microfracture with bone marrow aspirate.....	10
3.5 Alteration of subchondral bone after marrow stimulation treatment.....	11
3.5.1 Types of subchondral bone alteration and clinical evidence.....	11
3.5.2 Current analytic methods to examine subchondral bone alterations in translational models.....	11
3.5.3 High-resolution micro-computed tomography.....	12
4 HYPOTHESES.....	14
5 MATERIALS.....	15

5.1 Chemicals.....	15
5.2 Antibodies.....	15
5.3 Solutions and buffers.....	16
5.4 Softwares.....	16
5.5 Instruments and materials.....	17
5.6 Equipments.....	17
6 METHODS.....	18
6.1 Study design.....	18
6.2 Methods for developing a novel algorithm for the precise analysis of subchondral bone changes.....	18
6.2.1 Systematic review of the current analyzing methods.....	18
6.2.2 Animal studies.....	18
6.2.3 Micro-CT imaging of the subchondral bone following microfracture treatment.....	19
6.2.4 Introduction of the algorithm for analysing of subchondral bone changes.....	20
6.2.5 Inter-rater reliability of the algorithm.....	20
6.2.6 Comparison of the algorithm with the most comprehensive existing method.....	20
6.3 Methods applied to test the early loss of subchondral bone following bone marrow aspirate enhanced microfracture.....	21
6.3.1 Treatment groups.....	21
6.3.2 Animal surgeries.....	22
6.3.3 Evaluation of articular cartilage repair.....	26
6.3.4 Evaluation of subchondral bone reconstitution.....	28
6.4 Statistical analysis.....	34
7 RESULTS.....	35
7.1 A novel algorithm for the precise analysis of subchondral bone changes.....	35
7.1.1 Systematic review of current analytic methods.....	35

7.1.2 Algorithm for the analysis of subchondral bone changes.....	36
7.1.3 Evaluation of the novel algorithm in two large animal models.....	40
7.1.4 Inter-rater reliability of the algorithm.....	43
7.1.5 Comparison of the present algorithm with the most comprehensive scoring system.....	43
7.2 Bone marrow aspirate enhanced microfracture counteracting the early postoperative loss of subchondral bone.....	48
7.2.2 Articular cartilage repair.....	48
7.2.3 Subchondral bone reconstitution.....	51
8 DISCUSSION.....	60
8.1 Discussion of the novel algorithm for analysis of subchondral bone alterations .....	60
8.1.1 Key advantages of the new algorithm.....	61
8.1.2 Practicality, reliability, and enhanced precision of the algorithm.....	62
8.1.3 Limitations of the novel algorithm.....	63
8.1.4 Potential clinical implications of the novel algorithm.....	63
8.2 Discussion of bone marrow aspirate-enhanced microfracture.....	64
8.2.1 Animal model selection.....	64
8.2.2 Significant loss of subchondral bone following microfracture.....	65
8.2.3 Subchondral bone loss after debridement.....	66
8.2.4 Equivalent outcome of cartilage repair between debridement and microfracture.....	66
8.2.5 Comparable outcome of cartilage repair following microfracture without and with bone marrow aspirate.....	67
8.2.6 Outlook of enhanced microfracture techniques.....	67
8.2.7 Clinical implications.....	68
8.2.8 Limitations of the study on bone marrow aspirate-enhanced microfracture.....	68
8.3 Conclusions.....	69

9 REFERENCES.....	70
10 PUBLICATIONS AND PRESENTATIONS.....	78
11 ACKNOWLEDGEMENTS.....	81

## List of Abbreviations

2D	Two-dimensional
3D	Three-dimensional
BMA	Bone marrow aspirate
BMD	Bone mineral density
BS/BV	Specific bone surface
BS/TV	Bone surface density
BV/TV	Bone volume fraction
CaHA	Calcium hydroxyapatite
Ct.Th	Cortical thickness
DA	Degree of anisotropy
FD	Fractal dimension
Hd	Horizontal distance
HE	Hematoxylin and eosin
MFx	Microfracture
Micro-CT	Micro-computed tomography
MRI	Magnetic resonance imaging
PRISMA	Preferred Reporting Items for Systematic Reviews and Meta-Analyses
ROI	Region of interest
Safranin O	Safranin orange/fast green
SAS	Subarticular spongiosa
SBP	Subchondral bone plate
SD	Standard deviation
SMI	Structure model index
Tb.Th	Trabecular thickness
Tb.Sp	Trabecular separation
Tb.Pf	Trabecular pattern factor
Tb.N	Trabecular number
Vd	Vertical distance
VOI	Volume of interest

## List of Figures

Figure 1.	Zonal architecture of articular cartilage.	4
Figure 2.	Schematic of the osteochondral unit.	6
Figure 3.	Marrow stimulation techniques.	9
Figure 4.	Alterations of subchondral bone during the osteochondral repair following the marrow stimulation.	13
Figure 5.	Schematic drawing depicting the study design.	22
Figure 6.	Positioning and draping for the minipig surgery.	24
Figure 7.	Key procedures and instruments for the chondral defect creation and treatment.	25
Figure 8.	Standardized regions of interest for the histomorphometric analysis	29
Figure 9.	Standardized regions of interest for the quantitative micro-CT evaluation of the subchondral bone.	31
Figure 10.	Mathematical modeling for calculating the change of subchondral bone volume following the microfracture procedure.	33
Figure 11.	Flowchart of the literature searching in the MEDLINE database.	35
Figure 12.	Micro-CT based algorithm for the analysis of the subchondral bone changes following microfracture treatment.	39
Figure 13.	Identification of intra-lesional osteophytes, residual microfracture holes, peri-hole bone resorption, and subchondral bone cysts.	41
Figure 14.	Schematic of microfracture procedure in animal models and micro-CT image patterns of the osteochondral unit in the minipig model.	42
Figure 15.	Representative micro-CT images of a single defect possessing multiple patterns of subchondral bone changes and the quantitation of the subchondral bone changes applying different thresholds of the algorithm.	44
Figure 16.	Comparison of the results of the Chen score and the present algorithm for analysing the subchondral bone changes in the two animal models.	47
Figure 17.	Macroscopic, histological and immunohistochemical analyses of the osteochondral unit.	49
Figure 18.	Histomorphometric analyses of subchondral bone changes below the cartilage defects treated with the three experimental strategies.	53
Figure 19.	Qualitative and quantitative analysis of subchondral bone changes underlying defects treated with the three strategies.	56
Figure 20.	Mathematical modeling of subchondral bone volume changes within defect region following the three treatments.	59

## List of Tables

Table 1.	Chemicals.	15
Table 2.	Antibodies.	15
Table 3.	Recipes of solutions and buffers.	16
Table 4.	Softwares.	16
Table 5.	Instruments and materials for animal surgery.	17
Table 6.	Equipments used in the tissue process and analysis.	17
Table 7.	The Chen scoring system for a semi-quantitative assessment of the subchondral bone alterations.	21
Table 8.	The macroscopic scoring system for the macroscopic description of articular cartilage repair.	27
Table 9.	Histological scoring system from Sellers et al.	30
Table 10.	Systematic review of the four major types of subchondral bone changes after microfracture treatment and corresponding evaluation methods in animal models.	36
Table 11.	Semi-quantitative estimation of intra-lesional osteophytes in the minipig and sheep models applying the Chen score and the present algorithm.	45
Table 12.	Semi-quantitative estimation of residual microfracture holes and subchondral bone cysts in the minipig and sheep models applying the Chen score.	46
Table 13.	Semi-quantitative evaluation of bone resorption in the minipig and sheep models applying the Chen score.	46
Table 14.	Macroscopic evaluation of the articular cartilage repair tissue.	48
Table 15.	Histological evaluation of the articular cartilage repair tissue.	50
Table 16.	Evaluation of immunoreactivity to type-II collagen in the articular cartilage repair tissue.	51
Table 17.	Histomorphometric analysis of the subchondral bone below the treated cartilage defects.	52
Table 18.	Comparative and descriptive results of the micro-CT analysis regarding residual microfracture holes and peri-hole bone resorption.	54
Table 19.	Comparison of micro-CT parameters of Volume of Interests between the defect area and the adjacent control.	55
Table 20.	Comparison of the micro-CT parameters of the subchondral bone plate and the subarticular spongiosa of defect region between three treatment groups.	57

Table 21.	Change of bone volume fraction of the subchondral bone plate under defects treated by the three treatment strategies at 4 weeks postoperatively.	58
Table 22.	Change of bone volume fraction of the subarticular spongiosa under defects treated by the three treatment strategies at 4 weeks postoperatively.	58

## 1 ABSTRACT

Articular cartilage defects do not heal. Microfracture, the most commonly applied marrow stimulation procedure, results in fibrocartilaginous repair and induces alterations of the subchondral bone. These alterations are emerging as considerable clinical problems and include intra-lesional osteophytes, residual microfracture holes, peri-hole bone resorption, and subchondral bone cysts. A precise distinction between different alteration patterns is becoming increasingly important. Of similar importance, enhanced microfracture techniques with additional application of bone marrow aspirate may avoid these pathological subchondral bone changes.

In the present study, we selected the microfracture technique to precisely investigate osteochondral repair in the context of marrow stimulation in minipig and sheep models. A second focus was placed on the early effects of debridement and microfracture treatment without or with bone marrow aspirate on the osteochondral unit in a full-thickness minipig chondral defect model after 4 weeks in vivo.

Based on the continuous micro-CT datasets, we designed a tailored algorithm to analyze the subchondral bone changes following microfracture treatment in two animal models, allowing for a clear definition of each entity. We demonstrated that this novel algorithm is highly reliable, reproducible, and valid. Comparison analysis with the best existing semi-quantitative evaluation method supported the enhanced precision of this algorithm. Moreover, comparing microfracture without or with autologous bone marrow aspirate revealed that microfracture induced a substantial early resorption of the subchondral bone. These changes were counteracted by the additional application of bone marrow aspirate.

These data suggest that microfracture induced a substantial early resorption of the subchondral bone which can be precisely analysed. They also highlight the potential value of bone marrow aspirate as an adjunct to marrow stimulation to counteract subchondral bone alterations following cartilage repair procedures.

## 2 ZUSAMMENFASSUNG

Defekte des hyalinen Gelenkknorpels heilen nicht. Die am häufigsten angewandte Technik zur Markraumstimulation, die Mikrofrakturierung, führt zu einer fibrocartilaginären Reparatur und induziert Veränderungen des subchondralen Knochens. Diese Alterationen treten als erhebliche klinische Probleme auf und schließen intraläsionale Osteophyten, verbleibende Mikrofrakturlöcher, periläsionale Knochenresorption und subchondrale Knochenzysten ein. Eine genaue Unterscheidung zwischen den verschiedenen Veränderungsmustern gewinnt zunehmend an Bedeutung. Von ähnlicher Wichtigkeit sind verbesserte Mikrofrakturierungstechniken mit zusätzlicher Anwendung von autologen Knochenmarkaspirat, um diese pathologischen subchondralen Knochenveränderungen zu reduzieren.

In der vorliegenden Studie haben wir die Technik der Mikrofrakturierung ausgewählt, um die subchondralen Knochenveränderungen nach Markraumstimulation zu untersuchen. Ein weiterer Fokus wurde auf die frühen Effekte von Débridement und Mikrofrakturierungsbehandlung ohne oder mit Applikation von autologem Knochenmarkaspirat auf die osteochondrale Einheit in einem vollschichtigen chondralen Minipig-Defektmodell nach 4 Wochen *in vivo* gelegt.

Basierend auf kontinuierlichen Micro-CT-Datensätzen haben wir einen präzisen Algorithmus entwickelt, um die subchondralen Knochenveränderungen nach der Mikrofrakturierung in zwei Tiermodellen zu analysieren und eine klare Definition der einzelnen Veränderungen zu ermöglichen. Dieser neuartige Algorithmus ist zuverlässig, reproduzierbar und valide. Die Vergleichsanalyse mit der bestmöglichen semiquantitativen Bewertungsmethode unterstrich seine verbesserte Präzision. Darüber hinaus zeigen die Daten vom Vergleich der Mikrofrakturierung ohne oder mit Knochenmarkaspirat, dass die Mikrofrakturierung eine wesentliche frühe Resorption des subchondralen Knochens induziert. Diesen Veränderungen wirkt die zusätzliche Anwendung von Knochenmarkaspirat entgegen.

Diese Daten lassen vermuten, daß die Mikrofrakturierung eine substanzielle frühe Resorption des subchondralen Knochens induziert. Durch den neu entwickelten Algorithmus sind diese pathologischen Veränderungen präzise analysierbar. Die Daten heben ebenfalls den Wert von autologem Knochenmarkaspirat als möglicher Zusatz zur Markraumstimulation hervor, um subchondralen Knochenveränderungen nach rekonstruktiver Knorpelchirurgie entgegenzuwirken.

## **3 INTRODUCTION**

### **3.1 The osteochondral unit as a structural and functional concept**

A human joint as complex connection of functional units is uniquely constructed to allow for the constrained joint movement. The fundamental elements of a classic diarthrodial joint include the two articulating bones, the articular cartilage covering the ends of bones, the ligaments connecting bones to other bones, and the synovial membrane lining the joint cavity, and the tendons (GOLDRING, GOLDRING, 2016; MADRY et al., 2010). The articular cartilage and the underlying subchondral bone are separated by a thin layer of calcified cartilage, allowing for a gradual transition of the mechanical properties (MADRY et al., 2010). Such biocomposites of the articular cartilage, subchondral bone and calcified cartilage are known as the osteochondral unit, featuring the unique capability of transferring loads during the weight-bearing and joint movement (MADRY, 2010a). Recent evidence showed that the osteochondral unit is a structural and functional whole, and alterations in the composition or structure of any individual parts will disrupt the integrity and function of the entire joint (ORTH et al., 2012b). Although the past decades have witnessed considerable advances in the treatment of the articular cartilage defects, little attention has been paid to the defects involving both the articular cartilage and the underlying subchondral bone.

### **3.2 Articular cartilage**

#### **3.2.1 Articular cartilage structure**

Articular cartilage is the highly specialized connective tissue, providing smooth lubricated surfaces for articulation and facilitating the loading transmission in low-friction means. It is composed of a dense extracellular matrix with sparsely distributed chondrocytes. The extracellular matrix is principally composed of water, collagen, proteoglycans, and glycoproteins (BUCKWALTER, MANKIN, 1997; WOO, BUCKWALTER, 1988). These components function to retain the water content within the matrix and to maintain the unique mechanical properties of the articular cartilage. Of note, articular cartilage is devoid of blood vessels, lymphatics, and nerves.

The collagens within the articular cartilage are mainly type-II collagen and type-X collagen, accounting for over 50% of the dry weight. Along with the matrix and collagens, chondrocytes contribute to the specific zonal architecture of the articular cartilage, including the tangential zone, the transitional zone, the radial zone, and the calcified cartilage zone (BHOSALE, RICHARDSON, 2008) (Figure 1).

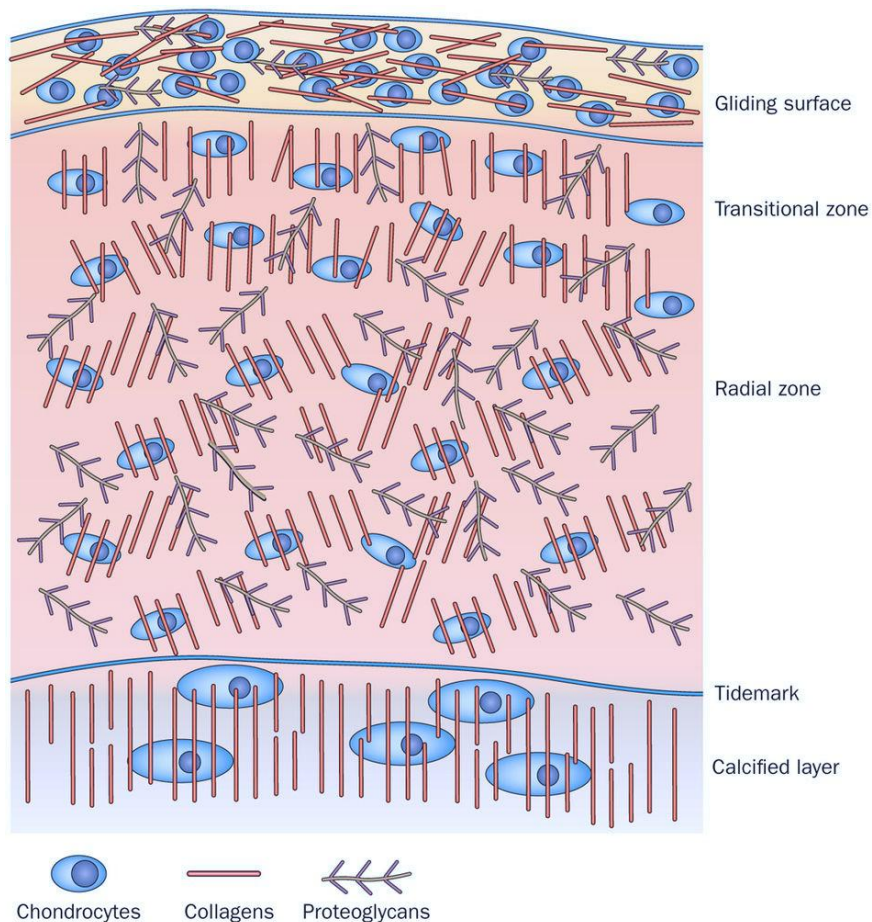


Figure 1. Zonal architecture of articular cartilage. Figure reproduced from (HARDIN et al., 2015).

The tangential zone (gliding surface), making up approximately 10% to 20% of the articular cartilage thickness, protects the deeper layers from the shear forces. This zone mainly functions to resist the shear, tensile, and compressive forces. The collagen fibers of this zone are tightly packed with relatively abundant chondrocytes and arrange parallel to the articular surface.

The transitional zone provides an anatomic and functional bridge between the tangential and deep zones. It functions as the first line to resist to compressive forces. This zone contains proteoglycans and thicker collagen fibrils and represents approximately 50% of the total cartilage volume. The collagen fibers are organized obliquely and the chondrocytes are spherical with a low density.

The radial zone represents approximately 30% of the total cartilage volume, and provides the greatest resistance to compressive forces. It contains the largest diameter collagen fibrils in a radial disposition, the highest proteoglycan content, and the lowest water concentration. The chondrocytes are characteristically arranged in the columnar orientation, parallel to the collagen fibers and perpendicular to the joint line.

The calcified cartilage layer is separated from the radial zone by the tidemark. The chondrocytes are scarce and hypertrophic in this zone. This zone plays an integral role in securing the articular cartilage to bone by anchoring the collagen fibrils of the radial zone to the underlying subchondral bone.

### **3.2.2 Articular cartilage injury**

Articular cartilage injury is a common disorder. The injured cartilage has a limited capacity for the intrinsic healing or repair. Curl and colleagues reviewed 31,516 knee arthroscopies and detected a total of 53,569 articular cartilage lesions in 63% of procedures (19,827), with an average of 2.7 lesions per knee (CURL et al., 1997). This unique and complex structure of the articular cartilage makes the treatment of articular cartilage defects clinically challenging.

### 3.3 Subchondral bone

#### 3.3.1 Structure of subchondral bone

Subchondral bone, the other component of the osteochondral unit, is the bony structure immediately underlying the calcified layer of the articular cartilage (Figure 2). The cement line separates the calcified cartilage layer from the subchondral bone. Structurally, the subchondral bone could be further divided into two components: the subchondral bone plate (cortical bone) and the subarticular spongiosa (trabecular bone). The detailed architecture of the subchondral bone is of high variation topographically depending upon the specific joint. The thickness of the subchondral bone plate also varies in different joints, as well as the contour of the tidemark and cement line, the number and type of perforations in the subchondral bone plate, density, and composition (ARMSTRONG *et al.*, 1995; BULLOUGH *et al.*, 1985; MÜLLER-GERBL *et al.*, 1998). Likewise, the trabecular structure and mechanical properties of the subarticular spongiosa differ between the weight-bearing and non-weight-bearing regions of the joints (CHEN *et al.*, 2013).

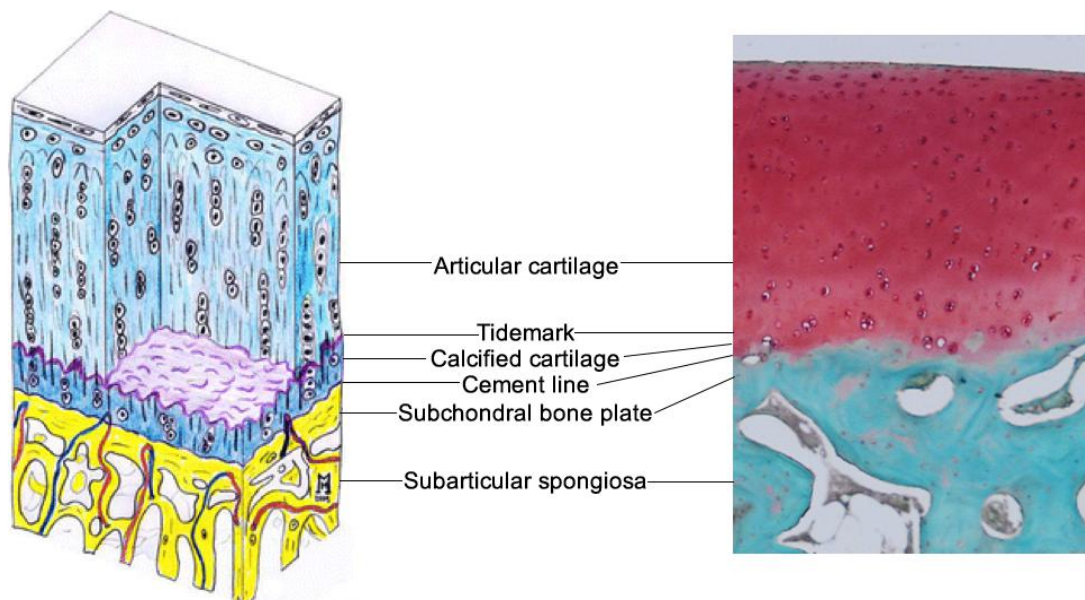


Figure 2. Schematic of the osteochondral unit. Figure adapted from (MADRY, 2010b).

The interaction between the cartilage and the subchondral bone occurs mainly between the calcified cartilage and subchondral bone plate, termed the osteochondral junction and marked with the cement line. With the scanning electron microscope, Inoue *et al.*,

reported that the subchondral plate under the osteochondral junction is composed of lamellated sheets of parallel collagen fibrils with occasional vascular channels connecting to the osteochondral junction by small canals (INOUE, 1981). Glaser *et al.*, noted that no collagen fibers are continuous between the calcified cartilage and the cortical endplate (GLASER, PUTZ, 2002), indicating a relative weakness of the osteochondral junction compared to other regions of the osteochondral unit.

### **3.3.2 Role of subchondral bone for cartilage repair**

The integrity of the subchondral bone is a significant factor for the success of cartilage repair (GOMOLL *et al.*, 2010; HOEMANN *et al.*, 2012). Its components, the subchondral bone plate and the subarticular spongiosa, play a key role in the mechanically and metabolically supporting of the articular cartilage (IMHOF *et al.*, 1999; IMHOF *et al.*, 2000).

## **3.4 Marrow stimulation techniques**

### **3.4.1 Treatment theory**

Marrow stimulation is the most important first-line treatment option for small symptomatic articular cartilage defects. It aims to establish a communication between the cartilage defect and the subchondral bone marrow compartment and to fill the defect with mesenchymal stem cells derived from bone marrow within the underlying subchondral bone. Subsequently, the pluripotent progenitor cells migrate from the subchondral compartment into the defect, differentiate into chondrocytes, and generate a fibrocartilaginous repair tissue over time. Such repair tissue aids to stabilize the adjacent normal cartilage and to prevent the advancement of osteoarthritic degeneration.

### **3.4.2 Technical principles**

As the initial step of the marrow stimulation, the cartilage defect should be prepared in a meticulous fashion, including the removal of cartilage fragments and the generation of stable and vertically oriented margins of the peripheral cartilage. Then the bony defect base is prepared and debrided with the removal of the entire calcified cartilage layer and the exposure of the superficial part of the subchondral bone plate. Frisbie and colleagues highlighted the importance of the removal of the calcified cartilage layer with

retention of the subchondral bone plate on the healing of chondral defects treated with microfracture (MFx) in horses at 1 year (FRISBIE et al., 2006). Such a debridement of human cartilage defects down to the subchondral bone induced the penetrations of the subchondral bone plate (DROBNIC et al., 2010), thus creating an access to the marrow elements.

The standardized marrow stimulation can be performed by one of three different techniques: microfracture, subchondral drilling, and abrasion arthroplasty (Figure 3). Microfracture induces multiple holes of the subchondral bone plate by the use of the sharp tip of a microfracture awl (STEADMAN et al., 2001). Subchondral drilling, proposed as early as 1957 (SMILLIE, 1957), is often termed Pridie drilling (PRIDIE, GORDON, 1959). Here, the rotating instrument, a drill bit or a Kirschner wire (K-wire), cuts through the subchondral bone plate into the subarticular spongiosa to create a defined number of standardized cylindrical holes to a certain depth. Abrasion arthroplasty, in contrast, refers to a generalized abrasion of the subchondral bone plate of a limited depth (JOHNSON, 1986). The small bony canals within the subchondral bone plate are opened following the abrasion with a round burr by removing about 1.0-1.5 mm of its thickness without completely eliminating the subchondral bone plate. Such an abrasion exposes the vascularity of the subchondral bone plate and provides the connection between the defect and the subchondral bone marrow.

### **3.4.3 Outcomes**

In appropriate patients, marrow-stimulation techniques have historically produced the reliable and good short-term outcomes with improvement of the pain control and return of function (MITHOEFER et al., 2009; MITHOEFER et al., 2005, 2006; STEADMAN et al., 2003; STEADMAN et al., 2001). However, the durability of the sustained clinical improvement beyond 2 years after microfracture is variable (MCCORMICK et al., 2014; XING et al., 2013).

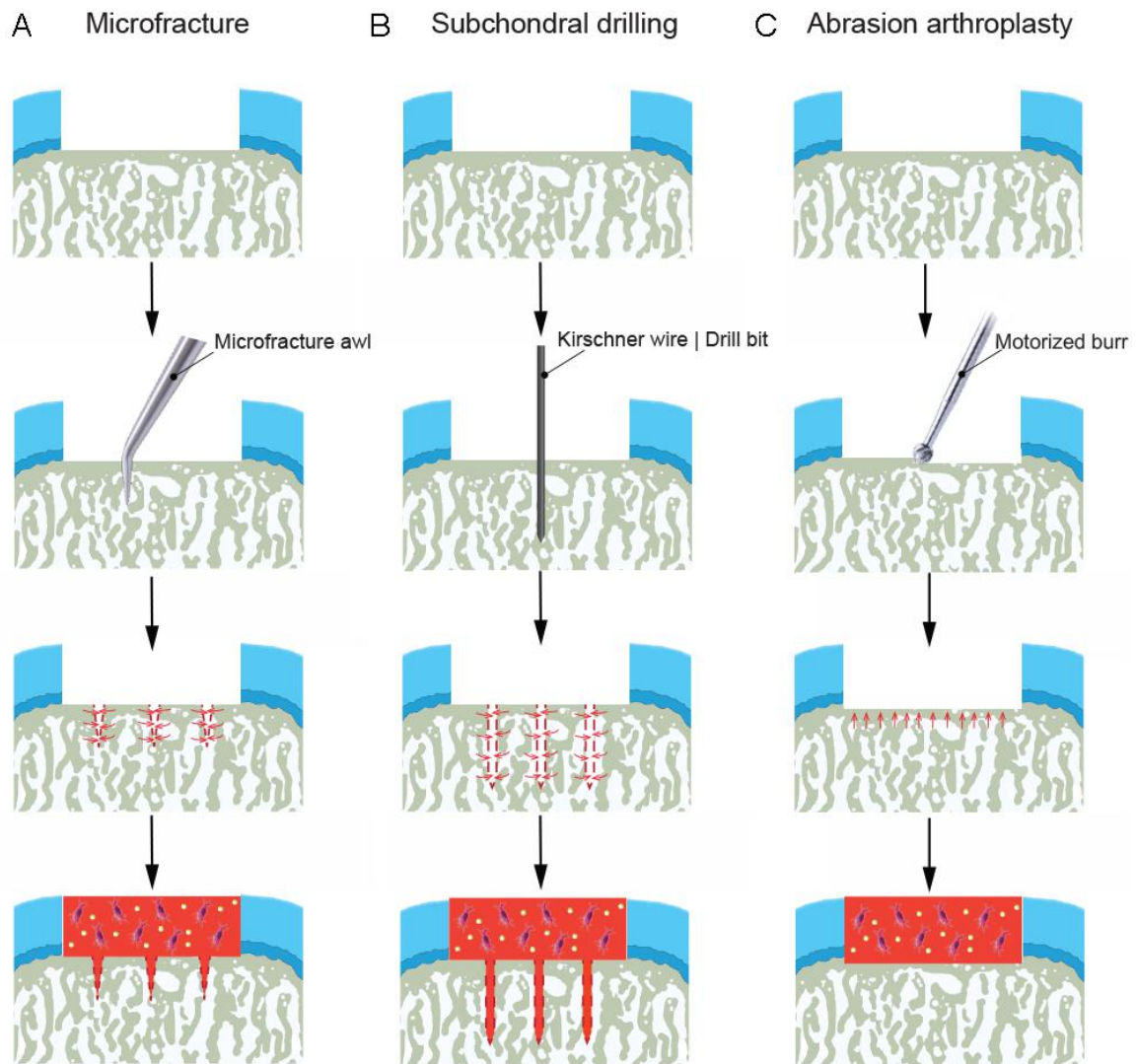


*Figure 3. Marrow stimulation techniques including microfracture (A), subchondral drilling (B), or abrasion arthroplasty (C). The cartilage defect should first be meticulously prepared in a standardized manner. The subchondral bone plate can be perforated with a microfracture awl (microfracture), a Kirschner wire or a drill bit (subchondral drilling), or a motorized burr (abrasion arthroplasty). After marrow stimulation, bone marrow containing mesenchymal stem cells ascends from the marrow cavity of the underlying subchondral bone via the channels generated by the marrow stimulation procedures. Defects containing bone marrow from the subchondral bone gradually forms a cartilaginous repair tissue within them. Red dashed lines show the outline of holes created by microfracture and subchondral drilling. Red arrows within the subchondral bone denote the migration direction of the liquid bone marrow. Figure adapted from (MADRY et al., 2017).*

#### **3.4.4 Microfracture**

Microfracture is the most commonly applied marrow stimulation technique. It generally yields a fibrous repair tissue (fibrocartilage), which lacks the biomechanical characteristics of the hyaline cartilage to withstand the compressive forces within the joint (STEADMAN et al., 2010). Such a fragile fibrocartilage generally deteriorates over time with the returning of the original symptoms and the frequent progression to the osteoarthritis (MITHOEFER et al., 2009).

#### **3.4.5 Enhanced microfracture with bone marrow aspirate**

Recently, enhanced techniques of microfracture have been proposed with the aim to better support chondrogenesis within the cartilage defect (ERGGELET, 2014; FORTIER et al., 2010; HOEMANN et al., 2005). Among those enhanced microfracture techniques, the application of bone marrow concentrate as an adjunct to the microfracture technique has been shown to improve articular cartilage repair in multiple animal models (BETSCH et al., 2013; FORTIER et al., 2010) and patients (ENEA et al., 2015; GIGANTE et al., 2011). Fortier *et al.* demonstrated the superiority of concentrated bone marrow aspirate augmented microfracture over microfracture alone the acute cartilage repair in a horse model (FORTIER et al., 2010). Gigante *et al.* provided a case series of 9 patients treated with microfracture and a collagen membrane immersed in autologous bone marrow concentrate, showing clinical improvements with a fibrocartilaginous repair tissue after 1 year (GIGANTE et al., 2011). Furthermore, the bone marrow aspirate has been proven to possess a robust osseous regenerative capacity when applied to long bone defects in both animals (GIANAKOS et al., 2016) and patients (WEEL et al., 2015). A recent double-blind randomized controlled clinical trial showed that additional application of concentrated blood and bone marrow aspirate to the operative treatment of fifth metatarsal stress fractures led to an earlier fracture union than surgery alone (WEEL et al., 2015).

### **3.5 Alteration of subchondral bone after marrow stimulation treatment**

#### **3.5.1 Types of subchondral bone alteration and clinical evidence**

A complete reestablishment of the osteochondral unit is the goal of all articular repair techniques (BRITTBURG et al., 1994; JOHNSON, 1986; PRIDIE, 1959; STEADMAN et al., 2001). Traditionally, a focus was placed on the cartilaginous repair tissue, but it is now recognized that complex structural changes of the subchondral bone emerging as a considerable clinical problem associated with different articular cartilage repair techniques (MADRY et al., 2010). These structural changes include the upward migration of the subchondral bone plate, the formation of intralesional osteophytes, the appearance of subchondral bone cysts, and the impairment of the osseous microarchitecture (Figure 4) (ORTH et al., 2012a).

For the marrow stimulation, despite clinical short- and mid-term success (GOYAL et al., 2013, SARIS et al., 2009), subchondral bone changes are thought to influence the long-term clinical outcome of the cartilage repair following the marrow stimulation (MITHOEFER et al., 2009; ORTH et al., 2013; STEADMAN et al., 2001; VANLAUWE et al., 2011). For instance, subchondral bone cysts or intra-lesional osteophytes (ORTH et al., 2013) were noticed in up to 33% of patients treated with the marrow stimulation (COLE et al., 2011; KREUZ et al., 2006; MITHOEFER et al., 2005; SARIS et al., 2009). Autologous chondrocyte implantation (ACI) for articular cartilage defects previously treated with marrow stimulation techniques has a three-fold higher failure rate than for the previously untreated defects (COLE et al., 2011; MINAS et al., 2009; VASILADIS et al., 2010). These data highlight the need to account for the complex role of subchondral bone alterations during the process of pursuing the optimal osteochondral repair.

#### **3.5.2 Current analytic methods to examine subchondral bone alterations in translational models**

Accumulative translational evidence for these subchondral bone alterations were also reported in both small (AROEN et al., 2006; CHEN et al., 2009; CHEN et al., 2011a; HEIR et al., 2012; MARCHAND et al., 2011; MARCHAND et al., 2012; NAM et al., 2004; QIU et al., 2003) and large preclinical animal models (DOROTKA et al., 2005; FRISBIE

et al., 1999; HANIE et al., 1992; HOEMANN et al., 2005; HOWARD et al., 1994; ISHIMARU et al., 1992; LANE et al., 2004; ORTH et al., 2012b; VACHON et al., 1986) of cartilage defects.

These translational studies have attempted to evaluate these postoperative morphological changes of the subchondral bone by histology (CHEN et al., 2011a; GILL et al., 2005; HOEMANN et al., 2005) and conventional radiography (FRISBIE et al., 2006; FRISBIE et al., 1999; MCILWRAITH et al., 2011). However, a precise distinction especially between residual microfracture holes, bone resorption, and cyst formation is often difficult to make when applying these methods.

### **3.5.3 High-resolution micro-computed tomography**

High-resolution micro-computed tomography (micro-CT) allows for a quantitative evaluation of the subchondral microarchitecture in a three-dimensional (3D) and non-invasive manner, overcoming the limitations of histology and conventional radiographic modalities. Chen and colleagues proposed a micro-CT-based scoring system to estimate subchondral bone changes in rabbits after microfracture treatment (CHEN et al., 2011a). However, the categorical scoring system described by the authors relies on subjective evaluations and yields semi-quantitative information. Consequently, the obtained data do not represent the actual measurements on a continuous scale, hindering the comparison of studies with different designs.

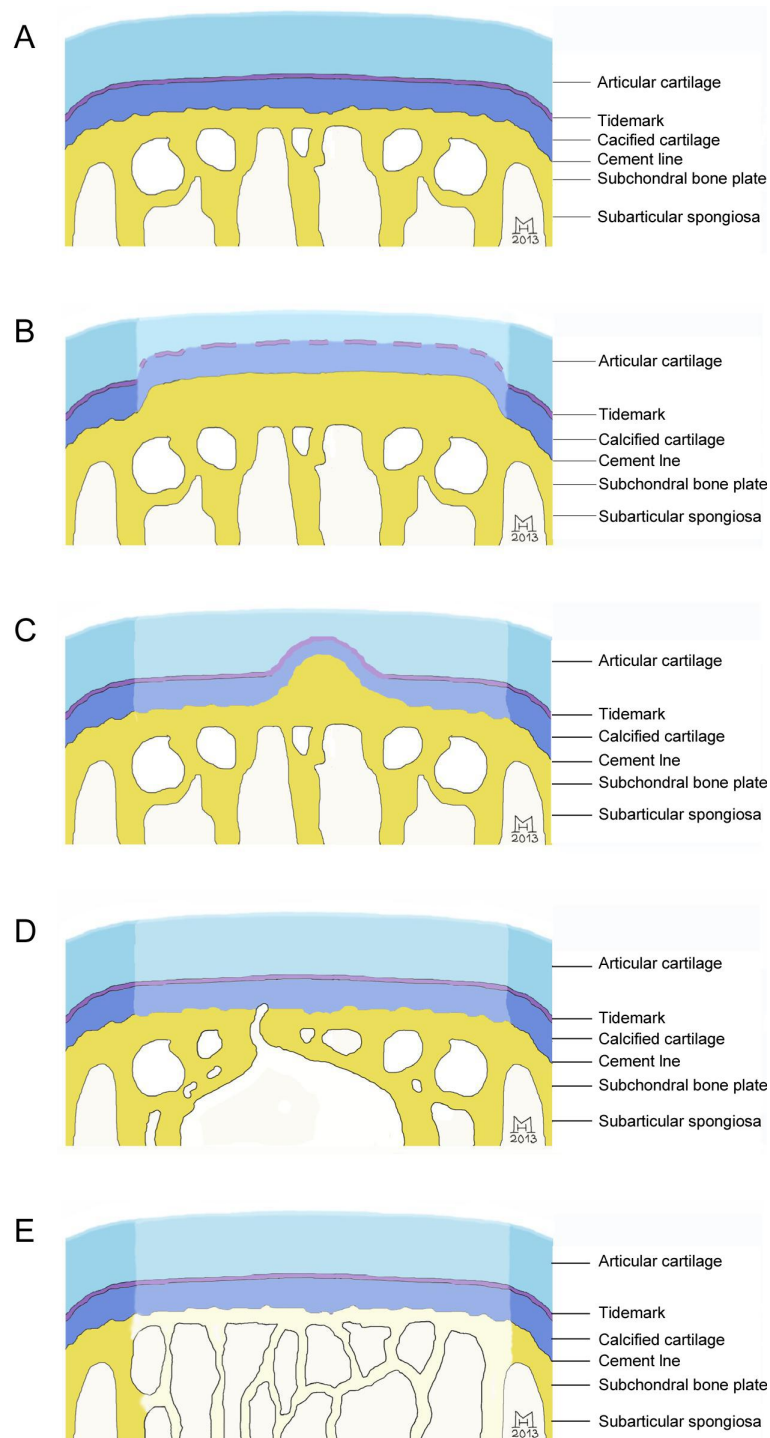


*Figure 4. Alterations of subchondral bone during the osteochondral repair following the marrow stimulation. (A) structure of a normal osteochondral unit. The possible postoperative alterations of the subchondral bone include (B) the generalized upward migration of the subchondral bone plate, (C) the formation of focal intralesional osteophytes, (D) the subchondral bone cysts, and (E) the impairment of the microarchitecture of the subchondral bone. The osteochondral repair tissue is identified with a less intense colour (B-D). Figure reproduced from (ORTH et al., 2012a).*

## 4 HYPOTHESES

In the present study, we selected the microfracture technique to investigate subchondral bone changes following marrow stimulation treatment. A focus was placed on the early effects of debridement and microfracture treatment without or with autologous bone marrow aspirate on the osteochondral unit in the full-thickness chondral defect models. We tested the following two hypotheses:

- (1) A novel algorithm for the precise analysis of subchondral bone changes with enhanced precision compared to the best existing evaluation method can be developed.
- (2) Early loss of subchondral bone following microfracture can be counteracted by bone marrow aspirate in a translational model of osteochondral repair.

## 5 MATERIALS

### 5.1 Chemicals

Product	Manufacturer
ABC-Reagent (Avidin-Biotin-Peroxidase-Reagent)	Vector, Burlingame, California, USA
Albumin Standard	Thermo Scientific, Rockford, USA
Braunol	B. Braun, Melsungen, Germany
BSA (bovines Serum Albumin)	Sigma, Taufkirchen, Germany
Diaminobenzidine (DAB reagent)	Sigma, Deisenhofen, Germany
Fast Green	ICN Biomedicals, Eschwege, Germany
Eosin G	Roth, Karlsruhe, Germany
Acetic acid (1%)	Merck, Darmstadt, Germany
Ethanol	Roth, Karlsruhe, Germany
Formalin Stock Solution (37%)	Sigma, Taufkirchen, Germany
Goldner Solution I (Ponceau acid fuchsin)	Roth, Karlsruhe, Germany
Goldner Solution II (Phosphotungstic acid-O)	Roth, Karlsruhe, Germany
Goldner Solution III (Light green SF)	Roth, Karlsruhe, Germany
Haematoxylin	Roth, Karlsruhe, Germany
Ketavet (Ketamin-Hydrochlorid)	Pharmacia & Upjohn, Erlangen, Germany
Narcoren (Sodium pentobarbital)	Merial, Hallbergmoos, Germany
Paraffin granules	Roth, Karlsruhe, Germany
Rompun (Xylazin-Hydrochloride)	Bayer, Leverkusen, Germany
Roti-Histokitt II (Mounting device)	Roth, Karlsruhe, Germany
Safranin Orange	Roth, Karlsruhe, Germany
HCl (1%)	Sigma, Taufkirchen, Germany
Hydrogen peroxide	Sigma, Taufkirchen, Germany
Xylene	Fischar, Saarbrücken, Germany
Ketamine	Ketanest S, Pfizer, Berlin, Germany
Xylazine	Rompun, Bayer, Leverkusen, Germany
Atropine	B. Braun, Melsungen, Germany
Propofol	AstraZeneca, Wedel, Germany
Isoflurane	Baxter, Unterschleißheim, Germany
Caprofen	Rimadyl, Pfizer Animal Health, Berlin, Germany
Sterile saline	Ecotainer, B. Braun Medical AG, Emmenbrucke, Germany

Table 1. Chemicals.

### 5.2 Antibodies

Antibody	Manufacturer
Monoclonal mouse anti-human type-II collagen IgG	Acris, Hiddenhausen, Germany
Biotinylated anti-mouse antibody	Vector Laboratories, Burlingame, California, USA

Table 2. Antibodies.

### 5.3 Solutions and buffers

Solution and buffer	Ingredients	Weight or volume
Blocking buffer	BSA	6 ml
	PBS	200 ml
DAB solution	H <sub>2</sub> O	5 ml
	Buffer (PH 7.5)	2 drops
	DAB substrate reagent	4 drops
	H <sub>2</sub> O <sub>2</sub>	2 drops
Fast green solution	Fast green	200 mg
	H <sub>2</sub> O	ad 1000 ml
Descaling solution	Natrium-Citrate	100 g
	Formic acid (90%)	250 ml
	H <sub>2</sub> O	ad 750 ml
Eosin solution	Eosin G	10 g
	H <sub>2</sub> O	Ad 2000 ml
	KH <sub>2</sub> PO <sub>4</sub>	9.07 g
	Na <sub>2</sub> HPO <sub>4</sub>	11.86 g
Formalin solution (PH 7.4)	Formalin-stock solution	140 ml
	H <sub>2</sub> O	ad 1000 ml
Hamatoxylin solution (according to Harris)	Haematoxylin	10 g
	Ethanol (100%)	120 ml
	Sodium iodate	10 g
	ALKSO <sub>4</sub>	200 g
	H <sub>2</sub> O	ad 2000 ml
HCl solution	HCl (40%)	5.4 ml
	H <sub>2</sub> O	ad 200 ml
PBS	KCL (PH 7.2)	2.7 mM
	K <sub>2</sub> HPO <sub>4</sub>	1.7 mM
	NaCl	136 mM
	Na <sub>2</sub> HPO <sub>4</sub> -7H <sub>2</sub> O	10 mM
	Safranin orange solution	Safranin-Orange
Trypsin solution (0.1%)	H <sub>2</sub> O	ad 1000 ml
	Trypsin-stock solution (25%)	800 µl
	PBS	ad 200 ml
Trypsin stock solution	Trypsin	25% (V/V)
	PBS	75% (V/V)
Hydrogen peroxide solution (0.3%)	H <sub>2</sub> O <sub>2</sub>	0.6 ml
	H <sub>2</sub> O	200 ml

Table 3. Recipes of solutions and buffers.

### 5.4 Softwares

Software	Company
ImageJ	National Institutes Health, Maryland, USA
Adobe Photoshop	Adobe Systems, Mountain View, California, USA
AnalySIS	Soft Imaging System GmbH, Münster, Germany
CTAnalyzer	Bruker Skyscan, Kontich, Belgium
SPSS	IBM SPSS 20; SPSS Inc., Chicago, Illinois, USA
Microsoft Excel	Microsoft, Redmond, Washington, USA

Table 4. Softwares.

## 5.5 Instruments and materials

Instruments and materials	Manufacturer
Scalpel handle	Aesculap, Tuttlingen, Germany
Scalpel blade	KLS Martin, Tuttlingen, Germany
Biopsy punch	Kai Europe, Solingen, Germany
Disposable electrode handle	Erbe, Tübingen, Germany
High-frequency generator	Erbotom ICC 350, Erbe, Tübingen, Germany
Ring curette	Aesculap, Tuttlingen, Germany
Microfracture awl	Aesculap, Tuttlingen, Germany
Army-navy retractor	Aesculap, Tuttlingen, Germany
Collier-Anderson forceps	Aesculap, Tuttlingen, Germany
De Bakey-Collier forceps	Aesculap, Tuttlingen, Germany
De Bakey needle forceps	Aesculap, Tuttlingen, Germany
Mixter forceps	Aesculap, Tuttlingen, Germany
Weitlaner retractor (self-retaining)	Aesculap, Tuttlingen, Germany
Bent Hohmann retractor	Aesculap, Tuttlingen, Germany
TC Mayo scissors	Aesculap, Tuttlingen, Germany
TC Mayo Masson needle holder	Aesculap, Tuttlingen, Germany
Nelson Metzenbaum scissors	Aesculap, Tuttlingen, Germany
Polypropylene suture	Prolene, Ethicon, Somerville, New Jersey, USA
Skin disinfectant (Polyvidon-iodine, propran-1-ol solution)	Braunoderm, B. Braun, Melsungen, Germany
Antiseptic spray	Aluminium-Spray, Albrecht, Aulendorf, Germany
Fentanyl pain patch	Durogesic, Janssen-Cilag, Neuss, Germany
Syringe (20 ml)	Braun-Inject, B. Braun, Melsungen, Germany
Sterile drape (75 x 90 cm)	Foliodrape, Paul Hartmann AG, Heidenheim, Germany
Sterile drape (50 x 60 cm)	Secu-Drape, Sengewald, Germany
Sterile drape (75 x 75 cm)	Raucodrape, Lohmann & Rauscher, Rengsdorf, Germany
Electric hair shaver	Electra II, Aesculap, Tuttlingen, Germany
Micro pipette (20 µl)	Eppendorf, Hamburg, Germany
Pipette tips (100 µl)	Eppendorf, Hamburg, Germany

Table 5. Instruments and materials for animal surgery.

## 5.6 Equipments

Equipment	Manufacturer
Autoclave AMA-240	Astell, Sidcup, England
Canon Powershot A480	Canon, Tokyo, Japan
Digital camera CC-12 (on Microscope BX-45)	Soft Imaging System, Münster, Germany
Embedding machine EG 1140-C	Leica, Nussloch, Germany
Refrigerator -20 °C	Bosch, Gerlingen-Schillerhöhe, Germany
Refrigerator -74 °C Platinum 550	Angelantoni Industrie, Massa Martana PG, Italy
Incubator CB 150 (37 °C)	Binder, Tuttlingen, Germany
Magnetic stirrer RH basic 2	IKA, Staufen, Germany
Microfocus X-ray scanner Skyscan 1172	Skyscan, Kontich, Belgium
Microscope BX-45	Olympus, Hamburg, Germany
Microscope CK-2	Olympus, Hamburg, Germany
Cover plate (Plate sealer)	MD Bioproducts, Saint Paul, USA
Rotational microtome RM 2135	Leica, Nussloch, Germany
Heat plate HI 1220	Leica, Nussloch, Germany
Water bath HI 1210	Leica, Nussloch, Germany

Table 6. Equipments used in the tissue process and analysis.

## **6 METHODS**

### **6.1 Study design**

The study designs are given corresponding to the hypotheses. To develop the algorithm and to compare it with the best existing evaluation method, we used samples from minipigs and sheep (an unrelated study performed by Prof. Madry). To investigate and compare the outcome of debridement, microfracture, and bone marrow aspirate enhanced microfracture, we only use the samples from the minipigs. All animal experiments were conducted in agreement with the national legislation on protection of animals and the National Institutes of Health (NIH) Guidelines for the Care and Use of Laboratory Animals (NIH Publication 85-23, Rev 1985). The study was approved by the Saarland University Animal Committee according to the German guidelines. The animal surgeries were performed in the Institute for Clinical and Experimental Surgery, University of Saarland, Homburg/Saar, Germany by Prof. Madry with Liang Gao being the first assistant.

### **6.2 Methods for developing a novel algorithm for the precise analysis of subchondral bone changes**

#### **6.2.1 Systematic review of the current analyzing methods**

For summarizing the current methods in evaluating the postoperative status of the subchondral bone, a systematic review of subchondral bone changes following microfracture treatment in animal models was performed according to Preferred Reporting Items for Systematic Reviews and Meta-Analyses (PRISMA) standards and a PRISMA checklist (MOHER et al., 2009). The MEDLINE database was searched through PubMed between 1950 and January 06, 2016. Inclusion criteria for the search included English language, animal studies with microfracture treatment, and evaluation of the subchondral bone.

#### **6.2.2 Animal studies**

For developing a novel algorithm for the precise analysis of subchondral bone changes,

both minipigs and sheep were used. All minipigs studies were performed as described below in 6.3.2 with the exception that no bone marrow aspirate (BMA) was applied. For the sheep, they received microfracture surgery in the knee with the same surgical instruments as for the minipigs surgery (ORTH et al., 2016).

Full-thickness chondral defects were created in the femoral trochlea of adult minipigs (n = 5 animals, 2 defects per animal; age: 18-22 months; average body weight: 28.9-41.7 kg) and the medial femoral condyle of adult sheep (n = 5 animals, 1 defect per animal; age: 26-42 months; average body weight: 72.7-81.5 kg). The borders of the cartilage defects were outlined with a circular (4-mm diameter in minipigs) or rectangular punch (4 x 8 mm in sheep). Next, the hyaline cartilage was removed with a curette to create full-thickness chondral defects that were circular in minipigs and rectangular in sheep. The calcified cartilage layer was meticulously removed to expose the subchondral bone plate. Microfracture holes were created in the subchondral bone plate using a microfracture awl in a standardized fashion. Three holes per defect in minipigs and six holes per defect in sheep were introduced. Holes were always orientated perpendicular to the bone surface and distributed evenly within the defects (resulting in a similar distance between holes) (STEADMAN et al., 2001). The applied microfracture awl consists of a conical head and a cylindrical body (1.2 mm diameter). A penetration stop ensured a standardized penetration depth (ORTH et al., 2016).

### **6.2.3 Micro-CT imaging of the subchondral bone following microfracture treatment**

All 2D consecutive micro-CT datasets from both minipig and sheep studies of the repair of articular cartilage defects were used. Osteochondral specimens containing the defects were scanned along the axis of each microfracture hole in a micro-CT scanner (Skyscan 1172, Skyscan, Kontich, Belgium) as previously described (ORTH et al., 2012c). The device possesses a moveable 10-MP camera and an X-ray tube (< 5  $\mu\text{m}$  spot; Hamamatsu, Hamamatsu City, Japan), allowing for a maximal nominal resolution below 0.8  $\mu\text{m}$ .

The X-ray tube voltage was 70 kV, and the current was 140  $\mu\text{A}$ . All specimens were scanned within 70% ethanol at a spatial resolution of 15  $\mu\text{m}$ . X-ray projections were

obtained at 0.4 ° intervals with 1770 ms exposure time and a combined 0.5 mm aluminum/copper filter interposed. Ring artifact correction, frame averaging, and random movement were engaged (4, 3, and 15, respectively, no units). The reconstructed dataset was segmented with a modified Feldkamp cone-beam algorithm (FELDKAMP et al., 1989).

In order to mimic bone as closely as possible, the thresholding levels of gray values were set for segmentation of the binary images (range: 89-255). To express gray values as bone mineral density (BMD), calcium hydroxyapatite (CaHA) phantom rods immersed in 70% ethanol with known BMD values (250 and 750 mg CaHA/cm<sup>3</sup>) were employed for calibration.

#### **6.2.4 Introduction of the algorithm for analysing of subchondral bone changes**

The precise definition of each type of subchondral bone change was provided and a novel micro-CT based algorithm was proposed for evaluating these subchondral bone changes. This algorithm was then applied and validated with the above-mentioned micro-CT datasets from both minipig and sheep models.

#### **6.2.5 Inter-rater reliability of the algorithm**

To test the reliability of this algorithm, 30 representative image sets with subchondral bone alterations from the sheep and minipig models were chosen by observer one (Patrick Orth) and blinded for the following evaluation. Observers two (Liang Gao) and three (Lars Goebel) independently scored the images using the novel algorithm. After completion, the number of observed agreements and Cohen's kappa were calculated (COHEN, 1960).

#### **6.2.6 Comparison of the algorithm with the most comprehensive existing method**

To evaluate the quality of the new algorithm, the datasets of defects from both animal models were evaluated applying the most comprehensive existing categorical scoring system (Table 7) (CHEN et al., 2011b). The results of the best existing method were compared with that of the present algorithm.

Variables	Point scale
Bone overgrowth above projected tidemark	
Proud throughout (exhibited in > 90% of defect width and length)	0
Proud throughout (exhibited in 5% to 90% of defect width and length)	1
Little or none (exhibited in < 5% of defect width and length)	2
Presence of residual holes or cyst	
Subchondral bone cyst or large merged hole	0
3 or more holes	1
2 holes	2
1 hole	3
No visible holes	4
Bone resorption	
Significant	0
Moderate	1
Little or none	2

*Table 7. The Chen scoring system for a semi-quantitative assessment of the subchondral bone alterations: the presence of intra-lesional osteophyte (termed "bone overgrowth above projected tidemark"), residual microfracture holes or subchondral bone cyst formation, and bone resorption. Only the relevant variables 1-3 from the original Chen score are shown (CHEN et al., 2011b).*

## **6.3 Methods applied to test the early loss of subchondral bone following bone marrow aspirate enhanced microfracture**

### **6.3.1 Treatment groups**

Standardized circular (diameter 4 mm) full-thickness chondral defects in the trochlear groove of minipigs were treated by (1) debridement (debridement group), (2) debridement and microfracture (microfracture group), and (3) debridement, microfracture, and bone marrow aspirate (enhanced microfracture group) (Figure 5). In the debridement group, the entire calcified cartilage layer was meticulously debrided down to the subchondral bone plate. In the microfracture group, following an identical debridement, three uniform microfracture holes with standardized diameter of 1.2 mm and depth of 5.0 mm were introduced. Here, a custom-made microfracture awl with a straight trihedral cutting tip and a penetration stop was used. Defects of the enhanced microfracture group were treated as described above with an addition of a layer of fresh autologous bone marrow aspirate, which was retrieved from the ipsilateral proximal tibia. Osteochondral repair was assessed at 4 weeks postoperatively using established macroscopic, histological, immunohistochemical, and micro-computed tomography analyses (ORTH, MADRY, 2015). The cartilage and subchondral bone adjacent to the treated osteochondral region served as internal controls.

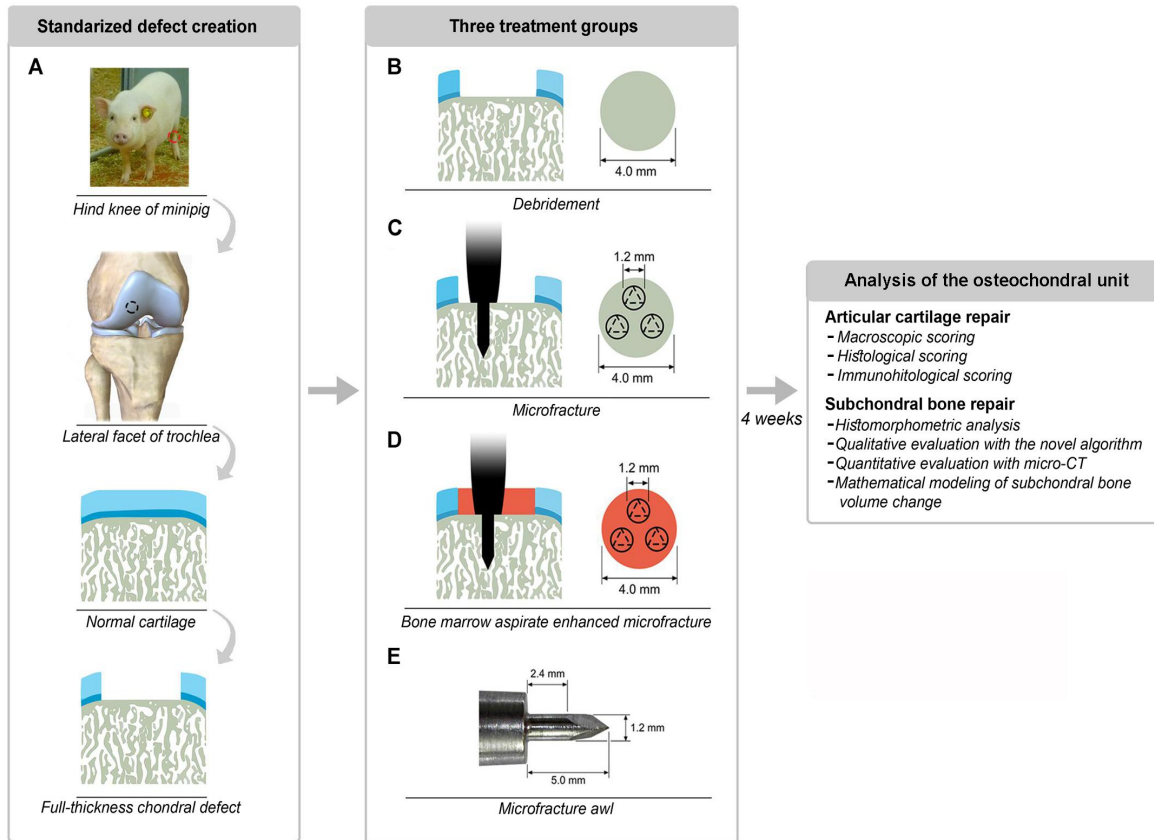


**Figure 5.** Schematic drawing depicting the study design. (A) Standardized circular (diameter 4 mm), full thickness chondral defects were created in the lateral trochlear facet of the hind legs of minipigs. Three treatments were applied including debridement alone (debridement group) (B), debridement and microfracture (microfracture group) (C), and debridement and bone marrow aspirate enhanced microfracture (enhanced microfracture group) (D). Top views of defects following the three treatments are shown at the right side. Different regions of the osteochondral unit are shown with various colors: light blue (articular cartilage), dark blue (calcified cartilage), grey (subchondral bone), and red (bone marrow aspirate). (E) The trocar-shaped microfracture awl tip used in the microfracture procedure consists of a distal trihedral head (length 2.6 mm), a middle cylindrical body (length 2.4 mm, diameter 1.2 mm), and a proximal penetration stop, allowing for a standardized penetration depth of 5.0 mm. Animals were sacrificed at 4 weeks postoperatively and both articular cartilage and subchondral bone were analyzed using previously established approaches. Figure adapted from (GAO et al., 2017b).

### 6.3.2 Animal surgeries

#### Animals

Eleven skeletally mature, healthy female Göttingen minipigs with an age ranging between 18 and 22 months and body weight between  $38.9 \pm 5.3$  kg were used. Animals were continuously monitored by a veterinarian, fed a standard diet, and received water ad libitum. The minimal sample size calculation was performed as previously described (ORTH et al., 2013). In 5 minipigs, 1 defect per animal was created and treated with

debridement alone. In another 6 minipigs, 2 defects per animal were created ipsilaterally, and treated with microfracture or bone marrow aspirate enhanced microfracture, respectively.

### ***Anesthesia***

Following a 12-hour fast, the animals were sedated with intramuscular injection of 30 mg ketamine/animal (Ketanest S, Pfizer, Berlin, Germany), 2 mg xylazine/animal (Rompun, Bayer, Leverkusen, Germany), and 1 mg atropine/animal (B. Braun, Melsungen, Germany), and endotracheally intubated after intravenous administration of 20 ml of 2% propofol (AstraZeneca, Wedel, Germany). General anesthesia was maintained by inhalation of 1.5% isoflurane (Baxter, Unterschleißheim, Germany) and intravenous administration of propofol (6-20 mg/kg BW/h). Unilateral surgery was performed in the hind legs with right and left knees alternating within groups.

### ***Positioning and draping***

The animal was placed in a supine position with both hind limbs untied. The skin of both hind limbs was shaved with an electric shaver. No tourniquet was used, and limbs were disinfected for about 10 minutes with a 10% iodine solution (Braunoderm, B. Braun, Melsungen, Germany). The distal one third of the limbs and claws were wrapped with impermeable plastic tapes. The abdomen of the animals was covered by the ordinary linen drapes (Raucodrape, Lohmann & Rauscher, Rengsdorf, Germany) and the limbs were put through fenestrated sheets (Figure 6). Additional drapes were placed to cover the proximal, lateral and medial borders of the stifle joints, leaving a triangular open region for operation (Secu-Drape, Sengewald, Germany). The sheets were then secured with towel clips and an adhesive transparent plastic drape was then applied to cover the entire operation zone of both hind limbs. During the wrapping and draping, full extension of hip and stifle joints was maintained by axially pulling both hind limbs to avoid the contamination of the disinfected regions and shifting of the drapes.

### ***Surgical approach***

Full extension of the limb was achieved and maintained by axially pulling by an assistant. A straight skin incision (4-5 cm) over the patellar ligament was established. The

subcutaneous tissue was dissected in line of the incision to expose the patella ligament. The arthrotomy was then performed by cutting along the medial border of the patellar tendon to expose the lateral facet of the femoral trochlea (Figure 7A).

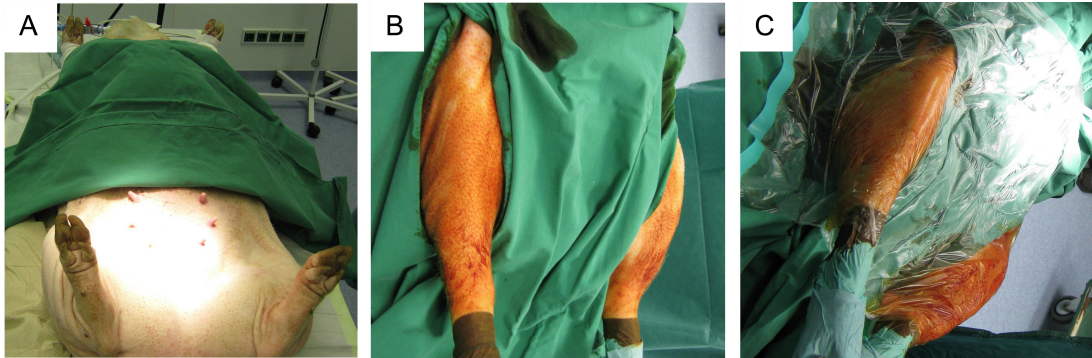
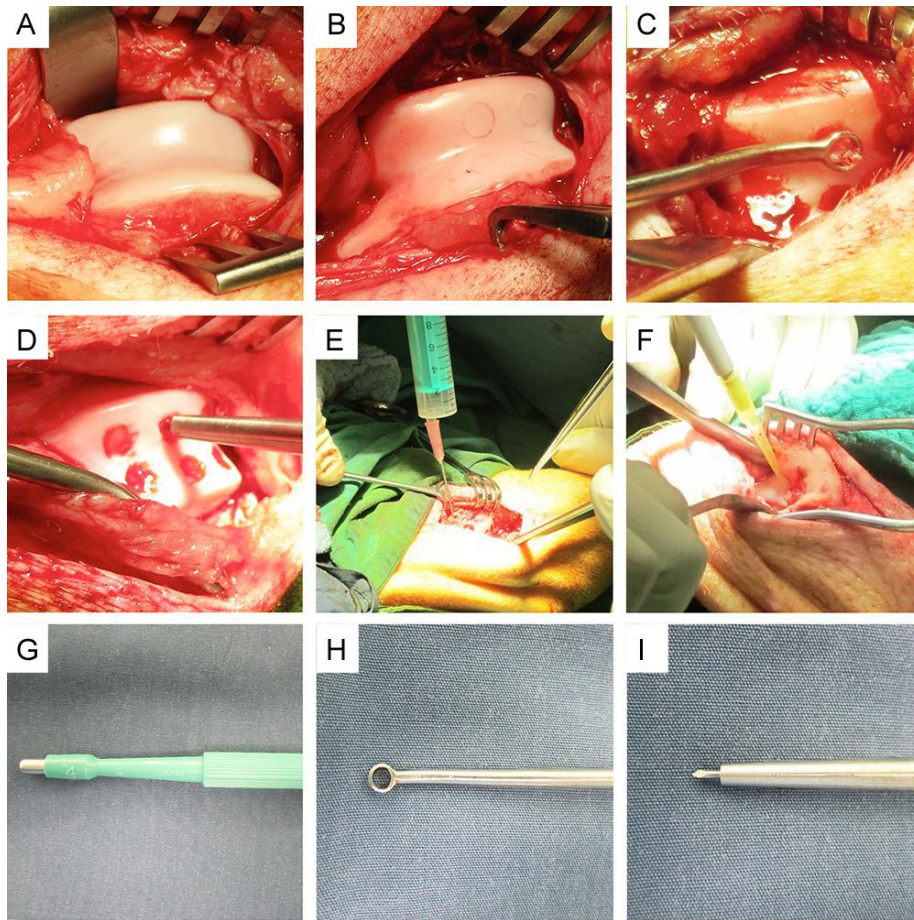


Figure 6. Positioning and draping for the animal surgery.

Standardized circular (diameter 4 mm) full-thickness chondral defects (defect n = 17) were created on the lateral trochlea facets with a custom-machined skin punch (Kai Europe, Solingen, Germany) (Figure 7B). In the debridement group (n = 5), defects only received the debridement treatment. The entire calcified cartilage layer was meticulously debrided down to the subchondral bone plate using a ring curette (Aesculap, Tuttlingen, Germany) (Figure 7C). Special care was taken to keep the subchondral bone plate intact without creating any abrasion. In the microfracture group (n = 6), following the identical debridement, three uniform microfracture holes (diameter 1.2 mm, depth 5.0 mm) were then introduced in a standardized manner, perpendicular to the joint surface and evenly distributed within the defect (Figure 7D). A custom-made microfracture awl with a straight trihedral cutting tip and a penetration stop was used to standardize the penetration depth to 5.0 mm (Aesculap, Tuttlingen, Germany). In the enhanced microfracture group (n = 6), following debridement and microfracture, an additional layer of fresh autologous bone marrow aspirate retrieved from the ipsilateral medial proximal tibia was injected onto the bottom of the defects treated with debridement and microfracture (25  $\mu$ l per defect) (Figure 7E;F). Joints were closed in layers with the polypropylene sutures (Prolene, Ethicon, Somerville, New Jersey, USA).



*Figure 7. Key procedures and instruments for the chondral defect creation and treatment. (A) Following the arthrotomy, exposure of the distal two thirds of the lateral and medial facet of the femoral trochlea is achieved. (B) Standardized circles (diameter 4 mm) were lined on the lateral facets of the femoral trochlea with a custom-made skin punch. (C) The full-thickness defects are generated by removal of the cartilage tissue within the lined circles and meticulous debridement of the calcified cartilage layer with a ring curette to the level of subchondral bone plate. Special care is taken to keep the subchondral bone plate intact. (D) For defects from the microfracture or enhanced microfracture groups, three microfracture holes were introduced in each defect with a microfracture awl. (E) Bone marrow aspirate was harvest from the ipsilateral medial proximal tibia with a syringe (20 ml). (F) For defects from the enhanced microfracture group, 25  $\mu$ l bone marrow aspirate was injected into each defect following the microfracture treatment. (G) Skin punch (Kai Europe, Solingen, Germany) for lining the defects. (H) Ring curette (Aesculap, Tuttlingen, Germany) for performing the debridement procedure. (I) Microfracture awl (Aesculap, Tuttlingen, Germany). Except for defects in inferior region of the lateral facet of trochlea, the resting defects shown in (B) and (D) are used for other unrelated studies. Detailed parameters of the microfracture awl are illustrated in Figure 5E.*

### ***Postoperative care***

The animals were allowed immediate postoperative full weight-bearing. Fentanyl pain patch (Durogesic, Janssen-Cilag, Neuss, Germany) with a release rate of 100 µg/ h was applied for 72 hours postoperatively. If needed, 4 mg/kg BW caprofen (Rimadyl, Pfizer Animal Health, Berlin, Germany) were admitted orally during the postoperative period.

### ***Animal scarification and specimen harvesting***

Animals were sacrificed in general anesthesia at 4 weeks postoperatively. Digital photographs of the entire defect area (n = 17) were obtained under standardized illumination conditions (SELLERS et al., 1997) at the time of animal sacrifice to allow for macroscopic evaluation. Osteochondral specimens containing the cartilage defects were dissected in a standardized manner, placed in 4% formalin (Sigma, Taufkirchen, Germany) for 24 hours and stored in 70% ethanol (Roth, Karlsruhe, Germany) thereafter. Fresh specimens were first scanned with the micro-CT, then decalcified with 5% formic acid, trimmed, and proceeded for further histological and immunohistochemical evaluations.

### **6.3.3 Evaluation of articular cartilage repair**

#### ***Macroscopic scoring***

Photographs for the macroscopic grading of articular cartilage repair were independently evaluated by two blinded experienced investigators using the inverse scoring system (Table 8) by Goebel *et al.* (20 = no repair; 0 = normal articular cartilage) (GOEBEL et al., 2012).

#### ***Histological scoring***

For the histological evaluation, sections (4 µm) were obtained using a microtome cutting from the center of each paraffin-embedded specimen and stained with the safranin orange/fast green (safranin O) and the hematoxylin and eosin (HE) (GILLE et al., 2010b; ORTH et al., 2015). A total of 136 stained sections (8 sections per defect) were evaluated by two independent investigators using the complex cartilage repair score (Table 9) described by Sellers *et al.* (SELLERS et al., 1997). The total score ranged from 31 (empty defect without repair tissue) to 0 points (complete regeneration).

Parameter	Items	Points
Color of the repair tissue	Hyaline or white	0
	Predominantly white (>50%)	1
	Predominantly translucent (>50%)	2
	Translucent	3
	No repair tissue	4
Presence of blood vessels in the repair tissue	No	0
	Less than 25% of the repair tissue	1
	25-50% of the repair tissue	2
	50-75% of the repair tissue	3
	More than 75% of the repair tissue	4
Surface of the repair tissue	Smooth, homogeneous	0
	Fibrillated	1
	Incomplete new repair tissue	2
	No repair tissue	3
Filling of the defect	In level with adjacent cartilage	0
	>50% repair of defect depth or hypertrophy	1
	<50% repair of defect depth or hypertrophy	2
	0% repair of defect depth	3
	Subchondral bone damage	4
Degeneration of adjacent articular cartilage	Normal	0
	Cracks and/or fibrillations in integration zone	1
	Diffuse osteoarthritic changes	2
	Extension of the defect into the adjacent cartilage	3
	Subchondral bone damage	4
Total points		20

Table 8. The macroscopic scoring system for the macroscopic description of articular cartilage repair (GOEBEL et al., 2012).

### **Immunohistochemical grading of type-II collagen**

For the evaluation of immunoreactivity to type-II collagen, the paraffin-embedded sections were submerged in 0.3% hydrogen peroxide (Sigma, Taufkirchen, Germany) for 30 min. After washing with PBS, sections were incubated in 0.1% trypsin for 30 minutes, washed with PBS and blocked with 3% bovine serum albumin in PBS (blocking buffer) for 30 minutes. The sections were then incubated with a 1/50 dilution of a monoclonal mouse anti-human type-II collagen IgG (Acris, Hiddenhausen, Germany) in blocking buffer for 24 hours at 4°C, washed and exposed to a 1/100 dilution of a biotinylated anti-mouse antibody (Vector Laboratories, Burlingame, California, USA) for 1 hour at room temperature. The sections were washed, incubated with avidin-biotin-peroxidase reagent for 30 minutes, and then exposed to the diaminobenzidine (DAB reagent; Sigma, Deisenhofen, Germany). Immunoreactivity to type-II collagen in the repair tissue was compared with that of the adjacent articular cartilage, serving as positive internal control, and reported as previously described (0: no immunoreactivity; 1: significantly weaker; 2:

moderately weaker; 3: similar; 4: stronger immunoreactivity) (ORTH, MADRY, 2015).

All microscopic images were attained by an optical microscope (BX-45; Olympus, Hamburg, Germany) mounted with a digital charge coupled device (CCD) camera system. The obtained images were then analyzed with the analySIS software (Soft Imaging System GmbH, Münster, Germany) applying standardized parameters.

### **6.3.4 Evaluation of subchondral bone reconstitution**

#### ***Histomorphometric analysis***

Paraffin embedded sections were processed for the Masson-Goldner trichrome staining as previously described (VAN 'T HOF et al., 2003). A standardized region of interest (ROI) was set up covering the trabecular region of the subchondral bone underlying the treated defects with 3.0 mm depth and 4.0 mm width (Figure 8). The entire ROI was divided into the same sized superficial, middle and deep zones (each zone 1.0 mm × 4.0 mm). Quantitative histomorphometry was performed in sections through the central region of defects using Map\_Bonemicrostructure, a plugin for ImageJ 1.50 (National Institutes Health, Maryland, USA) (SCHNEIDER et al., 2012), and Adobe Photoshop CC 2015 (Adobe Systems, Mountain View, California, USA) (EGAN et al., 2012). Map\_BoneMicrostructure calculated the following standard bone histomorphometry parameters on a digitalized trabecular bone surface according to the “parallel plates model”: bone volume fraction (BV/TV; %), mean trabecular thickness (Tb.Th;  $\mu\text{m}$ ), mean trabecular separation (Tb.Sp;  $\mu\text{m}$ ), and mean trabecular number per length unit (Tb.N; 1/mm). Osteoclast and osteoblast density was determined and quantified by the manual point counting within the 3 zones of the entire ROI using the following criteria (HAFFNER-LUNTZER et al., 2016) (Figure 8). Criteria for the osteoclast identification involved: (1) multinuclear cell ( $\geq 3$  nuclei), (2) concave surface of bone beside the cell, and (3) larger cytoplasm than nucleus. Criteria for the osteoblast identification included: (1) cuboidal or polygonal cell without concave surface of bone beside cell and (2) space between cells and mature bone was filled by osteoid. The osteoid (new formed bone) was lined with osteoblasts and prominently vascularized between cells and mineralized mature bone. For each defect, the percentage of marrow cavity, original (mature) bone, new bone (osteoid), and repair tissue was quantified within two Masson-Goldner

trichrome stained sections per defect through the central region of the defect using the ImageJ software. The nomenclature, symbols, and units complied with the report of the American Society for Bone and Mineral Research Nomenclature Committee (PARFITT et al., 1987).

### **Qualitative evaluation of subchondral bone changes**

The subchondral bone plate and the subarticular spongiosa beneath cartilage defects and laterally adjacent to the defects (internal controls) were separately assessed as previously described (ORTH et al., 2012a) using a microfocused X-ray computed tomography (micro-CT) scanner (Skyscan 1172; Bruker, Belgium) with a maximal nominal resolution below 0.8  $\mu\text{m}$ .

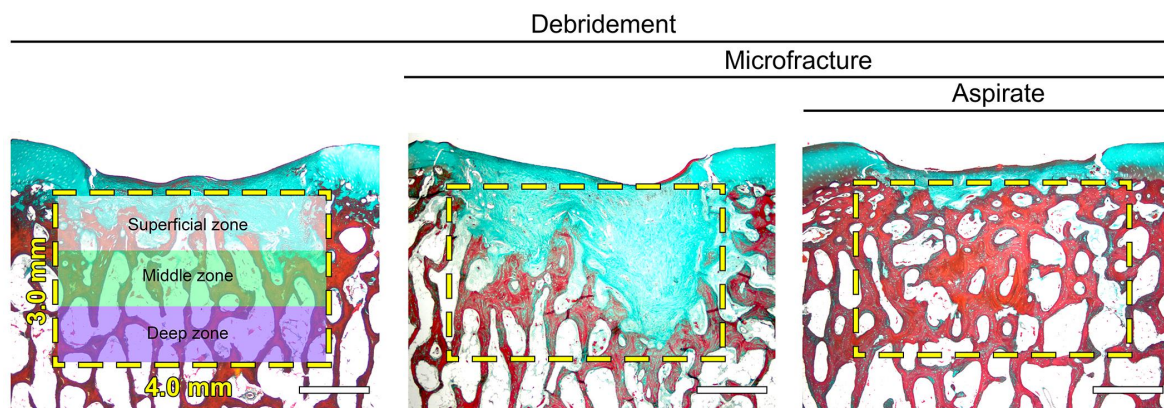


*Figure 8. Standardized regions of interest for the histomorphometric analysis. Representative images showing the pattern of subchondral bone changes in sections through the central region of defects stained with Masson-Goldner trichrome staining. The yellow dotted boxes indicate the defined region of interest (3.0 mm  $\times$  4.0 mm) selected for the histomorphometric analyses. The ROI was divided into superficial, middle and deep zone (each zone 1.0 mm  $\times$  4.0 mm). Scale bars: 1.0 mm (a). Figure reproduced from (GAO et al., 2017b).*

Variable	Items	Points
1. Filling of the defect relative to surface of normal adjacent cartilage	111 - 125%	1
	91 - 110%	0
	76 - 90%	1
	51 - 75%	2
	26 - 50%	3
	< 25%	4
2. Integration of repair tissue with surrounding articular cartilage	Normal continuity and integration	0
	Decreased cellularity	1
	Gap or lack of continuity on one side	2
	Gap or lack of continuity on two sides	3
3. Matrix staining with safranin O-fast green	Normal	0
	Slightly reduced	1
	Moderately reduced	2
	Substantially reduced	3
	None	4
4. Cellular morphology	4.1 Normal	0
	4.2 Mostly round cells with the morphology of chondrocytes	
	> 75% of tissue with columns in radial zone	0
	25 - 75% of tissue with columns in radial zone	1
	< 25% of tissue with columns in radial zone (disorganized)	2
	4.3. 50% round cells with the morphology of chondrocytes	
	> 75% of tissue with columns in radial zone	2
	25 - 75% of tissue with columns in radial zone	3
	< 25% of tissue with columns in radial zone (disorganized)	4
	4.4 Mostly spindle-shape (fibroblast-like cells)	5
5. Architecture within entire defect (not including margins) (void = empty space in the layer)	Normal	1
	1 - 3 small voids	1
	1 - 3 large voids	2
	> 3 large voids	3
6. Architecture of surface (fibrillation = cut surface)	Normal	0
	Slight fibrillation or irregularity	1
	Moderate fibrillation or irregularity	2
	Severe fibrillation or disruption	3
7. Percentage of new subchondral bone (average percent of original thickness or repair articular cartilage)	If new bone is below or above original tidemark	
	101 - 125%	1
	90 - 100%	0
	75 - 89%	1
	50 - 74%	2
	25 - 49%	3
< 25%	4	
8. Formation of tidemark (tidemark = interface cartilage/bone)	Complete	0
	75 - 99%	1
	50 - 74%	2
	25 - 49%	3
	< 25%	4

Table 9. Histological scoring system from Sellers et al (SELLERS et al., 1997).

For each osteochondral specimen, four distinct volumes of interest (VOIs) were evaluated within the subchondral bone compartment using the CTAnalyzer software (Bruker Skyscan, Kontich, Belgium) (ORTH et al., 2012a), including “subchondral bone plate-defect (SBP-defect)”, “subarticular spongiosa-defect (SAS-defect)”, “subchondral bone plate-lateral adjacent (SBP-adjacent)”, and “subarticular spongiosa-lateral adjacent (SAS-adjacent)” (Figure 9). SAS-adjacent was placed peripherally on the femoral trochlea. The total vertical depth of all VOIs was limited to 3.0 mm, and the maximal horizontal diameter of each VOI was restricted to 4.0 mm. Overlapping of VOIs was avoided.

Based on the micro-CT image dataset of each osteochondral specimen, the presence of subchondral bone alterations was described and qualitatively evaluated using the novel algorithm (GAO et al., 2016). The reported types of subchondral bone changes included intra-lesional osteophytes, residual microfracture holes, peri-hole bone resorption, and subchondral bone cysts. For intra-lesional osteophytes, the maximal height, maximal width, maximal two-dimensional (2D) area, and relative location of each osteophyte were reported. For residual microfracture holes, peri-hole bone resorption, and subchondral bone cysts, the maximal height of bone bridges (if existing), maximal horizontal diameter, maximal vertical diameter, and maximal 2D area were determined as previously described.

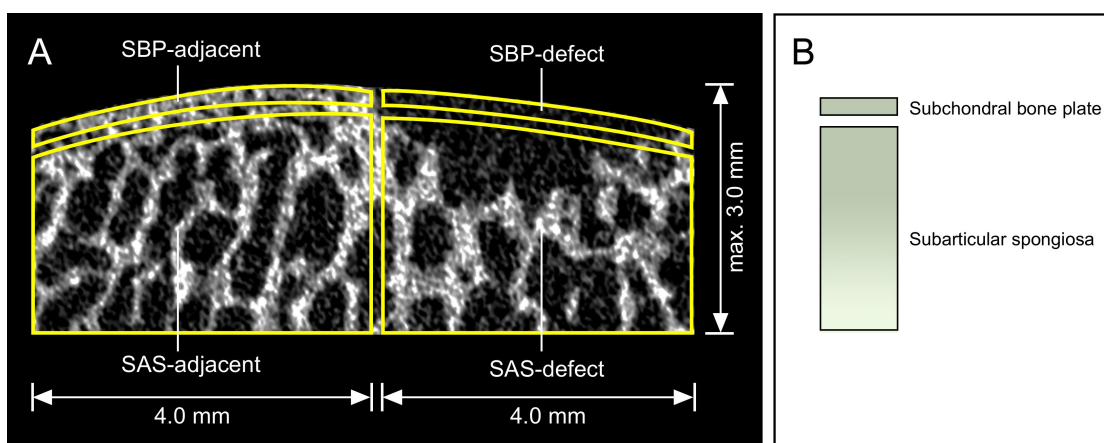


*Figure 9. Standardized regions of interest for the quantitative micro-CT evaluation of the subchondral bone. (A) Four standardized ROIs were defined on micro-CT images. SBP-defect involved exclusively the subchondral bone plate within the defect, and the underlying subarticular spongiosa (SAS-defect). SBP-adjacent and SAS-adjacent were located laterally neighboring SBP-defect and SAS-defect*

correspondingly. The maximum total vertical depth of SBP and SAS was 3.0 mm. Overlapping of individual ROIs was strictly avoided. (B) Schematic of the ROIs for subchondral bone evaluation. Note the ~10-fold larger ROI of the subarticular spongiosa compared with the subchondral bone plate. Figure reproduced from (GAO et al., 2017b).

### **Quantitative evaluation of subchondral bone changes**

For the quantitative analysis of the subchondral bone compartment, the following variables were determined within each of the four VOIs in a three-dimensional (3D) fashion (ORTH et al., 2012a): bone mineral density (BMD), bone volume fraction (BV/TV), specific bone surface (BS/BV), bone surface density (BS/TV). Cortical thickness (Ct.Th) was only reported within the subchondral bone plate, while trabecular thickness (Tb.Th), trabecular separation (Tb.Sp), trabecular pattern factor (Tb.Pf), trabecular number (Tb.N), structure model index (SMI), degree of anisotropy (DA), and fractal dimension (FD) were only determined in the subarticular spongiosa.

### **Mathematical modeling of subchondral bone volume changes**

In each treatment group, the real values of bone volume fraction (BV/TV) of SBP-defect and SAS-defect could be directly measured by the CTAnalyzer software and referred to as SBP-defect<sub>(measured)</sub> and SAS-defect<sub>(measured)</sub>, respectively.

In the debridement group, the entire subchondral bone was preserved theoretically (Figure 5A,B). Therefore, using adjacent VOIs as references, the expected value of BV/TV of SBP-defect [SBP-defect<sub>(calculated)</sub>] and SAS-defect [SAS-defect<sub>(calculated)</sub>] were determined as:

$$\text{BV/TV of SBP-defect}_{(\text{calculated})} = \text{BV/TV of SBP-defect}_{(\text{adjacent})} \quad (1)$$

$$\text{BV/TV of SAS-defect}_{(\text{calculated})} = \text{BV/TV of SAS-defect}_{(\text{adjacent})} \quad (2)$$

In the microfracture and enhanced microfracture group, the interaction between the microfracture awl and the subchondral bone was modeled (Figure 10). Here, the awl tip was composed of a distal trihedral head (length 2.6 mm), a middle cylindrical body (length 2.4 mm), and a distal penetration stop, standardizing the depth of penetration to 5.0 mm (Figure 5E). As the maximal vertical depth of VOIs of SBP-defect and SAS-defect was defined within 3.0 mm (Figure 9A; Figure 10B), and the thickness of SBP-defect was 0.1 mm (average value after 20 measurements), the volume occupied by the

awl tip within the defined VOIs (SBP-defect and SAS-defect) approximated a cylindrical configuration with a height of 3.0 mm and a base diameter of 1.2 mm (Figure 10C). Therefore,  $BV/TV$  of  $SBP\text{-defect}_{(calculated)}$  and  $SAS\text{-defect}_{(calculated)}$  were calculated as follows:

$$\begin{aligned} BV/TV \text{ of } SBP\text{-defect}_{(calculated)} = \\ BV/TV \text{ of } SBP\text{-adjacent} - BV/TV \text{ of } SBP\text{-defect}_{(3 \text{ cylinders})} \end{aligned} \quad (3)$$

$$\begin{aligned} BV/TV \text{ of } SAS\text{-defect}_{(calculated)} = \\ BV/TV \text{ of } SAS\text{-adjacent} - BV/TV \text{ of } SAS\text{-defect}_{(3 \text{ cylinders})} \end{aligned} \quad (4)$$

The subchondral bone volume changes were appraised with the actual preservation rate of the calculated bone volume fraction as the ratio of  $BV/TV$  of  $SBP/SAS\text{-defect}_{(measured)}$  to  $BV/TV$  of  $SBP/SAS\text{-defect}_{(calculated)}$ .

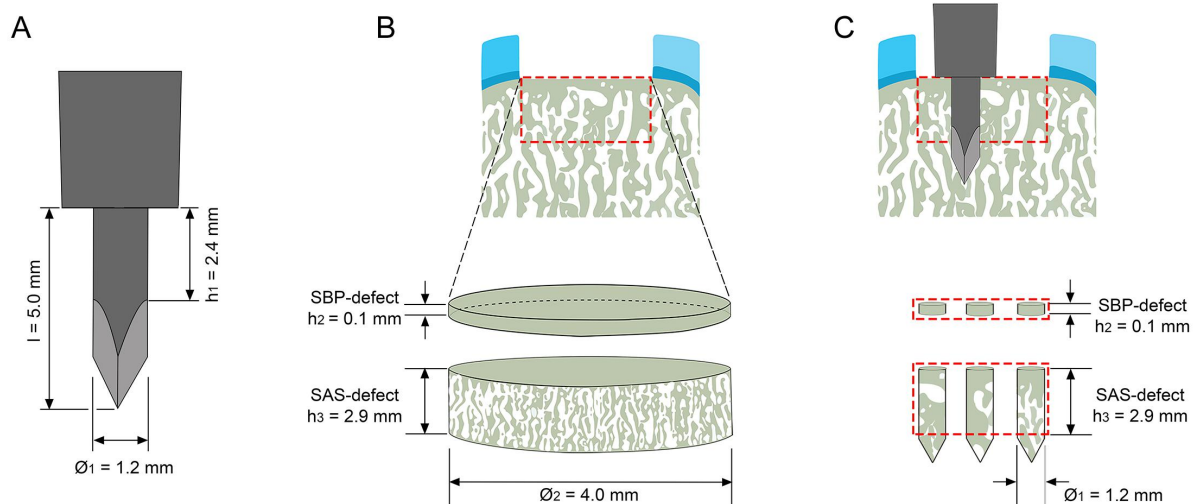


**Figure 10.** Mathematical modeling for calculating the change of subchondral bone volume following the microfracture procedure. (A) Schematic of the microfracture awl tip of Figures 5E and 7I. (B) Volume of interest (VOI) of the entire subchondral bone underlying the full-thickness chondral defect is composed of two cylinders. The top cylinder is VOI of SBP-defect with height 0.1 mm (average value of 20 measurements) and diameter 4.0 mm, and the bottom one is VOI of SAS-defect with height 2.9 mm and diameter 4.0 mm. (C) In this model, the three microfracture impactions excise the triple volume of the microfracture awl tip. Of note, when interacting with the subchondral bone, most of the trihedral head of the awl tip penetrates beyond the defined region of VOI of the subchondral bone (SBP-defect and SAS-defect). Therefore, the excised subchondral bone within the VOI of the subchondral bone is approximately equal to two cylindrical sections: one is within SBP-defect (height 0.1 mm; diameter 1.2 mm), and the other is within SAS-defect (height 2.9 mm; diameter 1.2 mm). Figure reproduced from (GAO et al., 2017b).

## 6.4 Statistical analysis

Descriptive data are expressed as mean value  $\pm$  standard deviation (SD). Units of the SI system are used where appropriate. For the study of designing of a novel algorithm, the Cohen's (unweighted) kappa was used to evaluate inter-rater agreement of nominal scaled values between two independent observers (COHEN, 1960). Calculations were performed using the Microsoft Excel 2007 (Microsoft, Redmond, Washington, USA) and the GraphPadQuickCalcs Website: <http://graphpad.com/quickcalcs/kappa1> (accessed December 16, 2015). For the study of bone marrow aspirate enhanced microfracture, the one-way ANOVA with Tukey's post-hoc test and the Mann-Whitney U test were used where appropriate. Any P value  $< 0.05$  was considered statistically significant. Calculations were performed using SPSS (IBM SPSS 20; SPSS Inc., Chicago, Illinois, USA).

## 7 RESULTS

The results are presented in 2 sections corresponding to the 2 hypotheses (page 12).

### 7.1 A novel algorithm for the precise analysis of subchondral bone changes

#### 7.1.1 Systematic review of current analytic methods

A total of 7 articles were identified in the MEDLINE database that provide analytic methods to examine the major types of subchondral bone alterations following microfracture treatment in preclinical animal models such as the formation of intralesional osteophytes ( $n = 2$ ), residual microfracture holes ( $n = 3$ ), peri-hole bone resorption ( $n = 3$ ), and subchondral bone cysts ( $n = 4$ ) (Figure 11). Most of these attempts to evaluate such morphological changes were performed by histology and radiography, including plain radiographs, MRI, and micro-CT (Table 10).

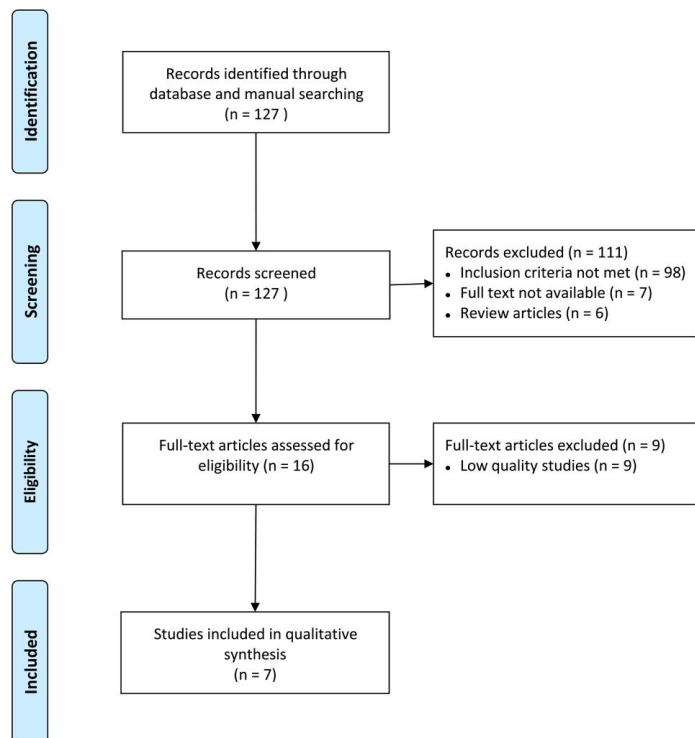


Figure 11. Flowchart of the literature searching in the MEDLINE database. Figure reproduced from (GAO et al., 2016).

Pathology	Procedure	Species	Evaluation method	Criteria of evaluation	Reference
Intra-lesional osteophyte	Microfracture; intraarticular injection of bone marrow stem cells	Horse	MRI	Scaled score ranging from 0 (normal) to 4 (severe)	(MCILWRAITH et al., 2011)
	Microfracture	Rabbit	Micro-CT	Scaled score based on the relative size of the osteophyte	(CHEN et al., 2011b)
Residual microfracture hole	Microfracture; chitosan-glycerol phosphate/ blood	Sheep	Histology	Qualitative description based on histological images	(HOEMANN et al., 2005)
	Microfracture	Rabbit	Micro-CT	Semi-quantitative description based on micro-CT and histological images	(CHEN et al., 2009a)
	Microfracture	Rabbit	Micro-CT	Scaled score based on the number of holes in micro-CT images	(CHEN et al., 2011b)
Peri-hole bone resorption	Microfracture; chitosan-glycerol phosphate/ blood	Sheep	Histomorphometry	Quantitative description based on the percentage of defect filling	(HOEMANN et al., 2005)
	Microfracture	Monkey	Histology	Qualitative description based on histological images	(GILL et al., 2005)
	Microfracture	Rabbit	Micro-CT	Scaled score ranging from 0 (significant) to 2 (little or none)	(CHEN et al., 2011b)
Subchondral bone cyst	Microfracture	Horse	Plain radiograph	Scaled score ranging from 1 (flat subcentral bone) to 4 (large lytic area deep to subchondral bone)	(FRISBIE et al., 1999)
	Microfracture; chitosan-glycerol phosphate/ blood	Sheep	Histomorphometry	Scaled score ranging from 0 to 4 based on the diameter of fibrous white tissue or tissue voids	(HOEMANN et al., 2005)
	Microfracture	Horse	Plain radiograph; MRI	Scaled score ranging from 0 (normal) to 3 (severe)	(FRISBIE et al., 2006)
	Microfracture	Rabbit	Histomorphometry; Micro-CT	Quantitative evaluation and description based on micro-CT and histological image	(CHEN et al., 2011b)

*Table 10. Systematic review of the four major types of subchondral bone changes after microfracture treatment and corresponding evaluation methods in animal models.*

### 7.1.2 Algorithm for the analysis of subchondral bone changes

To standardize the analysis of subchondral bone changes, we developed a micro-CT based algorithm consisting of two parts. In the first part (Figure 12A), all 2D consecutive micro-CT images containing the entire subchondral defect must be scanned to identify the defect region. Then the presence of subchondral bone change should be confirmed. A complete restoration of the subchondral bone of the microfractured defect was reported as “complete reconstitution”. In the defect with multiple subchondral bone lesions, each lesion should be evaluated separately. In the second part (Figure 12B), the

presence of any bone bridge between microfracture holes must first be confirmed. An osseous upward overgrowth of such a bone bridge is defined as an intra-lesional osteophyte (Figure 13A). Second, the number of microfracture holes within the osteochondral region is determined according to the relative height of the bone bridge (Figure 13B,C). Third, for each lesion, discrimination between residual microfracture holes, peri-hole bone resorption, and subchondral bone cysts is performed based on the suggested thresholds (Figure 13D). Theoretically, in the present minipig and sheep models (three holes per defect; Figure 14A), only two kinds of two-dimensional (2D) micro-CT image could be obtained: the micro-CT image displays either one single hole (Figure 14Bi-iii) or two microfracture holes (Figure 14Biv-vi).

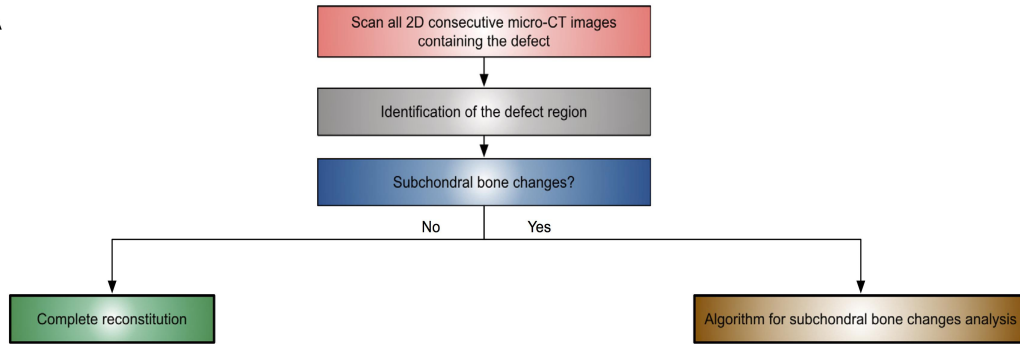
#### ***Definition of an intra-lesional osteophyte***

The intra-lesional bone bridge serves as the first evaluation index of the algorithm. By definition, a bone bridge only exists when the micro-CT image shows two microfracture holes (Figure 14Biv-vi). An intra-lesional osteophyte is determined, if a bone bridge protrudes above the projected cement line (Figure 13A) (ORTH et al., 2012b). The location of such an intra-lesional osteophyte is either central (between two microfracture holes) or peripheral (between microfracture hole and the defect edge) (ORTH et al., 2012b). The maximal height of each osteophyte ( $H_0$ ) can be measured as the vertical distance from the proximal end of the osteophyte to the projected cement line (Figure 13A). The maximal width and 2D area of each osteophyte can also be reported.

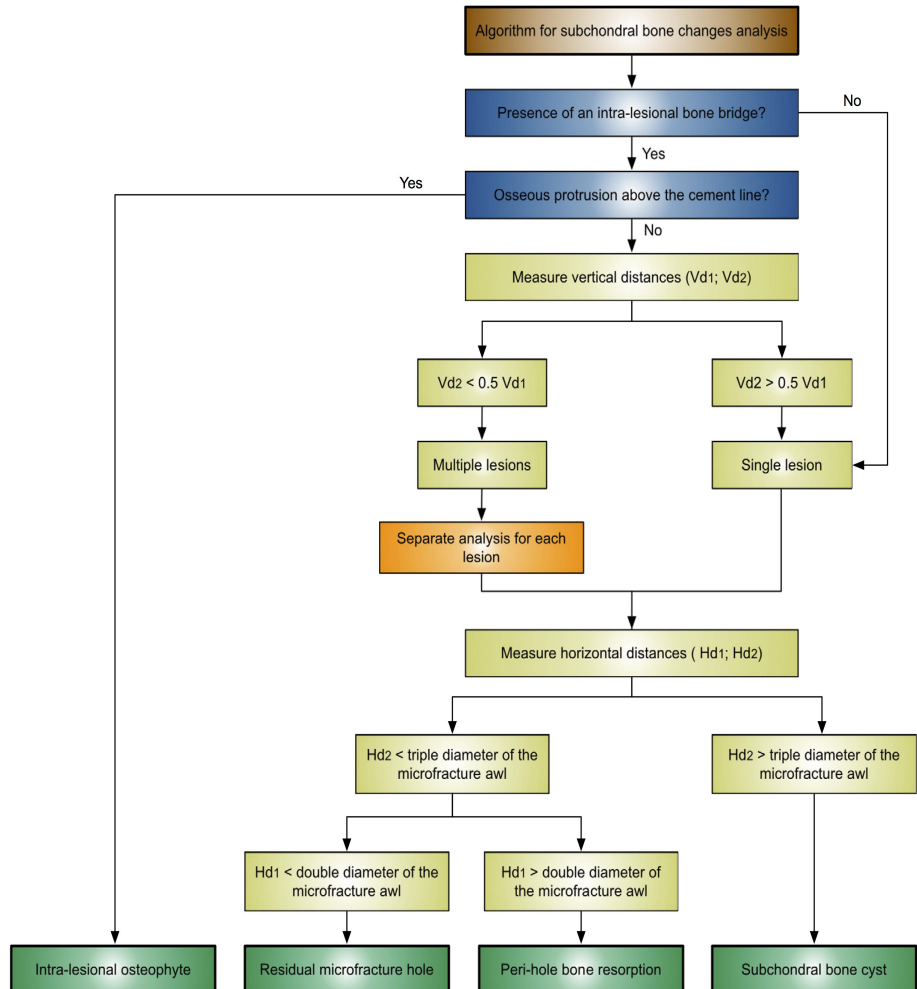
#### ***Definition of the relative bone bridge height as a means to differentiate between one or multiple holes***

The definition of the relative bone bridge height defines the number of visible microfracture holes. This bone bridge is usually located below the projected cement line, otherwise it is defined as an intra-lesional osteophyte. Such an inferiorly located bone bridge can, however, either result from bone resorption around a single microfracture hole or represent the remnant of a bone bridge between two original microfracture holes.

A



B



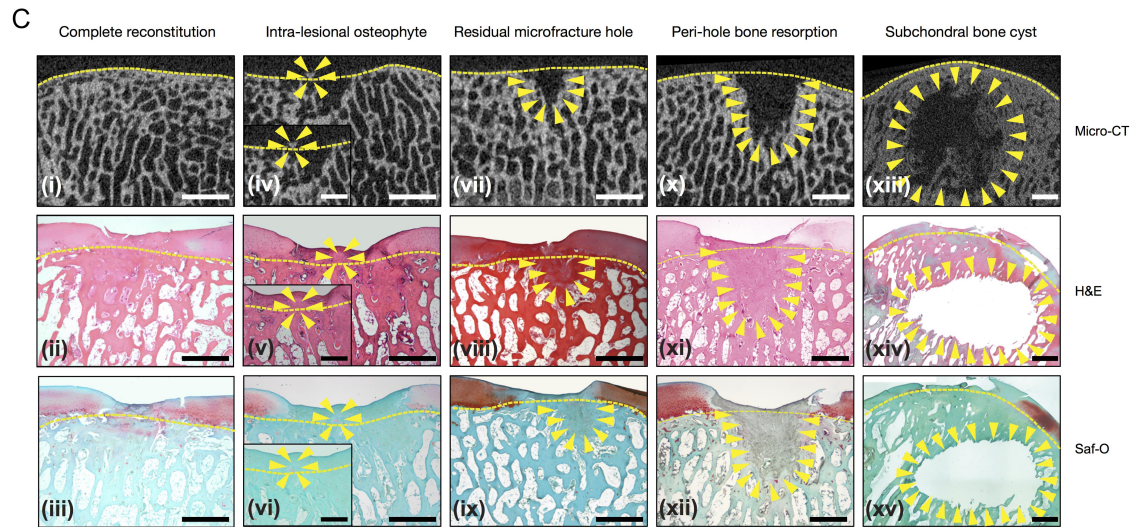


**Figure 12.** Micro-CT based algorithm for the analysis of the subchondral bone changes following microfracture treatment. (A) General workflow for analysis of subchondral bone changes based on consecutive 2D micro-CT images containing the entire subchondral bone defect. "Complete reconstitution" is reported only if the defect region resembles a normal subchondral bone structure. For a defect showing subchondral bone alterations, the second part of the algorithm has to be applied to evaluate each lesion within the defect. (B) Algorithm for analysis of the four patterns of subchondral bone changes. Of note, for a defect containing multiple lesions, each lesion should be evaluated separately, and the outcome of each lesion should also be reported respectively. For additional explanation of Vd1, Vd2, Hd1, and Hd2, please refer to Figure 13. (C) Representative micro-CT, haematoxylin and eosin (H&E), and safranin orange/fast green (safranin O) stained images of the five possible outcomes of the present algorithm applied in the minipig (i–xii) and sheep (xiii–xv) models. Insets show the higher magnification images of an intra-lesional osteophyte (iv–vi). The yellow dashed lines denote the projected cement line, and the yellow triangles define the contour of the specific subchondral bone alteration. Subchondral bone cysts were only observed in the sheep model, while the other four patterns were detected in both models. Scale bars, 10 mm (i–xv) and 5 mm (insets; iv–vi).

In order to distinguish between both circumstances, it is proposed to first calculate the relative height of the suspected bone bridge. In micro-CT images, the projected cement line is used as the apical reference line and the vertical distance (Vd) is measured from this reference line to the base of defect (Vd1) and to the top of the suspected bone bridge (Vd2) (Figure 13B). If the vertical distance from the projected cement line to the top of the suspected bone bridge is larger than half of the distance to the base of the defect ( $Vd2 > 0.5 Vd1$ ), this subchondral bone alteration is considered to originate from a single microfracture hole with surrounding bone erosion (Figure 13B). On the contrary, if the vertical distance from the projected cement line to the top of a suspected bone bridge is less than half of the distance to the base of the defect ( $Vd2 < 0.5 Vd1$ ), a persistent bone bridge is present. In this case, each of the two microfracture holes beside this persistent bone bridge requires separate analysis (Figure 13C).

---

***Discrimination between residual microfracture holes, bone resorption, and subchondral bone cysts***

To distinguish between residual microfracture holes, bone resorption, and subchondral bone cysts, the horizontal diameters (Hd) at the opening of each microfracture hole (Hd1) and the maximum horizontal diameter at half of the penetration depth (Hd2) are measured (Figure 13D). In order to allow for a comparison between holes, Hd2 is measured in parallel to Hd1 at 50% of the penetration depth of the microfracture awl. If Hd2 is less than the triple diameter of the microfracture awl, differentiation between residual microfracture hole and peri-hole bone resorption is mandatory.

Using the diameter of the microfracture awl as a constant reference standard, a residual microfracture hole is identified when the horizontal diameter of the opening of the hole (Hd1) is less than the double diameter of the microfracture awl (Figure 13D). Peri-hole bone resorption is present when Hd1 is larger than the double diameter of the microfracture awl (Figure 13Dii). Per definition, a subchondral bone cyst possesses a horizontal diameter (at 50% of the penetration depth; Hd2) larger than the triple diameter of the microfracture awl (Figure 13Diii), irrespective of Hd1. The maximal depth of each hole and cyst can be measured from the projected cement line to the base of the defect, and the maximal size may be reported as the 2D area of the empty cavity below the projected cement line and within the subchondral bone (ORTH et al., 2012b).

**7.1.3 Evaluation of the novel algorithm in two large animal models**

This algorithm for the analysis of subchondral bone changes was next evaluated in micro-CT datasets obtained from both minipig and sheep models. All defects from both studies were full-thickness chondral defects located in the trochlea of the knee joints and treated with the same custom-made microfracture awl with a 1.2 mm diameter trihedral tip (Figures 5E and 7i). Ten minipig defects with 3 microfracture holes per defect (Figure 14A) and 5 sheep defect with 6 microfracture holes per defects were randomized selected for the analysis with the present algorithm. The representative micro-CT images from both animal models are shown in Figure 15A.

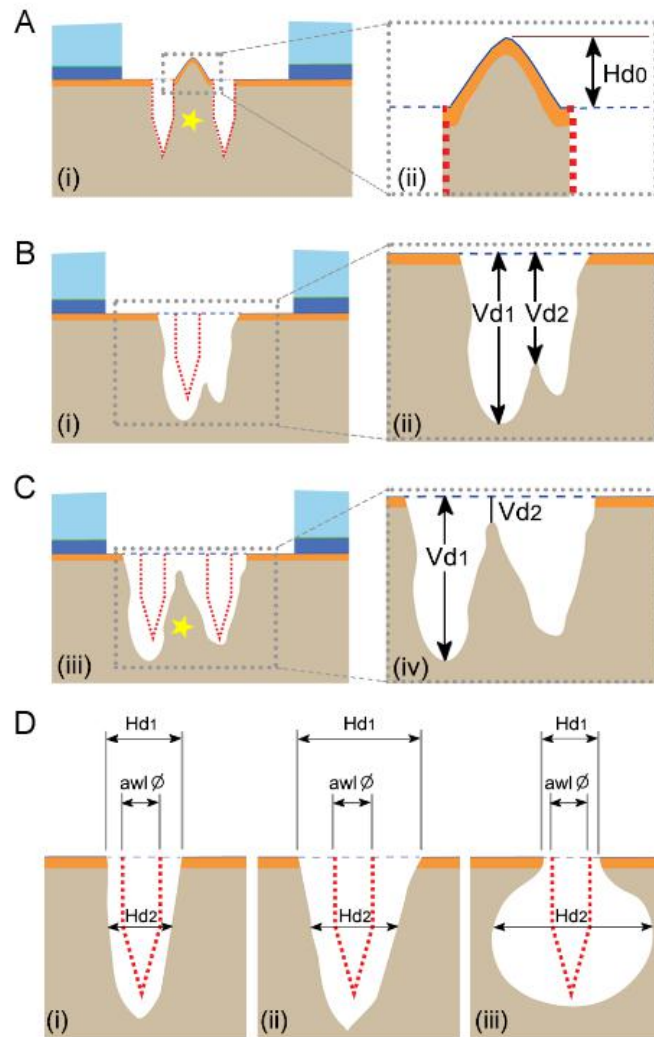
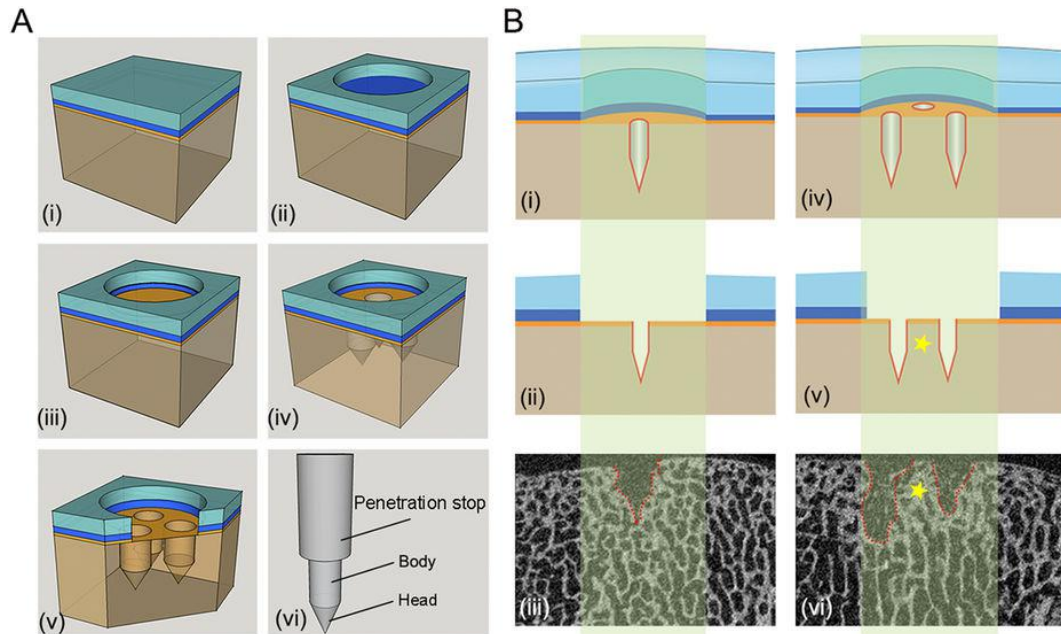


Figure 13. Identification of intra-lesional osteophytes, residual microfracture holes, peri-hole bone resorption, and subchondral bone cysts. (A) An intra-lesional osteophyte is defined as an osseous overgrowth protruding above the projected cement line. The maximal osteophyte height ( $H_0$ ) is measured as the perpendicular height from the top to the projected cement line. (B)  $V_{d1}$  and  $V_{d2}$  are the vertical distances from the projected cement line to the base of the defect and to the top of the suspected bone bridge respectively. A single microfracture hole is defined without the intra-lesional bone bridge ( $V_{d2} > 0.5 V_{d1}$ ), indicating that the subchondral bone change is derived from bone alteration surrounding the single hole. (C) Two microfracture holes are defined with a persistent bone bridge ( $V_{d2} < 0.5 V_{d1}$ ), necessitating the separate analysis of the pattern of subchondral bone change for each hole. (D) Discrimination between residual microfracture hole (i), peri-hole bone resorption (ii), and subchondral bone cyst (iii) using the relative horizontal  $\varnothing$  ( $H_{d1}$  : horizontal  $\varnothing$ , level: opening of the hole;  $H_{d2}$ : horizontal  $\varnothing$ , half of penetration depth). Using the  $\varnothing$  of the awl as reference, a residual microfracture hole (i) is defined with a small opening ( $H_{d1} < 2 \text{ awl } \varnothing$ ;  $H_{d2} < 3 \text{ awl } \varnothing$ ), and peri-hole bone resorption (ii) is defined with a large opening ( $H_{d1} > 2 \text{ awl } \varnothing$ ;  $H_{d2} < 3 \text{ awl } \varnothing$ ). (iii) Subchondral bone cyst: defined when  $H_{d2}$  is larger than  $3 \times \text{awl } \varnothing$  ( $H_{d2} > 3 \text{ awl } \varnothing$ ), regardless of  $H_{d1}$ . Red dotted lines: original location of the microfracture holes. Blue dotted lines: projected cement line. Yellow asterisks (A, C): bone bridge between two microfracture holes.  $\varnothing$ : diameter. Figure reproduced from (GAO et al., 2016).



**Figure 14.** Schematic of the microfracture procedure and representative micro-CT image patterns of the osteochondral unit in the minipig model. (A) Creation of a full-thickness chondral defect and treatment with the microfracture procedure. (i) The osteochondral unit is composed of the articular cartilage and the underlying subchondral bone. The subchondral bone is formed by the subchondral bone plate and the subarticular spongiosa. (ii) Removal of the hyaline cartilage to generate a circular chondral defect. (iii) Meticulous debridement of the calcified cartilage layer. (iv) Penetration of the subchondral bone plate with a microfracture awl to introduce three microfracture holes. (v) Detailed structure of the osteochondral unit following the microfracture treatment. (vi) Structure of the microfracture awl applied in both animal studies. The distal end has a conical head and a cylindrical body (1.2 mm diameter) and the proximal penetration stop standardizes the penetration depth. (B) Two micro-CT image patterns of the microfracture holes within defects of the minipig model. The osteochondral specimens are sectioned along their longitudinal axis by micro-CT. The light green-shaded boxes indicate the vertical cross section of the defect area. A section crossing a single microfracture hole (i,ii) corresponds to a micro-CT image (iii) displaying a single hole within the subchondral bone and a section crossing two microfracture holes (iv,v) corresponds to a micro-CT image (vi) showing two holes. The yellow asterisks (v,vi) indicate the inter-hole (intra-lesional) bone bridge. Dotted lines in (iii,vi) show the border of the residual microfracture holes. Colors of the osteochondral unit are for illustration purposes only including articular cartilage (light blue), calcified cartilage layer (dark blue), subchondral bone plate (orange), and subarticular spongiosa (brown). Figure reproduced from (GAO et al., 2016).

### **Analysis of the threshold for defining peri-hole bone resorption**

When applying the standard conditions regarding Hd1 described above for the definition of peri-hole bone resorption (Hd1 larger than the double diameter of the microfracture awl), this pathological condition was detected in 22 out of 30 microfracture holes (73%) in the minipig model and 17 out of 30 microfracture holes (57%) in the sheep model (Figure 15B). Interestingly, when elevating the threshold for peri-hole bone resorption

from 2- to 3-fold of the original awl diameter, peri-hole bone resorption was only detected in 3 out of 30 microfracture holes (10%) in the minipig model and in 7 out of 30 microfracture holes (23%) in the sheep model. When lowering the threshold for peri-hole bone resorption from 2- to 1.5-fold of the original awl diameter, peri-hole bone resorption was detected in 30 out of 30 microfracture holes (100%) in the minipig model and in 21 out of 30 microfracture holes (70%) in the sheep model (Figure 15B).

#### ***Analysis of the threshold for defining subchondral bone cysts***

Likewise, when subchondral bone cysts were defined as suggested above (Hd2 larger than the triple diameter of the microfracture awl), this pathological condition was detected in 1 out of 30 microfracture holes (3%) in the minipig model and 5 out of 30 microfracture holes (17%) in the sheep model (Figure 15C). If the threshold was elevated from 3- to 4-fold of the original awl diameter, no cyst was detected in the minipig model and only 1 subchondral bone cyst was detected in the sheep model (3%). When lowering the threshold from 3- to 2-fold of the original awl diameter, subchondral bone cysts were still detected in only 1 out of 30 microfracture holes (3%) in the minipig model but in 16 out of 30 microfracture holes (53%) in the sheep model (Figure 15C).

#### **7.1.4 Inter-rater reliability of the algorithm**

The calculation of inter-rater reliability of the algorithm for evaluation of the subchondral bone alterations revealed a total number of observed agreements of 27/30, corresponding to 90% of all observations. This resulted in a Cohen's kappa of 0.874.

#### **7.1.5 Comparison of the present algorithm with the most comprehensive scoring system**

The micro-CT datasets of defects from both animal models were then evaluated with the most comprehensive existing categorical scoring system described by Chen *et al* (Table 7) (CHEN et al., 2011b).

#### ***Intra-lesional osteophytes***

Applying the Chen score yielded point values ranging between 0 (> 90% of defect width and length) and 2 (< 5% of defect width and length). Applying the present algorithm

enabled a separated analysis of each osteophyte within the defect containing multiple intral-lesional osteophytes (e.g. in minipig #1). Furthermore, more detailed information of each osteophyte was also provided by the present algorithm such as the maximal height ( $0.312 \pm 0.119$  mm in minipigs;  $0.258 \pm 0.111$  mm in sheep), maximal width ( $0.522 \pm 0.216$  mm in minipigs;  $1.175 \pm 0.837$  mm in sheep), and maximal 2D area ( $0.204 \pm 0.184$  mm<sup>2</sup> in minipigs;  $0.247 \pm 0.167$  mm<sup>2</sup> in sheep) (Table 11).

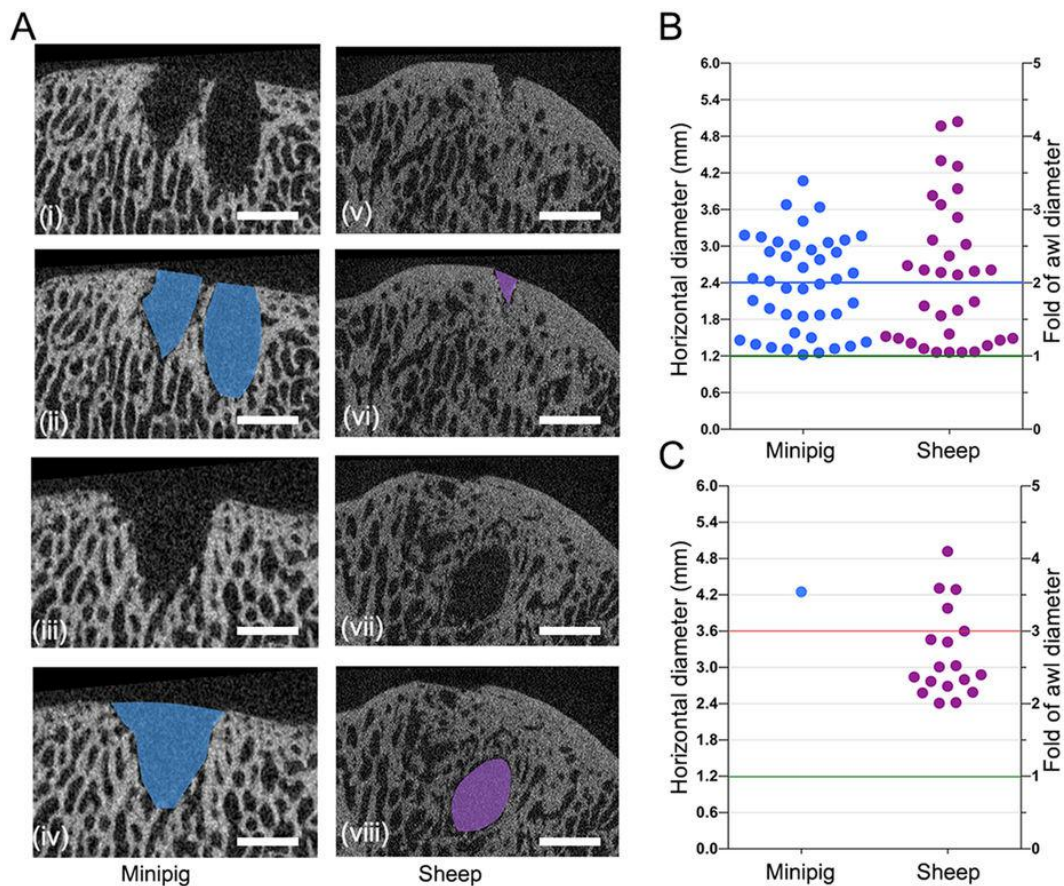


**Figure 15.** Representative micro-CT images of a single defect possessing multiple patterns of subchondral bone changes and the quantitation of the subchondral bone changes applying different thresholds of the algorithm. (A) Two suspected residual holes (i) and bone resorption (iii) were observed in the same minipig defect, and a suspected residual hole (v) and a cyst-like lesion (vii) were detected in the same sheep defect. (B) Quantitative estimation of residual microfracture holes and peri-hole bone resorption applying the algorithm with different thresholds in the minipig and sheep models. (C) Quantitative estimation of subchondral bone cysts applying the algorithm with different thresholds in the two models. The green horizontal lines (B,C) indicate the diameter of the microfracture awl as the reference standard. The red lines (B,C) indicate the triple diameter of the microfracture awl, as the suggested lower threshold value for a subchondral bone cyst. The blue horizontal line (B) indicates the double diameter of the microfracture awl, as the suggested lower threshold value of the peri-hole bone resorption. Scale bars, 2.0 mm. Figure reproduced from (GAO et al., 2016).

***Discrimination between residual microfracture holes, peri-hole bone resorption, and subchondral bone cysts***

When applying the Chen score to both datasets of defects, a precise discrimination between residual holes and peri-hole bone resorption could not be achieved (Figure 15Ai-iv). Moreover, coexistence of both residual microfracture hole and subchondral bone cyst in a single defect was detected in the 5 defects from the sheep study (Figure 15Av-viii), in which the Chen score was incapable of allocating them to a specific point scale of the score (Table 12). In contrast, the new scoring system allowed for an objective and reproducible discernment between residual holes and cysts (Figure 15Bi,ii;iv,v).

Animal type	Chen score		Present algorithm			
	Animal number	Point scale	Number of osteophytes	Maximal height (mm)	Maximal width (mm)	Maximal 2D area (mm <sup>2</sup> )
Minipig	1	1	1	0.446	0.762	0.416
Minipig	2	1	1	0.219	0.461	0.110
Minipig	3	1	1	0.271	0.342	0.086
Minipig	4	2	0	-	-	-
Minipig	5	2	0	-	-	-
Minipig	6	2	0	-	-	-
Minipig	7	2	0	-	-	-
Minipig	8	2	0	-	-	-
Minipig	9	2	0	-	-	-
Minipig	10	2	0	-	-	-
Sheep	1	1	3	0.104	0.611	0.181
				0.297	0.404	0.151
				0.189	0.745	0.093
Sheep	2	1	1	0.283	2.328	0.522
Sheep	3	1	1	0.242	1.788	0.381
Sheep	4	1	1	0.258	1.044	0.247
Sheep	5	2	0	-	-	-

*Table 11. Semi-quantitative estimation of intra-lesional osteophytes in the minipig and sheep models applying the Chen score and the present algorithm. Note that the scoring system described by Chen et al. evaluates the relative size of osteophyte (termed "bone overgrowth above the projected tidemark") to the defect (CHEN et al., 2011b). It provides a general description of the entire defect while it is not practical in defects with multiple osteophytes. The present algorithm can quantitatively estimate each intra-lesional osteophyte separately and provide details of each osteophyte.*

For the quantitative evaluation of bone resorption in both animal models, the Chen score solely allows for a subjective and general estimation of the severity of the bone resorption within an entire defect (Table 13; Figure 16Aii,iv) without discernment between bone resorption and residual microfracture holes (Figure 4Ai-iv). On the

contrary, the present continuous method is designed to yield an easy and objective evaluation of bone resorption around each original microfracture hole based on the quantitative data (Figure 16Biii,vi).

Animal type	Animal number	Residual microfracture holes		Subchondral bone cysts	
		Number	Point scale#	Number	Point scale*
Minipig	1	2	0	1	2
Minipig	2	1	n.a.	0	3
Minipig	3	2	0	1	2
Minipig	4	1	n.a.	0	3
Minipig	5	2	n.a.	0	2
Minipig	6	2	0	1	2
Minipig	7	1	n.a.	0	3
Minipig	8	2	0	1	2
Minipig	9	1	n.a.	0	3
Minipig	10	1	n.a.	0	3
Sheep	1	1	0	4	3
Sheep	2	2	0	2	2
Sheep	3	4	0	1	1
Sheep	4	2	0	1	2
Sheep	5	1	0	1	3

*Table 12. Semi-quantitative estimation of residual microfracture holes and subchondral bone cysts in the minipig and sheep models applying the Chen score. Note that the scoring system described by Chen et al. can only subjectively discriminate residual holes from subchondral bone cysts (CHEN et al., 2011b). No definite point scale can be given in specific defects with both suspected residual holes and suspected cysts inside. Discrimination between residual hole and peri-hole resorption is also impossible with the Chen score. #point scale for residual microfracture holes; \*point scale for subchondral bone cysts. n.a.: not applicable.*

Animal type	Animal number	Chen score	
		Severity of bone resorption	Point scale
Minipig	1	Significant	0
Minipig	2	Moderate	1
Minipig	3	Moderate	1
Minipig	4	Moderate	1
Minipig	5	Significant	0
Minipig	6	Significant	0
Minipig	7	Significant	0
Minipig	8	Significant	0
Minipig	9	Moderate	1
Minipig	10	Significant	0
Sheep	1	Moderate	1
Sheep	2	Little or none	2
Sheep	3	Moderate	1
Sheep	4	Moderate	1
Sheep	5	Little or none	2

*Table 13. Semi-quantitative Evaluation of bone resorption in the minipig and sheep models applying the Chen score. Note that the scoring system described by Chen et al. provides a subjective and general estimation of the severity of bone resorption of the entire defect, but it can not differentiate bone resorption from bone cyst and provide evaluation for each microfracture hole.*

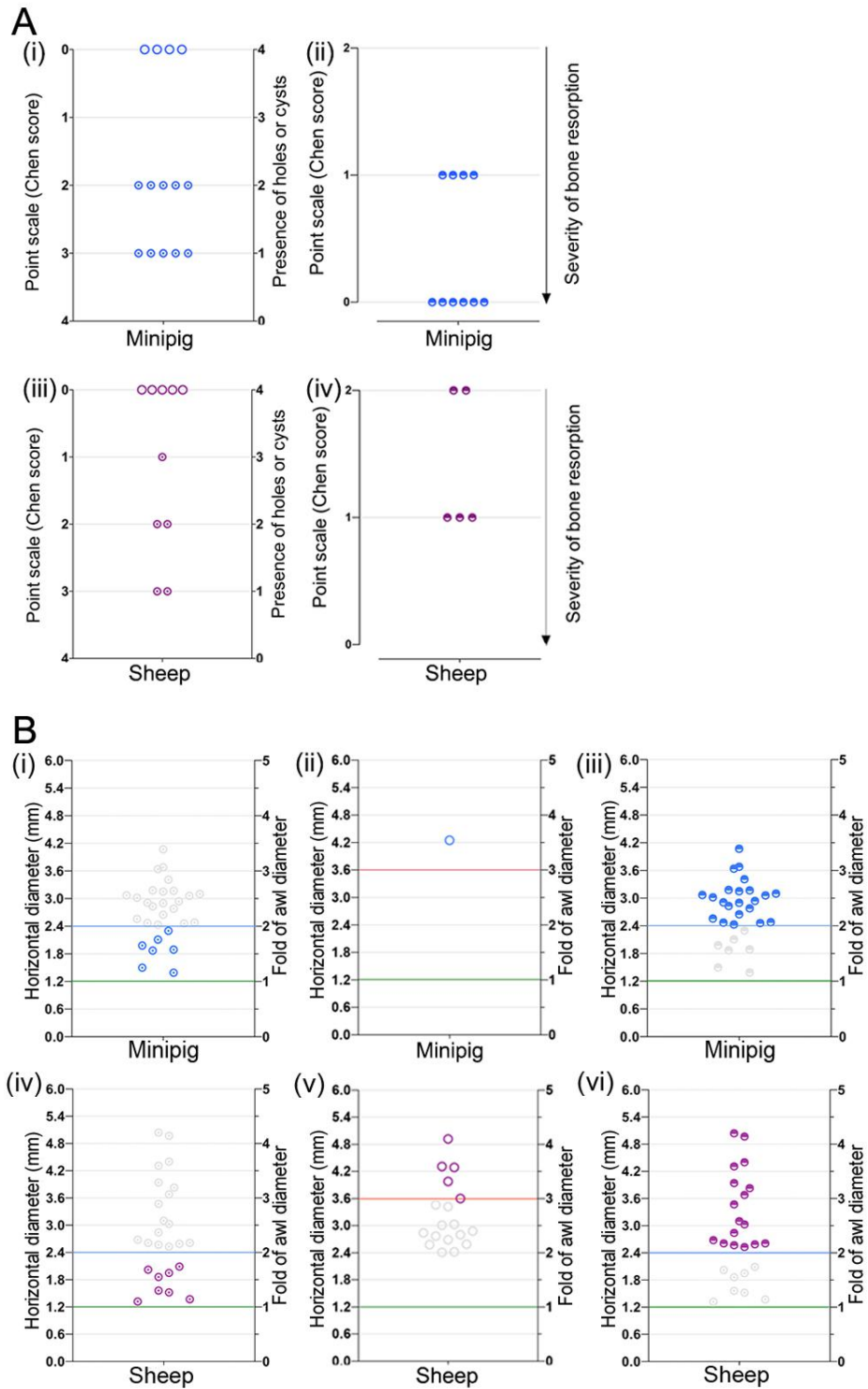


Figure 16. Comparison of the results of the Chen score and the present algorithm for analysing the subchondral bone changes in the two animal models. (A) Results of the Chen score: (i) residual microfracture holes and subchondral bone cysts in minipigs, (ii) bone resorption in minipigs, (iii) residual microfracture holes and subchondral bone cysts in sheep, and (iv) bone resorption in sheep. (B) Results

of the present algorithm: (i) residual holes in minipigs, (ii) subchondral bone cyst in minipigs, (iii) peri-hole bone resorption in minipigs, (iv) residual holes in sheep, (v) subchondral bone cysts in sheep, and (vi) peri-hole bone resorption in sheep. Compared with the Chen categorical score, the present algorithm enables an objective quantitation and discrimination of residual microfracture holes, peri-hole bone resorption, and subchondral bone cysts in both minipig and sheep models. The grey symbols in (B) indicate the eliminated subchondral bone changes according to the proposed cut-off values of the present algorithm. Figure reproduced from (GAO et al., 2016).

## 7.2 Bone marrow aspirate enhanced microfracture counteracting the early postoperative loss of subchondral bone

### 7.2.2 Articular cartilage repair

#### **Macroscopic findings**

During the defect preparation, immediate bleeding from the underlying subchondral bone plate was always observed after the removal of the calcified cartilage layer following debridement, microfracture, or bone marrow aspirate enhanced microfracture procedure. When the animals were euthanized at 4 weeks postoperatively, no joint effusion, macroscopic inflammation, peri-articular osteophytes, and adhesions were noticed in all treated joints following the three cartilage repair strategies (Figure 17A-C).

Parameter	Debridement	MFX	Enhanced MFX	Overall <i>P</i>	Specific <i>P</i>		
					*	#	§
Repair tissue color	2.60 ± 1.22	2.83 ± 0.75	2.33 ± 1.21	0.785	0.93	0.66	0.49
Blood vessels in the repair tissue	1.80 ± 2.05	3.00 ± 0.63	3.00 ± 1.10	0.271	0.54	0.33	1.00
Repair tissue surface	2.20 ± 1.79	2.00 ± 1.26	2.00 ± 1.26	0.966	0.79	0.93	0.94
Defect filling	2.00 ± 1.87	2.33 ± 0.82	1.50 ± 1.05	0.539	0.93	0.66	0.24
Adjacent cartilage degeneration	0.00 ± 0.00	0.50 ± 0.84	0.67 ± 0.82	0.300	0.43	0.18	0.70
Total	8.60 ± 6.31	10.67 ± 1.86	9.50 ± 4.46	0.745	1.00	1.00	0.39

Table 14. Macroscopic evaluation of the articular cartilage repair tissue. Values are expressed as mean ± SD. Graded on a scale of 0 to 20 (20 = worst repair; 0 = complete regeneration) according to Goebel et al. (GOEBEL et al., 2012). No statistic significant difference exists for all parameters and the average total score among the three treatment groups. Overall *P* values were for comparisons among the three treatment groups. Specific *P* values were for comparisons of two of the three treatment groups as follows: \**P* < 0.05 for debridement versus microfracture; #*P* < 0.05 for debridement versus enhanced microfracture; §*P* < 0.05 for microfracture versus enhanced microfracture group.

Semi-quantitative macroscopic analysis of articular cartilage repair in each defect according to the score developed by Goebel et al. (GOEBEL et al., 2012) showed no significant differences between defects from the three groups for all individual

parameters and the average total score (debridement:  $8.60 \pm 6.31$ ; microfracture:  $10.67 \pm 1.86$ ; enhanced microfracture:  $9.50 \pm 4.46$ ;  $P = 0.745$ ) (Figure 17V; Table 14).

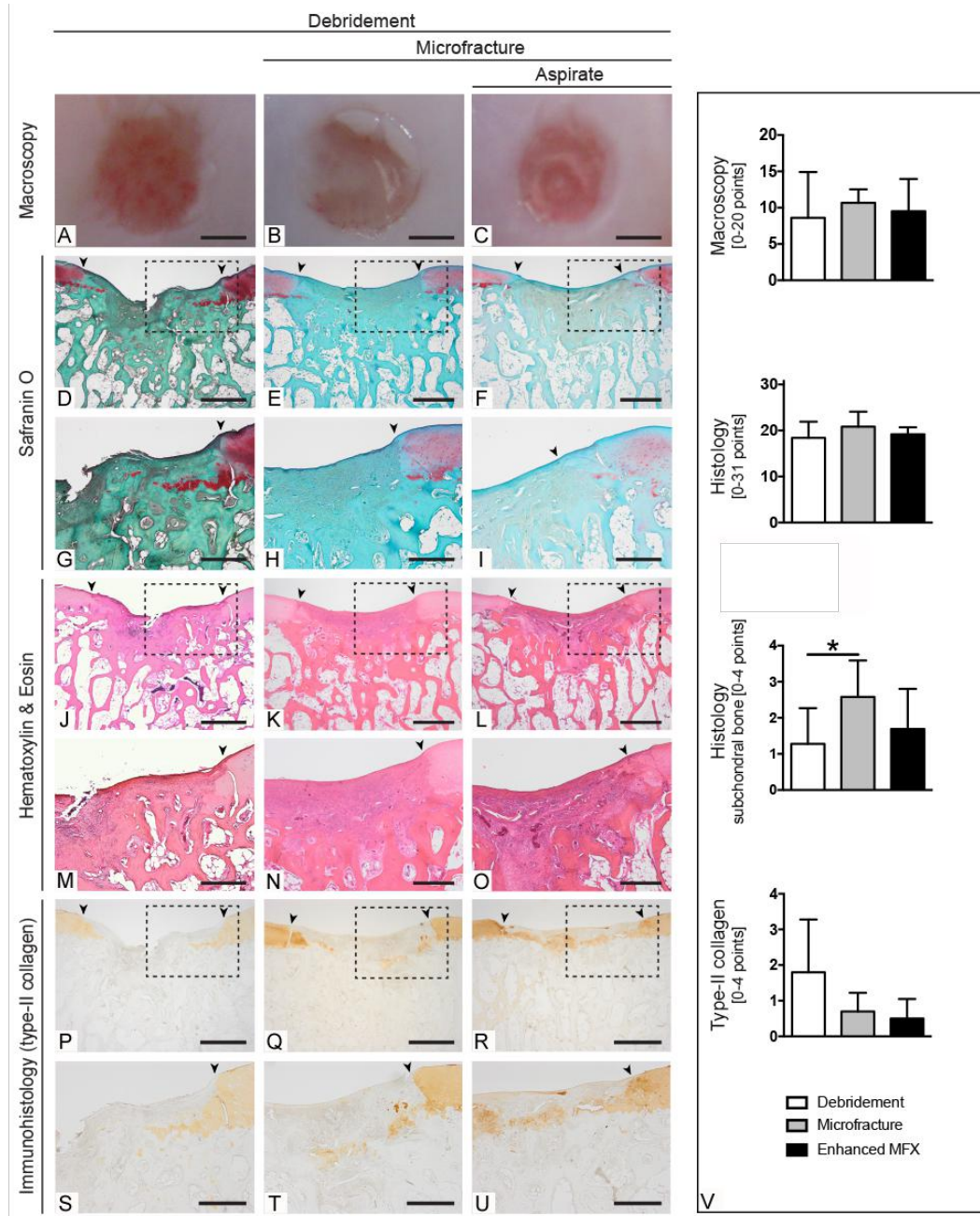


Figure 17. Macroscopic, histological and immunohistochemical analyses of the osteochondral unit. Standardized circular full-thickness chondral defects in the trochlear groove of minipigs were treated by (1) debridement (debridement group), (2) debridement and microfracture (microfracture group), and (3) debridement, microfracture, and application of bone marrow aspirate (enhanced microfracture group). By macroscopic grading, no significant differences in articular cartilage repair were detected between debridement group (A), microfracture group (B), and enhanced microfracture group (D). According to Sellers et al. (SELLERS et al., 1997), histological analysis of the cartilaginous repair tissue stained with

safranin O (D-I) and hematoxylin and eosin (J-O) also yielded no significant differences between debridement (D, G, J, M), microfracture (E, H, K, N), and enhanced microfracture group (F, I, L, O), except for a significantly higher percentage of subchondral bone within defects treated by debridement alone (V). Immunoreactivity to type-II collagen<sup>64</sup> was similar between defects treated with debridement (p, s), microfracture (Q, T), and enhanced microfracture (R, U). G-I, M-O, and S-U show the corresponding higher magnification images of the area within the dotted lines in the upper images. Black triangles denote defect borders (D-U). Scale bars: 2.0 mm (A-C), 0.5 mm (D-F, J-L, P-R), and 1.0 mm (G-I, M-O, S-U). Figure reproduced from (GAO et al., 2017b).

### **Histological evaluation**

Histological evaluation according to Sellers *et al.* (SELLERS et al., 1997) revealed that microfracture without or with bone marrow aspirate significantly improved the overall aspect of articular cartilage repair compared with debridement alone ( $0.075 < P < 0.896$ ) (Figure 17D-O,V; Table 15). Regarding the single parameter of subchondral bone reconstitution, a significantly impaired score value was observed following microfracture ( $2.58 \pm 1.01$ ) compared with debridement ( $1.28 \pm 0.99$ ;  $P = 0.050$ ) (Figure 17V). This adverse effect of microfracture on the histological aspect of subchondral bone reconstitution was counteracted by additional bone marrow aspirate ( $1.69 \pm 1.11$ ;  $P = 0.714$  for enhanced microfracture *versus* debridement) (Table 15).

Parameter	Debridement	MFX	Enhanced MFX	Overall <i>P</i>	Specific <i>P</i>		
					*	#	§
Defect filling	1.48 ± 1.22	1.90 ± 1.29	1.06 ± 0.73	0.415	1.00	0.66	0.09
Integration	1.25 ± 0.44	1.40 ± 0.61	1.50 ± 0.51	0.446	0.54	0.25	0.70
Matrix staining	2.95 ± 1.11	3.54 ± 0.50	3.44 ± 0.65	0.344	0.66	0.66	0.70
Cellular morphology	4.35 ± 1.00	4.54 ± 0.87	4.02 ± 1.08	0.595	0.43	0.79	0.31
Defect architecture	2.20 ± 0.99	2.35 ± 0.67	2.25 ± 0.60	0.896	0.54	0.66	0.70
Surface architecture	0.90 ± 0.90	0.54 ± 0.74	1.21 ± 1.17	0.261	0.66	0.54	0.07
Subchondral bone	1.28 ± 0.99	2.58 ± 1.01	1.69 ± 1.11	0.075	0.05	0.54	0.09
Tidemark	4.00 ± 0.00	2.98 ± 0.14	3.98 ± 0.14	0.670	0.66	0.66	1.00
Total	18.40 ± 3.51	20.83 ± 3.27	19.15 ± 1.52	0.314	0.25	0.66	0.09

*Table 15. Histological evaluation of the articular cartilage repair tissue. Values are expressed as mean ± SD. Bold values indicate a significant difference between groups ( $P < 0.05$ ). Graded on a scale of 0 to 31 (31 = no repair; 0 = complete regeneration) according to Sellers et al. (SELLERS et al., 1997). No difference of the average total score and each parameter existed in the histological scoring of the repair tissue between the three treatment groups. Overall *P* values were for comparisons among the three treatment groups. Specific *P* values were for comparisons of two of the three treatment groups as follows: \* $P < 0.05$  for debridement versus microfracture; # $P < 0.05$  for debridement versus enhanced microfracture; § $P < 0.05$  for microfracture versus enhanced microfracture.*

### **Immunohistochemical evaluation**

Immunoreactivity to type-II collagen was not significantly different between the three

groups (debridement:  $1.80 \pm 1.48$ ; microfracture:  $0.70 \pm 0.52$ ; enhanced microfracture:  $0.50 \pm 0.55$ ;  $P = 0.072$ ) (Figure 17P-U,V; Table 16).

	Debridement	MFX	Enhanced MFX	Overall $P$	Specific $P$		
					*	#	§
Points	$1.80 \pm 1.48$	$0.70 \pm 0.52$	$0.50 \pm 0.55$	0.072	0.177	0.126	0.699

*Table 16. Evaluation of immunoreactivity to type-II collagen in the articular cartilage repair tissue. Values are expressed as mean  $\pm$  SD. Immunoreactivity of type-II collagen was compared with the adjacent hyaline cartilage and graded on a scale from 0 to 4 (0 = no immunoreactivity; 4 = stronger immunoreactivity than adjacent cartilage)<sup>33</sup>. No statistically significant differences existed between the three treatment groups. "Overall  $P$  values" were for comparisons among the three treatment groups, while "specific  $P$  values" referred to comparisons between two treatment groups as follows: \* $P < 0.05$  for debridement versus microfracture; # $P < 0.05$  for debridement versus enhanced microfracture; § $P < 0.05$  for microfracture versus enhanced microfracture.*

### 7.2.3 Subchondral bone reconstitution

#### **Histomorphometric analysis of the subchondral bone**

Histomorphometric analysis within the defined region of interest (ROI) of the subchondral bone below the cartilage defects revealed no statistically significant differences of bone volume fraction (BV/TV), mean trabecular thickness (Tb.Th), mean trabecular separation (Tb.Sp), and mean trabecular number per length unit (Tb.N) between the three groups (all  $P > 0.05$ ) (Figure 18A,B; Table 17). Microfracture alone elicited a significantly higher density of osteoclasts than enhanced microfracture (microfracture:  $41.50 \pm 19.14$ ; enhanced microfracture:  $18.17 \pm 4.79$ ;  $P = 0.012$ ) (Figure 18C,D; Table 17). Osteoclasts were evenly distributed within the superficial, middle and deep zones of the entire ROI (all zones:  $P < 0.05$  for microfracture alone *versus* debridement and enhanced microfracture). Total osteoblast density was not different between the 3 groups ( $P > 0.05$ ). Interestingly, in the middle zone of the ROI, both microfracture without and with aspirate recruited significantly more osteoblasts when compared with debridement alone (3.1- and 2.6-fold, respectively; both  $P < 0.05$  for debridement *versus* microfracture without and with aspirate). Microfracture alone significantly reduced the amount of mature bone compared with debridement only ( $P = 0.013$ ; Figure 18E). Addition of bone marrow aspirate resulted in a significantly reduced new bone formation compared to microfracture alone ( $P = 0.008$ ; Figure 18E), while it did not significantly affect the amount of mature bone ( $P > 0.05$ ).

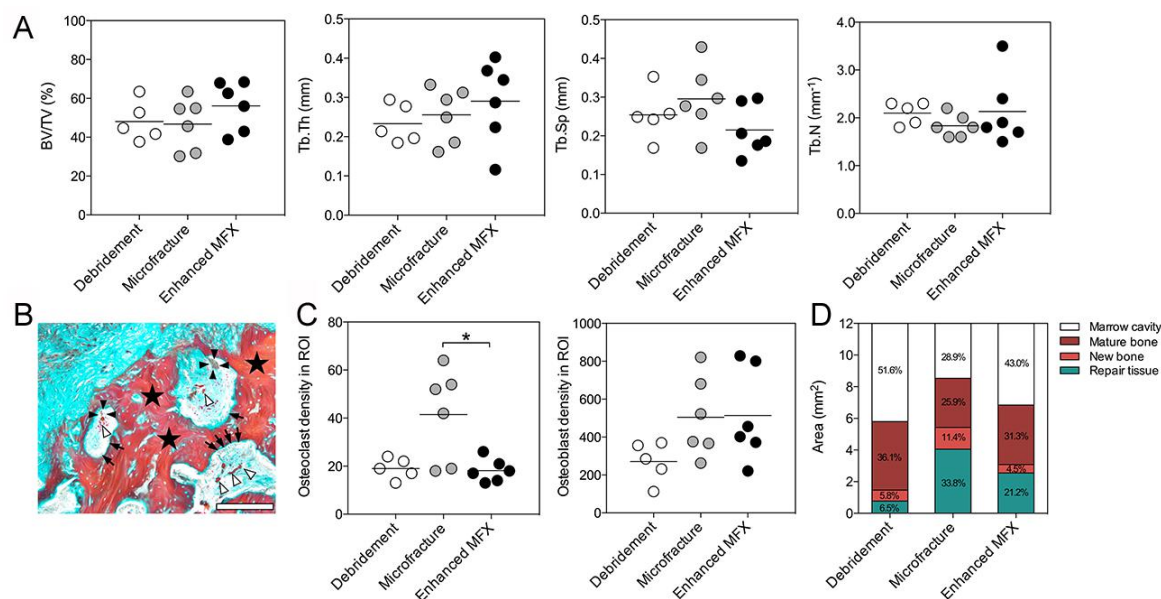
Parameter	Unit	Debridement	Microfracture	Enhanced microfracture	Overall <i>P</i>	Specific <i>P</i>		
						*	#	§
<i>Bone structure</i>								
BV/TV	%	48.06 ± 10.23	46.8 ± 13.45	56.13 ± 12.69	0.395	0.984	0.541	0.413
Tb.Th	mm	233.20 ± 49.51	255.88 ± 69.96	289.62 ± 107.64	0.523	0.890	0.502	0.756
Tb.Sp	mm	254.06 ± 65.52	295.53 ± 87.44	215.15 ± 65.03	0.206	0.633	0.668	0.180
Tb.N	mm <sup>-1</sup>	2.10 ± 0.23	1.83 ± 0.23	2.13 ± 0.73	0.514	0.635	0.993	0.536
<i>Osteoclast density</i>								
Superficial zone	-/-	8.33 ± 3.27	16.80 ± 6.53	7.33 ± 2.50	<b>0.005</b>	<b>0.014</b>	0.914	<b>0.007</b>
Middle zone	-/-	4.67 ± 3.14	15.00 ± 4.12	6.00 ± 1.90	<b>0.001</b>	<b>0.001</b>	0.743	<b>0.001</b>
Deep zone	-/-	5.83 ± 3.43	16.80 ± 6.53	4.83 ± 3.76	<b>0.015</b>	<b>0.034</b>	0.937	<b>0.018</b>
Total	-/-	19.00 ± 4.30	41.50 ± 19.14	18.17 ± 4.79	<b>0.008</b>	<b>0.020</b>	0.993	<b>0.012</b>
<i>Osteoblast density</i>								
Superficial zone	-/-	117.67 ± 65.89	152.80 ± 82.89	176.50 ± 101.90	0.501	0.777	0.473	0.891
Middle zone	-/-	65.67 ± 45.20	204.00 ± 72.49	172.33 ± 69.80	<b>0.006</b>	<b>0.007</b>	<b>0.028</b>	0.691
Deep zone	-/-	86.50 ± 64.24	152.80 ± 82.89	181.33 ± 118.11	0.119	0.147	0.201	0.958
Total	-/-	271.20 ± 104.53	505.00 ± 212.31	513.50 ± 246.38	0.123	0.173	0.154	0.997
<i>Area within ROI</i>								
Marrow cavity	mm <sup>2</sup>	6.21 ± 1.23	3.47 ± 0.68	5.16 ± 0.50	<b>0.004</b>	<b>0.004</b>	0.173	<b>0.034</b>
Mature bone	mm <sup>2</sup>	4.33 ± 0.84	3.11 ± 0.17	3.75 ± 0.12	<b>0.016</b>	<b>0.013</b>	0.197	0.145
New bone	mm <sup>2</sup>	0.69 ± 0.25	1.37 ± 0.47	0.54 ± 0.06	<b>0.007</b>	<b>0.021</b>	0.679	<b>0.008</b>
Repair tissue	mm <sup>2</sup>	0.78 ± 0.14	4.05 ± 0.04	2.55 ± 0.33	<b>0.001</b>	<b>0.001</b>	<b>0.001</b>	<b>0.001</b>

Table 17. Histomorphometric analysis of the subchondral bone below the treated cartilage defects.

### Qualitative evaluation of subchondral bone changes

According to a micro-CT based algorithm for the analysis of subchondral bone changes following microfracture treatment, no intra-lesional osteophytes and subchondral bone cysts were detected in defects from any treatment group. Residual microfracture holes and peri-hole bone resorption were frequently observed (Figure 18A; Table 18).

In defects treated with microfracture, only 2 of 18 holes (11%) were preserved as residual microfracture holes, while peri-hole bone resorption was observed in 16 of 18 holes (89%). In defects treated with enhanced microfracture, the incidence of residual microfracture holes and peri-hole bone resorption was 6/18 (33%) and 12/18 (67%), respectively. Yet, no significant differences in the maximal horizontal diameter, vertical diameter, area, and bone bridge height were detected between the microfracture and enhanced microfracture group.



**Figure 18.** Histomorphometric analyses of subchondral bone changes below the cartilage defects treated with the three experimental strategies. (A) No significant differences were seen between the three groups for BV/TV, Tb.Th, Tb.Sp, and Tb.N. (B) Typical higher-magnification image of the interface between the repair tissue and the subchondral bone, showing an accumulation of osteoclasts (black arrowheads) and osteoblasts (black arrows) as well as newly formed bone (black stars). The asterisks indicate the marrow cavity and the white arrowheads indicate blood vessels. (C) Density of osteoclasts and osteoblasts within the defined ROI. Compared with enhanced microfracture and debridement only, a significant higher density of osteoclast was detected in the microfracture group (without bone marrow aspirate). Microfracture without and with bone marrow aspirate recruited more osteoblasts than debridement alone to the treated subchondral bone. (D) Percentage of areas occupied by marrow cavity (white), original (mature) bone (dark red), new bone (light red), and repair tissue (green) within the defined ROI of defects from the three individual groups. Compared with microfracture alone, a significant larger area of marrow cavity and higher preservation rate of original (mature) bone were observed in the enhanced microfracture group. \* indicates a significant difference between debridement and microfracture group, # indicates a significant difference between debridement and enhanced microfracture, and § indicates difference between microfracture and enhanced microfracture. Scale bars: 200  $\mu\text{m}$  (B). Figure reproduced from (GAO et al., 2017b).

### Quantitative analysis of subchondral bone changes

The subchondral bone plate below the defects attained a significant decrease of bone volume fraction (BV/TV), specific bone surface (BS/BV), and bone surface density (BS/TV) when compared with the adjacent subchondral bone plate, irrespective of the treatment strategy (Table 18). Besides, both microfracture and enhanced microfracture treatments yielded a significant reduction in bone mineral density (BMD) of the subchondral bone plate beneath the defects when compared with the adjacent subchondral bone plate. No differences in cortical thickness of defect *versus* adjacent

subchondral bone plate were found between all groups.

	MFX (n = 18 holes)	Enhanced MFX (n = 18 holes)	P values
Residual microfracture holes			
Number (%)	2 (11%)	6 (33%)	0.228
Horizontal diameter (mm)	1.70 ± 0.02	1.50 ± 0.22	0.290
Vertical diameter (mm)	2.07 ± 0.13	2.43 ± 0.53	0.290
Area (mm <sup>2</sup> )	1.91 ± 0.60	2.02 ± 0.36	0.640
Bone bridge height (mm)	2.16 ± 0.51	1.97 ± 0.83	0.860
Peri-hole bone resorption			
Number (%)	16 (89%)	12 (67%)	0.228
Horizontal diameter (mm)	3.29 ± 0.22	3.43 ± 0.19	0.570
Vertical diameter (mm)	2.29 ± 0.67	2.16 ± 1.19	1.000
Area (mm <sup>2</sup> )	4.18 ± 1.96	2.73 ± 1.02	0.390

*Table 18. Comparative and descriptive results of the micro-CT analysis regarding residual microfracture holes and peri-hole bone resorption. Both the microfracture and enhanced microfracture group contained 6 cartilage defects per group (one per animal); each defect always received 3 microfracture penetrations (holes). Values are reported as mean ± standard error of the mean unless otherwise indicated. More residual microfracture holes and less peri-hole bone resorption were detected in the enhanced microfracture group. No significant difference existed for all parameters between the microfracture and enhanced microfracture group (all  $P > 0.05$ ).*

In the subarticular spongiosa below the articular cartilage defects, debridement resulted in a reduced bone volume fraction, trabecular thickness (Tb.Th) and structure model index (SMI) when compared with the adjacent subarticular spongiosa. Microfracture alone induced a general reduction of bone surface density (BS/TV), trabecular number (Tb.N), and degree of anisotropy (DA) as well as an increased trabecular separation (Tb.Sp) compared with the adjacent spongiosa. In defects treated by enhanced microfracture, a decrease of specific bone surface, trabecular pattern factor (Tb.Pf), structure model index, and degree of anisotropy was observed in the subarticular spongiosa of the defect region (Table 19).

At the level of the subchondral bone plate, debridement alone led to less severe osseous deterioration when compared with the microfracture and enhanced microfracture group as indicated by the highest volume of cortical thickness (debridement: 0.10 mm ± 0.02 mm; microfracture: 0.07 mm ± 0.02 mm; enhanced microfracture: 0.06 mm ± 0.01 mm;  $P = 0.006$ ) (Figure 19B; Table 19). Values for bone mineral density were also more preserved by debridement alone, but without reaching statistical significance (debridement: 630.79 mg CaHA/cm<sup>3</sup> ± 85.34 mg CaHA/cm<sup>3</sup>;

microfracture:  $410.05 \text{ mg CaHA/cm}^3 \pm 222.01 \text{ mg CaHA/cm}^3$ ; enhanced microfracture:  $460.05 \text{ mg CaHA/cm}^3 \pm 196.34 \text{ mg CaHA/cm}^3$ ;  $P = 0.066$ ).

Parameter (Unit)	Debridement		MFX		Enhanced MFX	
	Adjacent	Defect	Adjacent	Defect	Adjacent	Defect
Subchondral bone plate						
BMD (mg/cm <sup>3</sup> )	772.33 ± 70.32	630.79 ± 85.34	546.46 ± 251.06	410.01 ± 222.01*	599.87 ± 234.19	460.05 ± 196.34*
BV/TV (%)	78.71 ± 4.02	2.03 ± 1.19*	80.35 ± 7.44	1.25 ± 1.23*	75.97 ± 8.98	1.19 ± 0.95*
BS/BV (mm <sup>-1</sup> )	45.89 ± 9.11	120.74 ± 12.55*	50.39 ± 3.01	172.86 ± 76.16*	55.39 ± 10.45	162.76 ± 21.37*
BS/TV (mm <sup>-1</sup> )	35.88 ± 5.65	2.54 ± 1.81*	40.43 ± 3.81	1.65 ± 1.44*	41.53 ± 5.90	1.83 ± 1.33*
Ct.Th (mm)	0.08 ± 0.03	0.10 ± 0.02	0.06 ± 0.01	0.07 ± 0.02	0.07 ± 0.01	0.06 ± 0.01
Subarticular spongiosa						
BMD (mg/cm <sup>3</sup> )	863.89 ± 63.23	851.65 ± 32.64	585.94 ± 268.01	572.59 ± 244.75	667.43 ± 246.31	735.30 ± 244.95
BV/TV (%)	46.15 ± 6.27	40.08 ± 2.13*	41.80 ± 5.65	36.91 ± 3.90	41.66 ± 9.96	46.07 ± 6.38
BS/BV (mm <sup>-1</sup> )	28.03 ± 3.77	29.65 ± 2.59	30.55 ± 12.62	28.25 ± 3.00	30.49 ± 5.46	26.49 ± 3.47*
BS/TV (mm <sup>-1</sup> )	12.81 ± 1.44	11.88 ± 1.16	12.62 ± 1.61	10.44 ± 1.65*	12.35 ± 1.94	12.08 ± 1.24
Tb.Th (mm)	0.74 ± 1.38	0.12 ± 0.01*	0.11 ± 0.02	0.12 ± 0.02	0.37 ± 0.64	0.13 ± 0.02
Tb.Sp (mm)	0.46 ± 0.67	0.18 ± 0.02	0.17 ± 0.02	0.23 ± 0.05*	0.17 ± 0.03	0.17 ± 0.02
Tb.Pf (mm <sup>-1</sup> )	-2.19 ± 2.16	-0.01 ± 1.67	-2.10 ± 4.10	-2.17 ± 5.16	-1.80 ± 6.16	-5.40 ± 5.26*
Tb.N (mm <sup>-1</sup> )	3.19 ± 1.68	3.46 ± 0.38	3.81 ± 0.59	3.01 ± 0.50*	3.64 ± 0.57	3.61 ± 0.53
SMI (-/-)	0.47 ± 0.31	0.95 ± 0.32*	0.69 ± 0.58	0.90 ± 0.65	0.80 ± 0.70	0.49 ± 0.78*
DA (-/-)	1.84 ± 0.18	0.42 ± 0.03	1.90 ± 0.14	0.44 ± 0.03*	1.86 ± 0.17	0.39 ± 0.03*
FD (-/-)	2.42 ± 0.06	2.41 ± 0.07	2.41 ± 0.09	2.43 ± 0.04	2.38 ± 0.08	2.48 ± 0.02*

*Table 19. Comparison of micro-CT parameters of Volume Of Interests (VOIs) between the defect area and the adjacent control. Values are expressed as mean ± SD. Mann-Whitney U test was applied for comparison of parameters of subchondral bone between adjacent and defect regions. \*Significant difference between defect VOI and adjacent normal control structure. BMD, bone mineral density; BV/TV, bone volume fraction; BS/BV, specific bone surface; BS/TV, bone surface density; Ct.Th, cortical thickness; Tb.Th, trabecular thickness; Tb.Sp, trabecular separation; Tb.Pf, trabecular pattern factor; Tb.N, trabecular number; SMI, structure model index; DA, degree of anisotropy; FD, fractal dimension.*

At the level of the subarticular spongiosa (SAS-defect), the bone marrow aspirate enhanced microfracture group yielded an increased bone volume fraction (46.07% ± 6.38%) when compared with both microfracture alone (36.91% ± 3.90%;  $P = 0.008$ ; 0.8-fold) and debridement (40.08% ± 2.13%;  $P = 0.085$ ; 0.9-fold). Enhanced microfracture also led to a significantly lower trabecular separation (microfracture:  $0.23 \text{ mm} \pm 0.05 \text{ mm}$ ; enhanced microfracture:  $0.17 \text{ mm} \pm 0.02 \text{ mm}$ ;  $P = 0.015$ ), a higher trabecular number (microfracture:  $3.01 \pm 0.50$ ; enhanced microfracture:  $3.61 \pm 0.53$ ;  $P = 0.108$ ), and a reduced degree of anisotropy (microfracture:  $0.44 \pm 0.03$ ; enhanced microfracture:  $0.39 \pm 0.03$ ;  $P = 0.088$ ) when compared with microfracture alone (Figure 19C; Table 20). A comparison between debridement and microfracture group revealed no statistically significant differences within the subarticular spongiosa ( $0.093 < P < 0.988$ ) (Figure 19C; Table 20).

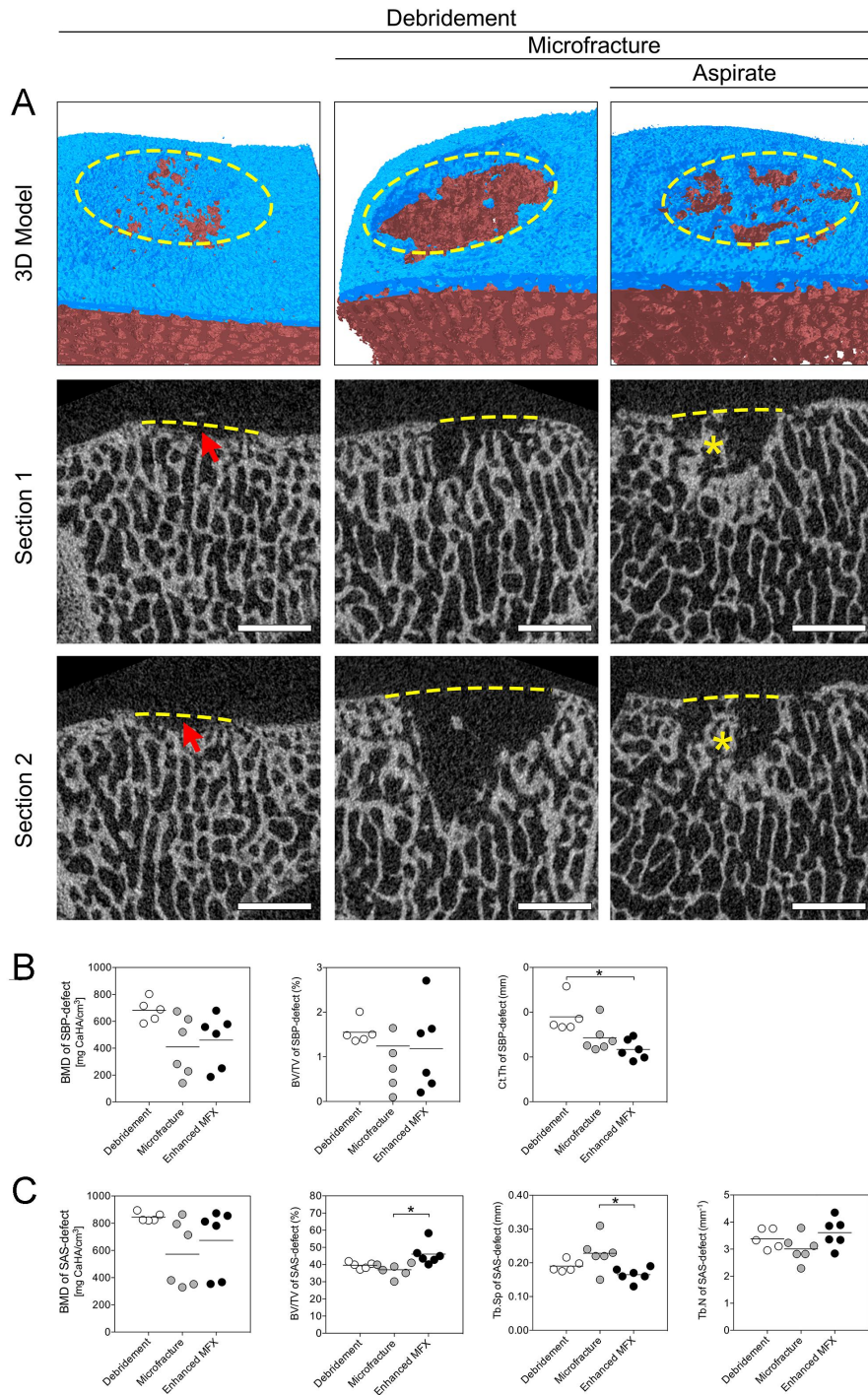


Figure 19. Qualitative and quantitative analysis of subchondral bone changes underlying defects treated with the three strategies. (A) Representative micro-CT images of subchondral bone changes. The top row shows a 3D reconstruction of characteristic defects. The subchondral bone plate and subarticular spongiosa are colored in blue and red, respectively. The yellow dashed ellipse shows the margin of the defect. The middle and bottom rows represent two different sections of the defects of the top row. Removal of the calcified cartilage layer in the debridement group induced subchondral bone loss (red arrows). In defects from the microfracture and enhanced microfracture group, residual microfracture holes

and peri-hole bone resorption were present. The yellow dashed lines indicate the projected cement lines, and the red asterisks indicate the preserved bone bridge between two residual microfracture holes. Scale bar: 2 mm. (B) Comparison of the micro-CT parameters of SBP-defect between the three treatment groups. \* $P < 0.05$ . (C) Comparison of the micro-CT parameters of SAS-defect between the three treatment groups. \* $P < 0.05$ . Figure reproduced from (GAO et al., 2017b).

Parameter (Unit)	Adjacent	Defect			Overall $P$
		Debridement	MFX	Enhanced MFX	
Subchondral bone plate					
BMD (mg/cm <sup>3</sup> )	631.74 ± 217.62	630.79 ± 85.34	410.01 ± 222.01 <sup>†</sup>	460.05 ± 196.34 <sup>†</sup>	0.07
BV/TV (%)	78.32 ± 7.09	1.55 ± 0.26 <sup>†</sup>	1.25 ± 1.23 <sup>†</sup>	1.19 ± 0.95 <sup>†</sup>	0.38
BS/BV mm <sup>-1</sup>	50.83 ± 8.56	120.74 ± 12.55 <sup>†</sup>	172.86 ± 76.16 <sup>†</sup>	162.76 ± 21.37 <sup>†</sup>	0.15
BS/TV (mm <sup>-1</sup> )	39.48 ± 5.42	2.54 ± 1.81 <sup>†</sup>	1.65 ± 1.44 <sup>†</sup>	1.83 ± 1.33 <sup>†</sup>	0.58
Ct.Th (mm)	69.77 ± 16.92	0.10 ± 0.02 <sup>#</sup>	0.07 ± 0.02	0.06 ± 0.01	<b>0.01</b>
Subarticular spongiosa					
BMD (mg/cm <sup>3</sup> )	696.45 ± 236.77	851.65 ± 32.64	572.59 ± 244.75	735.30 ± 244.95	0.13
BV/TV (%)	43.03 ± 7.42	40.08 ± 2.13 <sup>†</sup>	36.91 ± 3.90 <sup>§</sup>	46.07 ± 6.38	<b>0.01</b>
BS/BV (mm <sup>-1</sup> )	29.79 ± 4.58	29.65 ± 2.59	28.25 ± 3.00	26.49 ± 3.47 <sup>†</sup>	0.23
BS/TV (mm <sup>-1</sup> )	12.58 ± 1.59	11.88 ± 1.16	10.44 ± 1.65 <sup>†</sup>	12.08 ± 1.24	0.11
Tb.Th (mm)	0.39 ± 0.82	0.12 ± 0.01 <sup>†</sup>	0.12 ± 0.02	0.13 ± 0.02	0.38
Tb.Sp (mm)	0.26 ± 0.36	0.18 ± 0.02	0.23 ± 0.05 <sup>§</sup>	0.17 ± 0.02	<b>0.02</b>
Tb.Pf (mm <sup>-1</sup> )	-2.02 ± 4.28	-0.01 ± 1.67	-2.17 ± 5.16	-5.40 ± 5.26 <sup>†</sup>	0.23
Tb.N (mm <sup>-1</sup> )	3.57 ± 0.99	3.46 ± 0.38	3.01 ± 0.50 <sup>†</sup>	3.61 ± 0.53	0.11
SMI (-/-)	0.66 ± 0.55	0.95 ± 0.32 <sup>†</sup>	0.90 ± 0.65	0.49 ± 0.78 <sup>†</sup>	0.38
DA (-/-)	1.87 ± 0.16	0.42 ± 0.03	0.44 ± 0.03 <sup>†</sup>	0.39 ± 0.03 <sup>†</sup>	0.06
FD (-/-)	2.40 ± 0.08	2.46 ± 0.07	2.43 ± 0.04	2.48 ± 0.02 <sup>†</sup>	0.28

Table 20. Comparison of the micro-CT parameters of the subchondral bone plate and the subarticular spongiosa of defect region between three treatment groups. Values are expressed as mean ± SD. † = significant difference between defect VOI and adjacent normal control structure detected with Mann-Whitney U test. For overall  $P$  values, one-way ANOVA test was performed. Specific  $P$  values were reported as follows: † $P < 0.05$  for debridement versus microfracture; # $P < 0.05$  for debridement versus enhanced microfracture; § $P < 0.05$  for microfracture versus enhanced microfracture. Bold values indicate a significant difference between groups ( $P < 0.05$ ). BMD, bone mineral density; BV/TV, bone volume fraction; BS/BV, specific bone surface; BS/TV, bone surface density; Ct.Th, cortical thickness; Tb.Th, trabecular thickness; Tb.Sp, trabecular separation; Tb.Pf, trabecular pattern factor; Tb.N, trabecular number; SMI, structure model index; DA, degree of anisotropy; FD, fractal dimension.

### Mathematical modeling of subchondral bone volume changes

A mathematical comparison between the measured and calculated values of bone volume fraction of the treated subchondral bone plate showed a similar bone preservation rate in the three treatment groups (debridement: 1.97% ± 0.33%; microfracture: 2.12% ± 2.51%; enhanced microfracture: 2.14% ± 1.59%;  $P = 0.966$ ) (Figure 20A,C; Table 21). Within the subarticular spongiosa of the defect region, in contrast, compared with the other two groups, the enhanced microfracture yielded the significantly highest preservation rate of bone volume fraction (debridement: 85.69% ±

12.78%; microfracture: 122.54%  $\pm$  18.98; enhanced microfracture: 155.72%  $\pm$  24.51%;  $P = 0.0002$ ; 1.8-fold compared with debridement) (Figure 20B,C; Table 22).

Treatment	BV/TV (%) of SBP			Preservation rate (%)
	Adjacent control	Defect calculated	Defect measured	
Debridement	78.71 $\pm$ 4.02	78.71 $\pm$ 4.02	1.55 $\pm$ 0.26	1.97 $\pm$ 0.33
MFX	80.35 $\pm$ 7.44	58.66 $\pm$ 5.43	1.25 $\pm$ 1.23	2.12 $\pm$ 2.51
Enhanced MFX	75.97 $\pm$ 8.98	55.46 $\pm$ 6.56	1.19 $\pm$ 0.95	2.14 $\pm$ 1.59

*Table 21. Change of bone volume fraction (BV/TV) of the subchondral bone plate under defects treated by the three treatment strategies at 4 weeks postoperatively. Preservation rate was computed as the ratio of bone volume fraction (BV/TV) of SBP-defect<sub>(measured)</sub> to BV/TV of SBP-defect<sub>(calculated)</sub>. Overall P values were for comparison of the preservation rate of the calculated BV/TV among the three treatment groups, while specific P values were reported as follows: \* $P < 0.05$  for preservation rate of BV/TV of SBP-defect<sub>(calculated)</sub> between debridement and microfracture group; # $P < 0.05$  for preservation rate of BV/TV of SBP-defect<sub>(calculated)</sub> between debridement and enhanced microfracture group; § $P < 0.05$  for preservation rate of BV/TV of SBP-defect<sub>(calculated)</sub> between microfracture and enhanced microfracture group.*

Treatment	BV/TV (%) of SAS			Preservation rate (%)
	Adjacent control	Defect calculated	Defect measured	
Debridement	46.15 $\pm$ 6.27	46.15 $\pm$ 6.27	40.08 $\pm$ 2.13	86.85 $\pm$ 12.78**
MFX	41.80 $\pm$ 5.65	30.51 $\pm$ 4.12	36.91 $\pm$ 3.90	122.54 $\pm$ 18.98§
Enhanced MFX	41.66 $\pm$ 9.96	30.41 $\pm$ 7.27	46.07 $\pm$ 6.38	155.72 $\pm$ 24.51

*Table 22. Change of bone volume fraction (BV/TV) of the subarticular spongiosa under defects treated by the three treatment strategies at 4 weeks postoperatively. Preservation rate was computed as the ratio of bone volume fraction (BV/TV) of SAS-defect<sub>(measured)</sub> to BV/TV of SAS-defect<sub>(calculated)</sub>. Overall P values were for comparison of the preservation rate of SAS-defect<sub>(calculated)</sub> among the three treatment groups, while specific P values were reported as follows: \* $P < 0.05$  for preservation rate of BV/TV of SAS-defect<sub>(calculated)</sub> of defects from debridement versus microfracture group; # $P < 0.05$  for preservation rate of BV/TV of SAS-defect<sub>(calculated)</sub> of defects from debridement versus enhanced microfracture group; § $P < 0.05$  for preservation rate of BV/TV of SAS-defect<sub>(calculated)</sub> of defects from microfracture versus enhanced microfracture group.*

*Figure 20. Mathematical modeling of subchondral bone volume changes within the defect region following the three treatments. (A) Comparison of the calculated BV/TV of SBP-defect [ $SBP-defect_{(calculated)}$ ] and the measured BV/TV of SBP-defect [ $SBP-defect_{(measured)}$ ]. (B) Comparison of BV/TV of SAS-defect<sub>(calculated)</sub> and BV/TV of SAS-defect<sub>(measured)</sub>. (C) Comparison of preservation rate of BV/TV of SBP-defect<sub>(calculated)</sub> and SAS-defect<sub>(calculated)</sub> of the three groups. No apparent differences were found in preservation rates of BV/TV of SBP-defect<sub>(calculated)</sub> between the three groups, but additional application of aspirates yielded the highest preservation rate of BV/TV of SAS-defect<sub>(calculated)</sub>. \* $P < 0.05$ . Figure reproduced from (GAO et al., 2017b).*

## 8 DISCUSSION

In the present study, we investigated subchondral bone changes following marrow stimulation treatment. A focus was placed on the early effects of debridement and microfracture treatment without or with bone marrow aspirate on the osteochondral unit in the full-thickness chondral defect models. First, we tested the hypothesis that a novel algorithm for the precise analysis of subchondral bone changes with enhanced precision than the best existing evaluation method can be developed. The newly developed algorithm standardizes the analysis of subchondral bone alterations and enables a deeper understanding of the complex role of the subchondral bone following articular cartilage repair. This algorithm possesses a high inter-rater reliability and may serve as a basis for a more practical, objective, and reproducible evaluation of postoperative subchondral bone alterations in both animal models and patients. Second, we tested the hypothesis that early osteochondral repair following microfracture is enhanced if bone marrow aspirate is added as an adjunct to the microfracture procedure. The key finding here is that microfracture treatment of chondral defects induces a substantial early loss of the subchondral bone that may be significantly counteracted if autologous bone marrow aspirate is applied. Also, such bone marrow aspirate enhanced microfracture protected the subarticular spongiosa below the defects from osteoclast-mediated peri-hole bone resorption compared with microfracture alone. Importantly, debridement down to the subchondral bone similarly led to a reduction of the bone volume both in the subchondral bone plate and subarticular spongiosa. Interestingly, debridement and microfracture without or with bone marrow aspirate were equivalent regarding the early phase of articular cartilage repair.

### 8.1 Discussion of the novel algorithm for analysis of subchondral bone alterations

The key contributions of this part are to give an overview of the analytic methods currently described in the MEDLINE literature to examine subchondral bone changes, to provide clear definitions of the four types of subchondral bone changes and to develop a novel algorithm allowing for analysing and distinguishing these subchondral bone changes based on micro-CT images, to evaluate this new algorithm in datasets from two

large animal models, and to compare it with the best existing semi-quantitative scoring system.

### **8.1.1 Key advantages of the new algorithm**

We defined the term "intra-lesional osteophyte" as an osseous structure above the projected cement line. In a rabbit model following microfracture, Chen *et al.* defined an intra-lesional osteophyte as bone overgrowth above the projected tidemark in micro-CT images (CHEN *et al.*, 2011b). This definition does not reflect the fact that the calcified cartilage (and tidemark) is usually debrided to expose the subchondral bone plate in the standard microfracture procedure (STEADMAN *et al.*, 2001). Similarly, Shive *et al.* reported a limited incidence of intra-lesional osteophytes in patients after microfracture treatment by 3D quantitative MRI. The morphology of the intra-lesional osteophyte was calculated using the ratio of intra-lesional bone volume to the entire debrided lesion volume at one month postoperatively (SHIVE *et al.*, 2014). However, the change of this relative intra-lesional bone volume (termed "percentage of intra-lesional osteophyte") might be the result of other types of subchondral bone changes, such as peri-hole bone resorption or cyst formation (ORTH *et al.*, 2013), rather than a true intra-lesional osteophyte.

A key improvement of the suggested algorithm is that it allows for a specific, objective, and reproducible analysis of each single microfracture hole. In practice, it is very common to obtain a micro-CT image with a suspected bone bridge within the defect. The relative height of the suspected bone bridge is a novel parameter for defining the possible number of intra-lesional microfracture holes, allowing for an assessment of each microfracture hole separately. Clinically, the microfracture hole should be positioned perpendicular to the bone surface and independent to neighbouring holes. Therefore, the individual analysis of each microfracture hole provides more detailed information of the entire microfracture procedure.

Defining the horizontal diameter of the opening of the microfracture hole is useful to differentiate between residual microfracture holes and peri-hole bone resorption. To identify a residual hole, the double diameter of the microfracture awl is chosen as the

upper threshold value. This value takes into consideration a possible deflection of the awl during its impaction into the subchondral bone compartment, which, in theory, may cause an expansion of the hole. This recommended threshold for residual holes is consistent with the previous study of Hoemann *et al.*, showing that the maximal apical diameter of a microfracture hole (2.0 mm) was less than the double diameter of the original microfracture awl (1.1 mm) (HOEMANN et al., 2013). Additionally, based on the aforementioned descriptive analysis of peri-hole bone resorption in two different animal models, it is also suggested that the maximum diameter of the residual hole at its apical opening (Hd1) should be less than the double of the original awl diameter in order to fulfil the conditions of being a residual hole. If Hd1 is larger than the double of the awl diameter, a peri-hole bone resorption is defined.

### **8.1.2 Practicality, reliability, and enhanced precision of the algorithm**

The successful application of this algorithm using the recommended thresholds in two animal models proved its practicability to identify subchondral bone cysts. When shifting the thresholds for the identification of subchondral cysts only slightly, extremely lower (3%) and higher (53%) incidences were calculated, most likely not in line with the biological situation. For simplicity and practicability of this algorithm, a diameter (at the level of half of the penetration depth) 3-fold larger than the original awl diameter was chosen as threshold for subchondral bone cysts. Elevating or lowering of the recommended threshold value is not recommended, as this might result in either overestimation or underestimation of the incidence of these subchondral bone alterations.

The high reliability of the present algorithm has been verified with the calculation of inter-rater agreement (90% agreement) and Cohen's kappa (kappa = 0.874). In the independently blinded evaluations by two observers using the present algorithm, inter-rater disagreement only existed in 3 out of the total 30 randomly selected representative defects from two animal models. These data prove that the algorithm is highly reliable, reproducible, and valid for analysis the subchondral bone alterations in different animal models.

The enhanced precision of this tailored algorithm was demonstrated by the comparison with the most comprehensive score available (CHEN et al., 2011b). Compared with the semi-quantitative evaluation of the Chen score, the present algorithm uses the diameter of the microfracture awl as a stable reference and provides a more precise definition of each pattern of subchondral bone changes. Most importantly, it avoids the potential drawbacks of the Chen score for the incapacity to differentiate between residual microfracture holes, peri-hole bone resorption, and subchondral bone cysts. Additionally, this algorithm enables an objective and reproducible analysis of subchondral bone changes around each original microfracture hole.

### **8.1.3 Limitations of the novel algorithm**

The present algorithm has some limitations. First, owing to the specimen processing, the thresholds for subchondral bone cyst and peri-hole bone resorption were not tested by other modalities, such as inter-group comparison of standardized osteoclast histomorphometry. However, the present analysis in two large animal models proved the practicability and feasibility of the recommended thresholds. Secondly, the general upward migration of the subchondral bone plate - a possible independent type of subchondral bone alterations (ORTH et al., 2013) - was not detected in the datasets from the minipig and sheep models, therefore it was not included into the present algorithm. Finally, the different location of the defects in the two animal models (trochlear groove *versus* femoral condyle) may weaken the algorithm. As cartilage repair in sheep differs between trochlea and medial femoral condyle (ORTH et al., 2013), the suggested thresholds for bone cyst and peri-hole resorption may need to be adapted accordingly if the extent and pattern of subchondral bone alterations are similarly topographically dependent.

### **8.1.4 Potential clinical implications of the novel algorithm**

In the past decades, the subchondral bone has been increasingly recognized as being fundamentally important for the clinical success of articular cartilage repair (ELDRACHER et al., 2014, HOEMANN et al., 2013, IMHOF et al., 2000, MADRY et al., 2010, ORTH et al., 2013, ORTH et al., 2016, ORTH et al., 2012c). Microfracture, representing the clinically most relevant first-line treatment option for small chondral

lesions, has been extensively evaluated in patients with numerous outcome parameters and at various follow-up periods (GOYAL et al., 2013; MITHOEFER et al., 2009; MITHOEFER et al., 2005; ORTH et al., 2016; SARIS et al., 2009; ZAK et al., 2014). Our still insufficient understanding of subchondral bone repair after microfracture treatment is a strong motivation to further investigate the mechanisms of postoperative osteochondral remodelling in animal models. The current algorithm standardizes the analysis of subchondral bone alterations and enables a deeper understanding of the complex role of the subchondral bone after articular cartilage repair and further translating cell- or biomaterial-based techniques to preserve and restore the entire osteochondral unit. For applying the algorithm in clinical setting, it can conveniently be adapted to identify and analyze subchondral bone changes such as intra-lesional osteophytes, residual microfracture holes, peri-hole bone resorption, and subchondral bone cysts in conventional clinical CT or MRI protocols. This algorithm possesses a high inter-rater reliability and may serve as a basis for a more practical, objective, and reproducible evaluation of postoperative subchondral bone alterations in both animal models and patients in the future.

## **8.2 Discussion of bone marrow aspirate-enhanced microfracture**

### **8.2.1 Animal model selection**

In this study, we chose the Göttingen minipigs as the animal model for the osteochondral repair. The minipigs become skeletally mature between 16 and 24 months. Similar to human, the cartilage of adult minipigs also has limited capability for self-repair. The bone apposition rate, trabecular thickness, and collagen fiber arrangement in articular cartilage of the Göttingen minipigs are similar to those in humans (KÄÄB et al., 1998). Although the stifle joint of minipigs is notable smaller than the human knee, the joint size is enough for (osteo-) chondral defect creation with a diameter of 6-8 mm or even larger either in the femoral condyles or the trochlear groove, while the thickness of articular cartilage and the subchondral bone plate is relatively thinner (GOEBEL et al., 2017). Therefore, studies for both chondral and osteochondral defects can be performed with the Göttingen minipigs.

Gotterbarm and colleagues proved the limited capability for the endogenous repair of chondral and osteochondral defects and validated the utility of the Göttingen minipigs for articular cartilage repair research (GOTTERBARM et al., 2008). Christensen *et al.* evaluated multiple cartilage repair strategies in the minipig model and proved a clinical consistent repair process following different treatments in minipigs (CHRISTENSEN et al., 2015). In an osteochondral defect repair study, the cartilage regeneration potential of human umbilical cord blood-derived mesenchymal stem cells with a hyaluronic acid hydrogel composite has been proven at 12 weeks post-operatively (HA et al., 2015). These studies support the feasibility and practicability of the minipig model for the cartilage repair studies with partial-thickness, full-thickness, chondral defects and osteochondral defects.

### **8.2.2 Significant loss of subchondral bone following microfracture**

Microfracture treatment significantly reduced the amount of mature bone compared with debridement only, as determined by histomorphometrical analysis. The additional application of bone marrow aspirate to microfracture led, in the subarticular spongiosa, to a significantly higher bone volume fraction and increased trabecular number, together with a decreased trabecular separation compared with microfracture alone as determined by micro-CT analysis. In good agreement, the bone marrow aspirate treatment restrained the reaction of osteoclasts within the subchondral bone, thus acting towards preserving the original subchondral bone (microfracture: 25.9% *versus* enhanced microfracture: 31.3%). Together with the data from the histomorphometrical analyses, these findings suggest that microfracture treatment induces a substantial early loss of the subchondral bone that may be significantly counteracted by bone marrow aspirate, which however does not seem to primarily act via a stimulation of new bone formation in the region below the defects. It is possible, however, that such a stimulation of new bone formation may be seen at later time points. Moreover, the additional marrow aspirate yielded a change towards presence of more residual microfracture holes (microfracture: 11% *versus* enhanced microfracture: 33%) *versus* less peri-hole bone resorption (microfracture: 83% *versus* enhanced microfracture: 50%). Besides, the preservation rate of bone volume fraction of the subarticular spongiosa of defect region following microfracture was also significantly improved by addition of bone marrow

aspirate. These data suggest a protective effect of the bone marrow aspirate on the subchondral bone, especially the subarticular spongiosa, which is also consistent with previous studies on the osteogenic effect of bone marrow aspirate in fracture and osteonecrosis treatments (CONNOLLY et al., 1989; DAWSON et al., 2013; GIANAKOS et al., 2016). It is possible that the bone marrow aspirate protected the openings of the microfracture holes towards the joint space from the aggressive synovial fluid, thereby additionally favoring new tissue formation (ENEA et al., 2013; FORTIER et al., 2010; GIGANTE et al., 2011).

### **8.2.3 Subchondral bone loss after debridement**

The present study also demonstrated that debridement alone significantly affected the subchondral bone, which per definition was not perforated by the sole removal of the calcified cartilage layer. Of note, the great amount of bone loss occurred within the entire subchondral bone of the defect region in the debridement group, and the extent of bone loss of the subchondral bone plate of defect region was similar to that in the other two groups. However, the histological subchondral bone evaluation using the Sellers score showed an improved value in the debridement group compared with the microfracture treatment. Besides, the micro-CT calculation revealed that debridement retained the broadest subchondral bone plate among the three groups.

### **8.2.4 Equivalent outcome of cartilage repair between debridement and microfracture**

Regarding short-term outcomes of cartilage repair, debridement and microfracture functioned equivalently in the minipig model. This raises the question whether the additional penetration of the subchondral bone plate might be unnecessary for the generation of a fibrocartilage-like repair tissue. After a meticulous debridement, i.e. removal of the calcified cartilage layer, bleeding from the subchondral bone plate is often observed immediately within the defect in patients (JOHNSON, 1991). Such bleeding mostly originates from the opened vessels of the subchondral bone extending upward into the overlying calcified cartilage layer (MADRY, 2010b). The subsequently formed so-called “super clot” consists of bone marrow extracellular matrix, progenitor cells, and stem cells, which may be sufficient for the repair of the lesion (JOHNSON, 1986;

JOHNSON, SPECTOR, 2015). Possibly, this “super clot” is capable of fulfilling the same effects than the additional bone marrow aspirate in a clinical setting.

### **8.2.5 Comparable outcome of cartilage repair following microfracture without and with bone marrow aspirate**

Interestingly, addition of bone marrow aspirate to the microfracture treatment did not further improve cartilage repair compared with microfracture alone. One possible explanation for this finding is the relative paucity of the progenitor cells in the native, non-centrifuged bone marrow aspirate (HERNIGOU, BEAUJEAN, 2002; HERNIGOU et al., 2005). However, some authors questioned the difference of the cellular components between native and centrifuged marrow aspirate (CONNOLLY et al., 1989; HAUSER, ETESHOLA, 2013). The native bone marrow aspirate was even proven to be superior to centrifuged bone marrow aspirate for the healing of meniscal lesions in a dog model (ABDEL-HAMID et al., 2005). Another possible explanation is the short observation period in the present study. In previous studies with encouraging results of native or centrifuged bone marrow aspirate, evaluations were performed at 3 months (ABDEL-HAMID et al., 2005), 8 months (FORTIER et al., 2010), and even 10 years (HERNIGOU, BEAUJEAN, 2002).

### **8.2.6 Outlook of enhanced microfracture techniques**

Enhanced microfracture techniques aim to improve the standard microfracture by using matrices to stabilize the mesenchymal clot following microfracture treatment and to improve mesenchymal stem cell differentiation into chondrocytes. These procedures chiefly include autologous matrix-induced chondrogenesis (AMIC) (BENTHIEN, BEHRENS, 2010) and commercially available enhanced marrow-stimulation products (HIRAHARA, MUELLER, 2015; METHOT et al., 2016; VILA et al., 2015). However, reports of clinical outcomes for patients treated with enhanced microfracture technique for articular cartilage repair remain limited to date, and long-term outcomes are unavailable. Although most available literature of biomaterials enhanced microfracture do report promising clinical results in case series (GILLE et al., 2013; GILLE et al., 2010a; STANISH et al., 2013), further preclinical and randomized, double-blinded controlled clinical studies with larger cohorts and longer follow-up are required before

any conclusions can be drawn regarding the short- and long-term effectiveness of these techniques.

### **8.2.7 Clinical implications**

From a clinical standpoint, the present study and previous investigations in small animal models (CHEN et al., 2011a; CHEN et al., 2011b; CHEN et al., 2009a) show that the balance of bone turnover is clearly shifted towards bone resorption at this very early phase following microfracture. The finding of the present study that osteoclast density is higher in both microfracture groups compared with debridement alone is in good agreement with the work of Chen and colleagues, supporting the important role of osteoclasts as cellular mediators of marrow stimulation techniques that incise the subchondral bone (CHEN et al., 2011d). Remarkably, previous clinical studies reported pathological alterations of the subchondral bone at later time points. Especially subchondral bone cysts and intra-lesional osteophytes were seen in up to one third of patients treated with microfracture as early as 6 months postoperatively (KREUZ et al., 2006; MITHOEFER et al., 2005; SARIS et al., 2009). Together with the upward migration of the subchondral bone plate, these phenomena possibly play a role in the degeneration of the cartilaginous repair tissue over time (COLE et al., 2011; HENDERSON, LA VALETTE, 2005; MINAS et al., 2009; VASILADIS et al., 2010). As they weaken the subchondral bone support of the cartilaginous repair tissue, these data highlight the importance of the clinical treatment regimen of a protected weight bearing for the first 6 weeks postoperatively, as recommended for all marrow stimulation techniques in the tibiofemoral compartment of the human knee joint. Moreover, these data also serve to instigate more clinical observations of the early postoperative phase, e.g. by using MRI or cone beam CT (KOKKONEN et al., 2014) to search for similar changes of the subchondral bone in patients.

### **8.2.8 Limitations of the study on bone marrow aspirate-enhanced microfracture**

This study holds some limitations. Animals were allowed immediate full weight-bearing and received no postoperative rehabilitation regimes, which might alter the outcome of the postoperative repair of the osteochondral unit compared with the clinical situation. Also, only one single cartilage defect was created per knee in the debridement group,

while two defects per knee were generated in the microfracture or enhanced microfracture group. Yet, Christensen and colleagues observed no difference of cartilage repair between multiple or singular defects per knee (CHRISTENSEN et al., 2015). Finally, the 4-week time point selected here to study early osteochondral repair might be not long enough for an overall and final assessment. Strengths of this investigation include the use of a translational animal model and the choice of an early time point, allowing for an in-depth analysis of the early effects of marrow stimulation on the osteochondral unit with a broad variety of robust evaluation methods.

### **8.3 Conclusions**

A novel algorithm for the precise analysis of subchondral bone changes following marrow stimulation was developed, allowing for a more reliable, reproducible, and valid analysis of the subchondral bone compartment in a translational model of osteochondral repair. Also, we demonstrated that early loss of subchondral bone following microfracture can be counteracted by bone marrow aspirate, highlighting the potential benefits and clinical relevances of such bone marrow aspirate enhanced microfracture approaches.

## 9 REFERENCES

- Abdel-Hamid M, Hussein MR, Ahmad AF, Elgezawi EM (2005) Enhancement of the repair of meniscal wounds in the red-white zone (middle third) by the injection of bone marrow cells in canine animal model. *Int J Clin Exp Pathol* 86:117-123
- Armstrong SJ, Read RA, Price R (1995) Topographical variation within the articular cartilage and subchondral bone of the normal ovine knee joint: a histological approach. *Osteoarthritis Cartilage* 3:25-33
- Benthien JP, Behrens P (2010) Autologous matrix-induced chondrogenesis (AMIC). A one-step procedure for retropatellar articular resurfacing. *Acta Orthop Belg* 76:260-263
- Betsch M, Schneppendahl J, Thuns S, Herten M, Sager M, Jungbluth P, Hakimi M, Wild M (2013) Bone marrow aspiration concentrate and platelet rich plasma for osteochondral repair in a porcine osteochondral defect model. *PLoS One* 8:e71602
- Bhosale AM, Richardson JB (2008) Articular cartilage: structure, injuries and review of management. *Br Med Bull* 87:77-95
- Buckwalter J, Mankin H (1997) Articular cartilage: degeneration and osteoarthritis, repair, regeneration, and transplantation. *Instr Course Lect* 47:487-504
- Bullough PG, Yawitz PS, Tafra L, Boskey AL (1985) Topographical variations in the morphology and biochemistry of adult canine tibial plateau articular cartilage. *J Orthop Res* 3:1-16
- Chen G, Sun J, Lascau-Coman V, Chevrier A, Marchand C, Hoemann CD (2011a) Acute osteoclast activity following subchondral drilling is promoted by chitosan and associated with improved cartilage repair tissue integration. *Cartilage* 2:173-185
- Chen H, Sun J, Hoemann CD, Lascau-Coman V, Ouyang W, McKee MD, Shive MS, Buschmann MD (2009a) Drilling and microfracture lead to different bone structure and necrosis during bone-marrow stimulation for cartilage repair. *J Orthop Res* 27:1432-1438
- Chen H, Chevrier A, Hoemann CD, Sun J, Ouyang W, Buschmann MD (2011b) Characterization of subchondral bone repair for marrow-stimulated chondral defects and its relationship to articular cartilage resurfacing. *Am J Sports Med* 39:1731-1740
- Chen H, Hoemann CD, Sun J, Chevrier A, McKee MD, Shive MS, Hurtig M, Buschmann MD (2011d) Depth of subchondral perforation influences the outcome of bone marrow stimulation cartilage repair. *J Orthop Res* 29:1178-1184
- Chen H, Chevrier A, Hoemann CD, Sun J, Picard G, Buschmann MD (2013) Bone marrow stimulation of the medial femoral condyle produces inferior cartilage and bone repair compared to the trochlea in a rabbit surgical model. *J Orthop Res* 31:1757-1764

- Christensen BB, Foldager CB, Olesen ML, Vingtoft L, Rolwing JH, Ringgaard S, Lind M (2015) Experimental articular cartilage repair in the Gottingen minipig: the influence of multiple defects per knee. *J Exp Orthop* 2:13
- Cohen J (1960) A coefficient of agreement for nominal scales. *Educ Psychol Meas* 20:37-46
- Cole BJ, Farr J, Winalski CS, Hosea T, Richmond J, Mandelbaum B, De Deyne PG (2011) Outcomes after a single-stage procedure for cell-based cartilage repair: a prospective clinical safety trial with 2-year follow-up. *Am J Sports Med* 39:1170-1179
- Connolly J, Guse R, Lippiello L, Dehne R (1989) Development of an osteogenic bone-marrow preparation. *J Bone Joint Surg Am* 71A:684-691
- Curl WW, Krome J, Gordon ES, Rushing J, Smith BP, Poehling GG (1997) Cartilage injuries: a review of 31,516 knee arthroscopies. *Arthroscopy* 13:456-460
- Dawson JI, Smith JO, Aarvold A, Ridgway JN, Curran SJ, Dunlop DG, Oreffo ROC (2013) Enhancing the osteogenic efficacy of human bone marrow aspirate: concentrating osteoprogenitors using wave-assisted filtration. *Cytotherapy* 15:242-252
- Drobnic M, Radosavljevic D, Cor A, Brittberg M, Strazar K (2010) Debridement of cartilage lesions before autologous chondrocyte implantation by open or transarthroscopic techniques: a comparative study using post-mortem materials. *J Bone Joint Surg Br* 92:602-608
- Egan KP, Brennan TA, Pignolo RJ (2012) Bone histomorphometry using free and commonly available software. *Histopathology* 61:1168-1173
- Enea D, Cecconi S, Calcagno S, Busilacchi A, Manzotti S, Kaps C, Gigante A (2013) Single-stage cartilage repair in the knee with microfracture covered with a resorbable polymer-based matrix and autologous bone marrow concentrate. *Knee* 20:562-569
- Enea D, Cecconi S, Calcagno S, Busilacchi A, Manzotti S, Gigante A (2015) One-step cartilage repair in the knee: Collagen-covered microfracture and autologous bone marrow concentrate. A pilot study. *Knee* 22:30-35
- Erggelet C (2014) Enhanced marrow stimulation techniques for cartilage repair. *Oper Tech Orthop* 24:2-13
- Feldkamp LA, Goldstein SA, Parfitt AM, Jesion G, Kleerekoper M (1989) The direct examination of three-dimensional bone architecture in vitro by computed tomography. *J Bone Miner Res* 4:3-11
- Fortier LA, Potter HG, Rickey EJ, Schnabel LV, Foo LF, Chong LR, Stokol T, Cheetham J, Nixon AJ (2010) Concentrated bone marrow aspirate improves full-thickness cartilage repair compared with microfracture in the equine model. *J Bone Joint Surg Am* 92:1927-1937

- Frisbie D, Cross M, McIlwraith C (2006) A comparative study of articular cartilage thickness in the stifle of animal species used in human pre-clinical studies compared to articular cartilage thickness in the human knee. *Vet Comp Orthop Traumatol* 19:142-146
- Frisbie DD, Trotter GW, Powers BE, Rodkey WG, Steadman JR, Howard RD, Park RD, McIlwraith CW (1999) Arthroscopic subchondral bone plate microfracture technique augments healing of large chondral defects in the radial carpal bone and medial femoral condyle of horses. *Vet Surg* 28:242-255
- Gao L, Orth P, Goebel LK, Cucchiari M, Madry H (2016) A novel algorithm for a precise analysis of subchondral bone alterations. *Sci Rep* 6:32982
- Gao L, Orth P, Cucchiari M, Madry H (2017a) Effects of solid acellular type-I/III collagen biomaterials on in vitro and in vivo chondrogenesis of mesenchymal stem cells. *Expert Rev Med Devices* 14:717-732
- Gao L, Orth P, Muller-Brandt K, Goebel LK, Cucchiari M, Madry H (2017b) Early loss of subchondral bone following microfracture is counteracted by bone marrow aspirate in a translational model of osteochondral repair. *Sci Rep* 7:45189
- Gianakos A, Ni A, Zambrana L, Kennedy JG, Lane JM (2016) Bone marrow aspirate concentrate in animal long bone healing: an analysis of basic science evidence. *J Orthop Trauma* 30:1-9
- Gigante A, Calcagno S, Cecconi S, Ramazzotti D, Manzotti S, Enea D (2011) Use of collagen scaffold and autologous bone marrow concentrate as a one-step cartilage repair in the knee: histological results of second-look biopsies at 1 year follow-up. *Int J Immunopathol Pharmacol* 24:69-72
- Gill TJ, McCulloch PC, Glasson SS, Blanchet T, Morris EA (2005) Chondral defect repair after the microfracture procedure: a nonhuman primate model. *Am J Sports Med* 33:680-685
- Gille J, Kunow J, Boisch L, Behrens P, Bos I, Hoffmann C, Koller W, Russlies M, Kurz B (2010a) Cell-laden and cell-free matrix-induced chondrogenesis versus microfracture for the treatment of articular cartilage defects: a histological and biomechanical study in sheep. *Cartilage* 1:29-42
- Gille J, Schuseil E, Wimmer J, Gellissen J, Schulz AP, Behrens P (2010b) Mid-term results of Autologous Matrix-Induced Chondrogenesis for treatment of focal cartilage defects in the knee. *Knee Surg Sports Traumatol Arthrosc* 18:1456-1464
- Gille J, Anders S, Volpi P, De Girolamo L, Reiss E, Zoch W, Behrens P (2013) Outcome of autologous matrix induced chondrogenesis (Amic) in cartilage knee surgery: data of the Amic registry. *Arthroscopy* 29:e49-e50
- Glaser C, Putz R (2002) Functional anatomy of articular cartilage under compressive loading Quantitative aspects of global, local and zonal reactions of the collagenous network with respect to the surface integrity. *Osteoarthritis Cartilage* 10:83-99

- Goebel L, Orth P, Muller A, Zurakowski D, Bucker A, Cucchiari M, Pape D, Madry H (2012) Experimental scoring systems for macroscopic articular cartilage repair correlate with the MOCART score assessed by a high-field MRI at 9.4 T--comparative evaluation of five macroscopic scoring systems in a large animal cartilage defect model. *Osteoarthritis Cartilage* 20:1046-1055
- Goebel L, Gao L, Madry H (2017). Animal models in cartilage repair. In *Cartilage: Volume 3: Repair Strategies and Regeneration*, Grässel S, A Aszódi, eds. (Springer International Publishing), pp. 189-206.
- Goldring SR, Goldring MB (2016) Changes in the osteochondral unit during osteoarthritis: structure, function and cartilage-bone crosstalk. *Nat Rev Rheumatol* 12:632-644
- Gomoll AH, Madry H, Knutsen G, Dijk N, Seil R, Brittberg M, Kon E (2010) The subchondral bone in articular cartilage repair: current problems in the surgical management. *Knee Surg Sports Traumatol Arthrosc* 18:434-447
- Gotterbarm T, Breusch S, Schneider U, Jung M (2008) The minipig model for experimental chondral and osteochondral defect repair in tissue engineering: retrospective analysis of 180 defects. *Lab Anim* 42:71-82
- Goyal D, Keyhani S, Lee EH, Hui JH (2013) Evidence-based status of microfracture technique: a systematic review of level I and II studies. *Arthroscopy* 29:1579-1588
- Ha C-W, Park Y-B, Chung J-Y, Park Y-G (2015) Cartilage repair using composites of human umbilical cord blood-derived mesenchymal stem cells and hyaluronic acid hydrogel in a minipig model. *Stem Cells Transl Med* 4:1044-1051
- Haffner-Luntzer M, Heilmann A, Heidler V, Liedert A, Schinke T, Amling M, Yorgan TA, Vom Scheidt A, Ignatius A (2016) Hypochlorhydria-induced calcium malabsorption does not affect fracture healing but increases post-traumatic bone loss in the intact skeleton. *J Orthop Res* 34:1914-1921
- Hardin JA, Cobelli N, Santambrogio L (2015) Consequences of metabolic and oxidative modifications of cartilage tissue. *Nat Rev Rheumatol* 11:521-529
- Hauser R, Eteshola E (2013) Rationale for using direct bone marrow aspirate as a proliferant for re-generative injection therapy (prolotherapy). *Open Stem Cell J* 4:7-14
- Henderson IJ, La Valette DP (2005) Subchondral bone overgrowth in the presence of full-thickness cartilage defects in the knee. *Knee* 12:435-440
- Hernigou P, Beaujean F (2002) Treatment of osteonecrosis with autologous bone marrow grafting. *Clin Orthop Relat Res* 405:14-23

- Hernigou P, Poignard A, Manicom O, Mathieu G, Rouard H (2005) The use of percutaneous autologous bone marrow transplantation in nonunion and avascular necrosis of bone. *J Bone Joint Surg Br* 87B:896-902
- Hirahara AM, Mueller KW, Jr. (2015) BioCartilage: a new biomaterial to treat chondral lesions. *Sports Med Arthrosc* 23:143-148
- Hoemann CD, Hurtig M, Rossomacha E, Sun J, Chevrier A, Shive MS, Buschmann MD (2005) Chitosan-glycerol phosphate/blood implants improve hyaline cartilage repair in ovine microfracture defects. *J Bone Joint Surg Am* 87:2671-2686
- Hoemann CD, Lafantaisie-Favreau CH, Lascau-Coman V, Chen G, Guzman-Morales J (2012) The cartilage-bone interface. *J Knee Surg* 25:85-97
- Hoemann CD, Gosselin Y, Chen H, Sun J, Hurtig MB, Carli A, Stanish WD (2013) Characterization of initial microfracture defects in human condyles. *J Knee Surg* 26:347-355
- Imhof H, Breitenseher M, Kainberger F, Rand T, Trattnig S (1999) Importance of subchondral bone to articular cartilage in health and disease. *Top Magn Reson Imaging* 10:180-192
- Imhof H, Sulzbacher I, Grampp S, Czerny C, Youssefzadeh S, Kainberger F (2000) Subchondral bone and cartilage disease: a rediscovered functional unit. *Invest Radiol* 35:581-588
- Inoue H (1981) Alterations in the collagen framework of osteoarthritic cartilage and subchondral bone. *Int Orthop* 5:47-52
- Johnson LL (1986) Arthroscopic abrasion arthroplasty historical and pathologic perspective: present status. *Arthroscopy* 2:54-69
- Johnson LL (1991) Characteristics of the immediate postarthroscopic blood clot formation in the knee joint. *Arthroscopy* 7:14-23
- Johnson LL, Spector M (2015) The new microfracture: all things considered. *Arthroscopy* 31:1028-1031
- Käab M, Ap Gwynn I, Nötzli H (1998) Collagen fibre arrangement in the tibial plateau articular cartilage of man and other mammalian species. *J Anat* 193:23-34
- Kreuz P, Steinwachs M, Erggelet C, Krause S, Konrad G, Uhl M, Südkamp N (2006a) Results after microfracture of full-thickness chondral defects in different compartments in the knee. *Osteoarthritis Cartilage* 14:1119-1125
- Madry H (2010) The subchondral bone: a new frontier in articular cartilage repair. *Knee Surg Sports Traumatol Arthrosc* 18:417-418
- Madry H, van Dijk CN, Mueller-Gerbl M (2010) The basic science of the subchondral bone. *Knee Surg Sports Traumatol Arthrosc* 18:419-433

- Madry H, Gao L, Eichler H, Orth P, Cucchiari M (2017) Bone marrow aspirate concentrate-enhanced marrow stimulation of chondral defects. *Stem Cells Int* 2017:1609685
- McCormick F, Harris JD, Abrams GD, Frank R, Gupta A, Hussey K, Wilson H, Bach B, Jr., Cole B (2014) Trends in the surgical treatment of articular cartilage lesions in the United States: an analysis of a large private-payer database over a period of 8 years. *Arthroscopy* 30:222-226
- McIlwraith CW, Frisbie DD, Rodkey WG, Kisiday JD, Werpy NM, Kawcak CE, Steadman JR (2011) Evaluation of intra-articular mesenchymal stem cells to augment healing of microfractured chondral defects. *Arthroscopy* 27:1552-1561
- Methot S, Changoor A, Tran-Khanh N, Hoemann CD, Stanish WD, Restrepo A, Shive MS, Buschmann MD (2016) Osteochondral biopsy analysis demonstrates that BST-CarGel treatment improves structural and cellular characteristics of cartilage repair tissue compared with microfracture. *Cartilage* 7:16-28
- Minas T, Gomoll AH, Rosenberger R, Royce RO, Bryant T (2009) Increased failure rate of autologous chondrocyte implantation after previous treatment with marrow stimulation techniques. *Am J Sports Med* 37:902-908
- Mithoefer K, Williams RJ, 3rd, Warren RF, Potter HG, Spock CR, Jones EC, Wickiewicz TL, Marx RG (2005) The microfracture technique for the treatment of articular cartilage lesions in the knee. A prospective cohort study. *J Bone Joint Surg Am* 87:1911-1920
- Mithoefer K, Williams RJ, 3rd, Warren RF, Potter HG, Spock CR, Jones EC, Wickiewicz TL, Marx RG (2006) Chondral resurfacing of articular cartilage defects in the knee with the microfracture technique. Surgical technique. *J Bone Joint Surg Am* 88 Suppl 1 Pt 2:294-304
- Mithoefer K, McAdams T, Williams RJ, Kreuz PC, Mandelbaum BR (2009) Clinical efficacy of the microfracture technique for articular cartilage repair in the knee: an evidence-based systematic analysis. *Am J Sports Med* 37:2053-2063
- Moher D, Liberati A, Tetzlaff J, Altman DG (2009) Preferred reporting items for systematic reviews and meta-analyses: the PRISMA statement. *PLoS Med* 6:e1000097
- Müller-Gerbl M, Dalstra M, Ding M, Linsenmeier U, Putz R, Hvid I (1998) Distribution of strength and mineralization in the subchondral bone plate of human tibial heads. *J Biomech* 31:123
- Orth P, Cucchiari M, Kaul G, Ong MF, Graber S, Kohn DM, Madry H (2012a) Temporal and spatial migration pattern of the subchondral bone plate in a rabbit osteochondral defect model. *Osteoarthritis Cartilage* 20:1161-1169
- Orth P, Cucchiari M, Kohn D, Madry H (2012b) Alterations of the subchondral bone in osteochondral repair - Translational data and clinical evidence. *Eur Cell Mater* 25:299-316

- Orth P, Goebel L, Wolfram U, Ong MF, Gräber S, Kohn D, Cucchiari M, Ignatius A, Pape D, Madry H (2012c) Effect of subchondral drilling on the microarchitecture of subchondral bone: Analysis in a large animal model at 6 months. *Am J Sports Med* 40:828-836
- Orth P, Cucchiari M, Kohn D, Madry H (2013) Alterations of the subchondral bone in osteochondral repair--translational data and clinical evidence. *Eur Cell Mater* 25:299-316; discussion 314-296
- Orth P, Madry H (2015) Advancement of the subchondral bone plate in translational models of osteochondral repair: implications for tissue engineering approaches. *Tissue Eng Part B Rev* 21:504-520
- Orth P, Peifer C, Goebel L, Cucchiari M, Madry H (2015) Comprehensive analysis of translational osteochondral repair: Focus on the histological assessment. *Prog Histochem Cytochem* 50:19-36
- Orth P, Duffner J, Zurakowski D, Cucchiari M, Madry H (2016) Small-diameter awls improve articular cartilage repair after microfracture treatment in a translational animal model. *Am J Sports Med* 44:209-219
- Parfitt AM, Drezner MK, Glorieux FH, Kanis JA, Malluche H, Meunier PJ, Ott SM, Recker RR (1987) Bone histomorphometry: standardization of nomenclature, symbols, and units. Report of the ASBMR Histomorphometry Nomenclature Committee. *J Bone Miner Res* 2:595-610
- Pridie K, Gordon G (1959). A method of resurfacing osteoarthritic knee joints. *J Bone Joint Surg Br* 41:618-619
- Saris DB, Vanlauwe J, Victor J, Almqvist KF, Verdonk R, Bellemans J, Luyten FP (2009) Treatment of symptomatic cartilage defects of the knee: characterized chondrocyte implantation results in better clinical outcome at 36 months in a randomized trial compared to microfracture. *Am J Sports Med* 37:10S-19S
- Schneider CA, Rasband WS, Eliceiri KW (2012) NIH Image to ImageJ: 25 years of image analysis. *Nat Methods* 9:671-675
- Sellers RS, Peluso D, Morris EA (1997) The effect of recombinant human bone morphogenetic protein-2 (rhBMP-2) on the healing of full-thickness defects of articular cartilage. *J Bone Joint Surg Am* 79:1452-1463
- Shive MS, Restrepo A, Totterman S, Tamez-Pena J, Schreyer E, Steinwachs M, Stanish WD (2014) Quantitative 3D MRI reveals limited intra-lesional bony overgrowth at 1 year after microfracture-based cartilage repair. *Osteoarthritis Cartilage* 22:800-804
- Smillie I (1957) Treatment of osteochondritis dissecans. *J Bone Joint Surg Br* 39:248-260

Stanish WD, McCormack R, Forriol F, Mohtadi N, Pelet S, Desnoyers J, Restrepo A, Shive MS (2013) Novel scaffold-based BST-CarGel treatment results in superior cartilage repair compared with microfracture in a randomized controlled trial. *J Bone Joint Surg Am* 95:1640-1650

Steadman JR, Rodkey WG, Rodrigo JJ (2001) Microfracture: surgical technique and rehabilitation to treat chondral defects. *Clin Orthop Relat Res* 391:S362-369

Steadman JR, Briggs KK, Rodrigo JJ, Kocher MS, Gill TJ, Rodkey WG (2003) Outcomes of microfracture for traumatic chondral defects of the knee: average 11-year follow-up. *Arthroscopy* 19:477-484

Steadman JR, Rodkey WG, Briggs KK (2010) Microfracture: its history and experience of the developing surgeon. *Cartilage* 1:78-86

van 't Hof RJ, Clarkin CE, Armour KJ (2003) Studies of local bone remodeling. The calvarial injection assay. *Methods Mol Med* 80:345-351

Vanlauwe J, Saris DB, Victor J, Almqvist KF, Bellemans J, Luyten FP, Tig/Act, Group EXTs (2011) Five-year outcome of characterized chondrocyte implantation versus microfracture for symptomatic cartilage defects of the knee: early treatment matters. *Am J Sports Med* 39:2566-2574

Vasiliadis HS, Danielson B, Ljungberg M, McKeon B, Lindahl A, Peterson L (2010) Autologous chondrocyte implantation in cartilage lesions of the knee: long-term evaluation with magnetic resonance imaging and delayed gadolinium-enhanced magnetic resonance imaging technique. *Am J Sports Med* 38:943-949

Vila YRJ, Dalmau A, Chaques FJ, Asuncion J (2015) Treatment of osteochondral lesions of the talus with bone marrow stimulation and chitosan-glycerol phosphate/blood implants (BST-CarGel). *Arthrosc Tech* 4:e663-667

Weel H, Mallee WH, van Dijk CN, Blankevoort L, Goedegebuure S, Goslings JC, Kennedy JG, Kerkhoffs GM (2015) The effect of concentrated bone marrow aspirate in operative treatment of fifth metatarsal stress fractures; a double-blind randomized controlled trial. *BMC Musculoskelet Disord* 16:211

Woo SL, Buckwalter JA (1988) Injury and repair of the musculoskeletal soft tissues. *J Orthop Res* 6:907-931

Xing LZ, Jiang YQ, Gui JC, Lu YM, Gao F, Xu Y, Xu Y (2013) Microfracture combined with osteochondral paste implantation was more effective than microfracture alone for full-thickness cartilage repair. *Knee Surg Sports Traumatol Arthrosc* 21:1770-1776

Zak L, Albrecht C, Wondrasch B, Widhalm H, Vekszler G, Trattnig S, Marlovits S, Aldrian S (2014) Results 2 years after matrix-associated autologous chondrocyte transplantation using the novocart 3D scaffold: an analysis of clinical and radiological data. *Am J Sports Med* 42:1618-1627

## 10 PUBLICATIONS AND PRESENTATIONS

### Publications

1. **Gao L**, Orth P, Goebel LK, Cucchiari M, Madry H (2016) A novel algorithm for a precise analysis of subchondral bone alterations. *Sci Rep* 6:32982
2. **Gao L**, Orth P, Cucchiari M, Madry H (2017) Effects of solid acellular type-I/III collagen biomaterials on in vitro and in vivo chondrogenesis of mesenchymal stem cells. *Expert Rev Med Devices* 14:717-732
3. **Gao L**, Orth P, Muller-Brandt K, Goebel LK, Cucchiari M, Madry H (2017) Early loss of subchondral bone following microfracture is counteracted by bone marrow aspirate in a translational model of osteochondral repair. *Sci Rep* 7:45189
4. **Gao L**, Orth P, Cucchiari M, Madry H (2017) Autologous matrix-induced chondrogenesis – a systematic review of the clinical evidence. *Am J Sports Med*. DOI: 10.1177/0363546517740575. In press.
5. Guo R\*, **Gao L\***, Xu B (2017) Current evidence of adult stem cells to enhance anterior cruciate ligament treatment: a systematic review of animal trials. *Arthroscopy* 26:30706-30705  
\*co-first author
6. Xu G, **Gao L\***, Tao K, Wan S, Lin Y, Xiong A, Kang B, Zeng H (2017) Three-dimensional printed upper limb prosthesis for a child with traumatic amputation of right wrist: a case report. *Medicine*. DOI: 10.1097/MD.00000000000009426. In press.  
\*corresponding author
7. Madry H, **Gao L**, Eichler H, Orth P, Cucchiari M (2017) Bone marrow aspirate concentrate-enhanced marrow stimulation of chondral defects. *Stem Cells Int* 2017:1609685
8. Oláh T, Reinhard J, **Gao L**, Goebel L, Madry H (2017) Reliable landmarks for precise topographical analyses of pathological structural changes of the ovine tibial plateau in 2-D and 3-D subspaces. *Sci Rep*. DOI:10.1038/s41598-017-18426-3.  
In press.

**Oral Presentations**

1. **Gao L**, Müller-Brandt K, Orth P, Goebel LK, Cucchiarini M, Madry H. Autologous bone marrow aspirate enhanced microfracture counteracts the early loss of subchondral bone in a translational model of osteochondral repair. Annual Congress of the Orthopaedic Research Society, 03/2017, San Diego, USA.
2. **Gao L**, Müller-Brandt K, Orth P, Goebel LK, Cucchiarini M, Madry H. Autologous bone marrow aspirate enhanced microfracture counteracts the early loss of subchondral bone in a translational model of osteochondral repair. Annual Congress of the Deutsche Gesellschaft für Orthopädie und Orthopädische Chirurgie, 10/2017, Berlin, Germany.
3. Tu J, Guo R, **Gao L**, Xu H, Xu B. Single-stage surgery for knee dislocation with multiligamentous injuries in elderly patients. Annual Congress of the Aisa-Pacific Knee, Arthroscopy and Sports Medicine Society, 06/2016, Hongkong, China.

**Poster Presentations**

1. **Gao L**, Orth P, Goebel LK, Cucchiarini M, Madry H. A novel algorithm for a precise analysis of subchondral bone alterations. Annual Congress of the French Society for Mineralized Tissue Biology, 06/2016, Nancy, France.
2. **Gao L**, Orth P, Goebel LK, Cucchiarini M, Madry H. A novel algorithm for a precise analysis of subchondral bone alterations. Annual Congress of the Deutsche Gesellschaft für Orthopädie und Orthopädische Chirurgie, 06/2016, Berlin, Germany.
3. **Gao L**, Orth P, Goebel LK, Cucchiarini M, Madry H. A novel algorithm for a precise analysis of subchondral bone alterations. Annual Congress of the Orthopaedic Research Society, 03/2017, San Diego, USA.
4. Xu B, Guo R, **Gao L**, Xu H, Tu J. Multipotent cells used in anterior cruciate ligament surgery: a systematic review of animal and clinical Trials. Biennial Congress of the International Society of Arthroscopy, Knee Surgery and Orthopaedic Sports Medicine, 06/2017, Shanghai, China.

**Book Chapter**

1. Goebel L, **Gao L**, Madry H (2017). Animal Models in Cartilage Repair. In Cartilage: Volume 3: Repair Strategies and Regeneration, Grässel S, A Aszódi, eds. (Springer International Publishing), pp. 189-206.

## 11 ACKNOWLEDGEMENTS

I would like to express my deep and sincere gratitude to my supervisor, Prof. Dr. med. Henning Madry, and also Prof. Dr. rer. nat. Magali Cucchiarini and PD. Dr. med. Patrick Orth for their continuous support and persistent guidance during the past years on these works. Without their meticulous patience, valuable guidance and selfless help throughout the whole project, this dissertation would not be possible.

Special thanks must be sent to Prof. Dr. med. Michael Menger, Prof. Dr. med. Matthias Laschke, Dr. med. vet. Christina Körbel and the outstanding team from Institute for Clinical and Experimental Surgery for providing the experimental surgical facilities and for their professional support during the animal surgeries. Also, my grateful appreciation should go to Mrs. Gertrud Schmitt for the lab facilities and kind help during the research. Many thanks to Dr. med. Lars Goebel for the unreserved support of my work, for the scientific guidance and invaluable suggestions for the development of the scientific manuscripts. I am grateful for your friendly care.

I thank Dr. rer. nat. Ana Rey-Rico, Dr. rer. nat. Jagadeesh K. Venkatesan, and Dr. rer. nat. Tamas Olah for their technical assistance and for encouraging guidance during my dissertation writing. My special and grateful thanks to Ms. Kathrin Müller-Brandt, who helped me during the tedious scoring tasks and accompanied me during the whole projects. Thank you very much. I am also thankful to Ms. Carolin Peifer, Mr. Yannik Morscheid, Mr. Niklas Stachel, and Mr. Jan Reinhard for introducing me to the methods of the histologic scoring and the micro-CT analysis, for their helpful discussions and practical advice. I would also like to credit my old friend and senior colleague, Dr. Ke Tao, who always helped me with everything and made me never feel homesick.

To all the current and former members of the Center of Experimental Orthopaedics, especially to Dr. rer. nat. Janina Frisch, Mrs. Christina Cravens, Mrs. Susanne Speicher-Mentges, Mr. Oliver Müller, and Ms. Julianne Glomm: Many thanks to all of you for the nice working atmosphere, your helpfulness, and support in many issues and for caring about my work.

Last, but not least, to Ms. Jiani Wang, my family and all my friends: I thank you so much for believing in me and my work, for your understanding and support without any doubt.